Synthesis of One-Dimensional Nanostructure Materials

A Thesis
Presented to
The Academic Faculty

by

Zhengzhi Zhou
B.E, M.A.Sc

In Partial Fulfillment
of the Requirements for the Degree
Doctor of Philosophy in the
School of Chemical & Biomolecular Engineering

Georgia Institute of Technology
August 2009

Synthesis of One-Dimensional Nanostructure Materials

Approved by:

Dr. Yulin Deng, Advisor
School of Chemical and
Biomolecular Engineering
Georgia Institute of Technology

Dr. Sankar Nair
School of Chemical and
Biomolecular Engineering
Georgia Institute of Technology

Dr. Jeffery Hsieh
School of Chemical and
Biomolecular Engineering
Georgia Institute of Technology

Dr. Donggang Yao
School of Polymer, Textile, and
Fiber Engineering
Georgia Institute of Technology

Dr. Preet Singh
School of Materials Science and Engineering
Georgia Institute of Technology

Date Approved: 22/06/2009

In Memory of

My Father-in-law

Changyin Lin

ACKNOWLEDGEMENTS

There are so many people I would like to thank for their help during my graduate studies. First of all, I wish to express my gratitude to my Ph. D. advisor, Dr. Yulin Deng, for his guidance during my entire course of study at Georgia Tech and for his friendliness and approachability. His persistence in pursuing scientific inquiry is well established as a model for researchers. I would also like to thank my dissertation committee members for their valuable time. Particularly, I would like to thank Dr. Sankar Nair for his valuable advice in my research and for offering me an opportunity to continue to do research in nanoscience and nanotechnology after graduation. I thank Dr. Preet Singh for allowing me to use the equipment in his lab from time to time. In addition, I will always remember my discussions with Dr. Hsieh and Dr. Yao about my career path in science.

I would also like to take this chance to thank the members of Dr. Z. L. Wang's group at Georgia Tech: Yolande Berta for electron microscope training, Dr. Yong Ding for high resolution transmission electron microscopy, Dr. Jung-il Hong and the future Dr. Melanie Kirkham for their valuable help with X-ray analysis.

I am indebted to the members in our group. Dr. Hanjie Gu gave much assistance in nanobelt synthesis. Dr. Yulin Zhao and Dr-to-be Delong Song are always valuable resources for assistance. Other group members Dr. Zeshan Hu, Dr. Zhaohui Tong, and Dr. Ying Wang, to name a few, have been amazingly friendly and helpful during my stay at Georgia Tech.

I am grateful for many people who assisted in my education at Georgia Tech in all possible ways. In particular, my gratitude goes to Dr Cyrus Aidun and Dr. Jeff Empie for their help with the admission process and my first few days in IPST; and Dr. Bo Liao from the University of Toronto for his help with my literature search.

I am indebted to my parents for their understanding and support of my decision to go abroad to continue my education. I would also like to thank my father-in-law, Changyin Lin, for his encouragement and financial support during my studies. Without his support, it would have been impossible for me to study here.

I am deeply indebted to my wife, Shanhong, for her unconditional love, understanding, and support. I will always remember how much she has sacrificed herself to help me achieve my goals here. Without her support and sacrifice, I would never have been able to attain as high a level in my research. I hope that I can now help her to pursue her own career. My lovely two children, Sijia and Elin, are the angles in my life. They have a special way of making me laugh even when I come home exhausted.

I would like to thank IPST for funding the four and half years of my education and for providing a supportive environment and excellent facilities.

Having said all of the, I can now say that a new chapter of my life will open when I turn the next page of my life.

TABLE OF CONTENTS

LIST OF TABLES

LIST OF FIGURES

SUMMARY

Nanomaterials have numerous potential applications in many areas such as electronics, optoelectronics, catalysis and composite materials. Particularly, one-dimensional nanomaterials such as nanobelts, nanorods, and nanotubes can be used as either functional materials or building blocks for hierarchical nanostructures. However, before these applications can be realized, we must be able to control the synthesis of nanostructures. Many techniques have been developed to synthesize one-dimensional nanomaterials. Two of the main methods that have been used to date are chemical vapor deposition(CVD) and solution phase synthesis. In these synthesis methods, because many factors such as supersaturation, mixing, temperature, and impurities can have an important effect on the growth and final morphology of the nanomaterials of the products, making nanomaterial growth a complicated process. Until now, most of the synthesis experiments in nanomaterial synthesis have been based on a trial-and-error approach. In the CVD method, high temperature and low gas concentration are used. Therefore, the vapor phase synthesis can be treated as the ideal gas system. Compared with CVD method, solution phase synthesis has the advantages of low cost, flexibility, and potential to scale up. However, the process of solution phase synthesis is far more complicated and less understood due to the complexity and non-ideality of the reaction system. However, a fundamental understanding of how different process parameters affect the growth process is necessary for the control of the growth of nanostructures.

This thesis investigated the supersaturation effect as well as other effects on the growth of two one-dimensional nanomaterials - Magnesium hydroxide sulfate hydrate(MHSH) nanobelt and ZnO nanorod. These materials were adopted as model systems for synthesis in a low-temperature solution. Another advantage of for using these materials is that their nanostructures can be produced at a relatively low temperature(around 100^{o}C). To examine the supersaturation effect on one-dimensional nanostructure growth, this study developed a quantitative kinetic model was developed to describe the one-dimensional nanostructure growth. The qualitative investigation and the quantitative model should provide more insight to the processes and some guide-lines for one-dimensional nanostructure growth in the future. This thesis also examines other factors such as agitation and temperature.

Our first attention was paid to synthesize one dimensional nanostructure. The synthesis was based on the hypothesis that supersaturation for 1D nanostructure growth should be maintained at a low level and that supersaturation could be controlled by sparingly soluble carbonate salts. MHSH ($5Mg(OH)_2 \bullet MgSO_4 \bullet 3H_2O$) nanobelts were synthesized using sparingly soluble carbonate salts and magnesium sulfate as reactants. SEM observations revealed that the nanostructure formed possessed a thin belt structure and rectangular cross section profile. The nanobelts were as long as one hundred micrometers. Also investigated were the thermal properties of the nanobelts which decomposed step by step to form MgO. Because of its fast deposition, it is considered a brand new class of nanofiller material in polymer

composites with a very high aspect ratio. The formation of nanobelts can be correlated with the slow hydrolysis of carbonate ions. Due to the low solubility of the carbonate salts, the supersaturation level can be controlled at a low level. A high concentration of reactants resulted in irregular particles only. In addition, the reaction temperature had a significant effect on the nanobelt formation rate and morphology. A temperature higher than the normal boiling point of the solution and lower than 140 ^{o}C resulted in short and stiff nanoneedles. However, if the temperature was below the boiling point, no nanobelt could be produced. The synthesis of nanobelts not only provides direct evidence for the supersaturation effect on nanobelt growth but also offers the evidence that supersaturation can be controlled using sparingly soluble carbonate salts.

Supersaturation control by sparingly soluble carbonate salts was further extended to synthesize ZnO nanorods in solution. It was shown that a large number of ZnO nanorods could be synthesized using this approach. The nanorods had a hexagonal cross section. The nanorods were about 200 to 300nm in diameter and as long as 10 micrometers. Various characterizations such as SEM, XRD, and GC revealed that the growth of the nanorods took place during three stages. In the first stage, calcium carbonate reacted with zinc ion to form zinc carbonate hydroxide nanosheets. In the second stage, seeds for nanorod formation were formed into an egg shape. In the third stage , nanorods grew from the seeds. However, the sparingly

soluble carbonate salts could not be consumed completely and mixed with the final products. Purification of the nanorods from the mixtures was difficult.

We have successfully demonstrated the synthesis of one-dimensional nanostructures such as nanobelts and nanorods using sparingly soluble salts as supersaturation control agents. During the synthesis of nanostructure, many factors were found to impact the growth process. Factors such as supersaturation, temperature, and mixing affected not only the final morphology but also the growth rate of the products. To capture the essence of the growth process and provide some guidelines for future work, we built a quantitative model by establishing a simple kinetic model to describe the growth of ZnO nanorods from solution. The $Zn(NO_3)_2$ and hexamethylenetetramine (HMT) system was used as a model system because 1) it has been reported that this reaction system can produce ZnO nanorod under low temperature (< 95^oC), and 2) the reaction time is on a scale of hour, so its kinetics are easy to study. A quantitative model was built to correlate the concentration of Zn^{2+} with the length of the nanorods. The results show that the concentration of zinc ions in solution could be fitted into a first order reaction mechanism. The length of the nanorods increases with increasing temperature. However at a high temperature of 85 ^oC, the length of the nanorods approaches a constant. The higher the temperature, the faster the length of the nanorods approaches to a constant. The reason is that the HMT decomposed rapidly at a high temperature, resulting in high supersaturation which is beneficial to nucleation but not to crystal growth.

We have found that nanostructure growth in solution is a complicated process. After all, many process parameters affect the growth process and supersaturation is only one of them. We further demonstrated in this thesis that some other process parameters can have a significant effect on the growth process. Taking the $Zn(NO_3)_2$ and HMT system as a model system, we showed that agitation had dramatic effects on the final morphology of the nanostructure. Nanospheres could be obtained through mixing the reaction solution when other experiment conditions remained the same. The building blocks of the nanospheres were similar to those forming the nanorods. Thus, the spherical morphology was believed to result from the breakdown of the free diffusion of building blocks to the growing nanocrystal surface.

In summary, this thesis presents the syntheses of nanobelts and nanorods in solution, the development of a quantitative model for nanorod growth, and an investigation of different experimental conditions for nanostructure growth. Understanding the fundamentals of the growth of nanostructures is key to controlling their size and morphology. Through this work, we illustrate how some parameters such as supersaturation control through sparingly soluble salts affect the synthesis of nanomaterials. This work also reveals the underlying mechanism for one-dimensional nanostructure growth. The concepts, experiments, and analyses involved in this work can provide useful information for future work in the synthesis of nanomaterials.

Chapter 1 : Introduction and Background of Nanomaterials

During the last two decades or so, the paper industry has been challenged by an increasing awareness of environment protection and the requirements for better printability. The increasingly stringent environment regulations require that less fiber be consumed for papermaking. At the same time, the development of printing technology demands that papermakers manufacture high quality paper products. Economic globalization has put an unprecedented pressure on the paper industry to produce for low-cost products.

The Institute of Paper Science and Technology (IPST), a leading research institute in pulp and paper science and technology, is committed to serving its member companies around the world. IPST offers one solution that addresses the above challenges: to develop new fillers for the paper industry. To meet this challenge, IPST has funded a number of studies, including this project, that have investigated development of new fillers. To address this topic, this thesis begins by synthesizing new fillers that could potentially be used for papermaking.

1.1 Inorganic Pigments in Papermaking

The paper industry is engaged in a common practice of introducing inorganic particles into the papermaking process. The historical reason for this practice is that it reduces the consumption of fiber, the cost of which is considerably higher than that of inorganic particles. Later on, however, it was found that the properties of paper can be improved in many aspects by introducing certain types of inorganic particles. Depending on their function, such inorganic particles can be categorized into two groups: filler and pigments. A filler is added to the papermaking process through the wet end of the paper machine, retained in the paper web through various retention mechanisms, and is distributed evenly throughout the paper web. A pigment is mainly applied on a paper surface to provide desired functional end-use properties such as opacity, brightness, gloss, smoothness, and printability.

As mineral fillers are usually cheaper than wood fiber, an increase in filler content will directly result in reduced fiber cost while maintaining the same basis weight. In the papermaking process, a higher filler content also brings the benefits of fast water drainage and drying, leading to less energy consumption in the drying section. Continuous increases in fiber prices and regional fiber shortages have caused a rising trend in filler use. Other than the economic factors of using fillers in papermaking, more salient reason for using filler is that the properties of paper must

meet certain requirements such as opacity which cannot be met, especially for low basis weight paper, without adding fillers to the paper web.

1.1.1 Commonly used fillers and pigments

Commonly-used fillers and pigments include kaolin clay, ground calcium carbonate (GCC), and precipitated calcium carbonate (PCC), the three of which account for about 95% of filler usage in the paper industry. Some other fillers such as TiO_2 are very expensive, but they provide excellent optical properties for paper and are used only in special grade paper. Table 1-1 lists some of the general properties of fillers/pigments. The distribution of each pigment is shown in Figure 1-1.

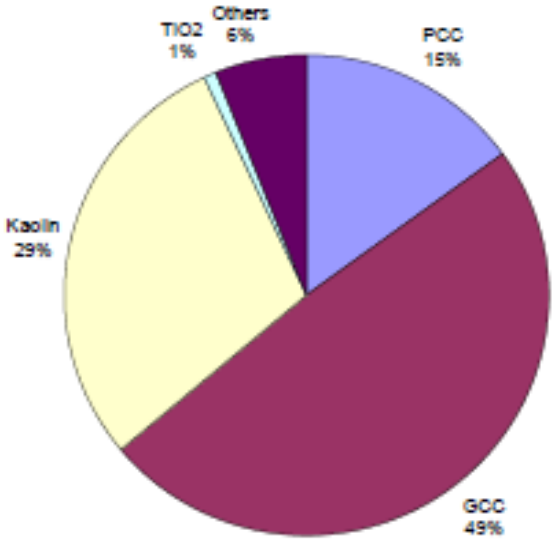

Figure 1-1 Global papermaking pigment demand [1].

Table 1-1 Summary of filler/pigment properties

	Average. Size, μm	Brightness, %
Clay	0.2-2.0	78-90
Calcined Clay	0.7-1.5	90-95
GCC	0.7-3.0	80-95
PCC	0.3-3.0	96-100
TiO_2	0.2-0.4	98-100

1.1.2 Effect of filler on the properties of paper

1.1.2.1 Effect of filler on the mechanical properties of paper

Generally, the strength of paper is determined by several factors: single fiber strength, the extent to which the fibers are bonded to each other (interfiber bonding), and the distribution of the fibers within the sheet (formation). Interfiber bonding is a result of the formation of hydrogen bonds during the drying process between individual fibers. Due to the weak nature of their interaction, the hydrogen bonds are easily disrupted and the overall paper strength depends on overlapping areas between the fibers and the intrinsic strength per unit area of contact. Introducing fillers to the paper sheet reduces its strength by interfering with interfiber bonding. Furthermore, the strength of paper decreases when the paper web contains less fiber per unit volume compared to unfilled paper. It was found that the size, the size distribution,

and the shape of the filler particles were factors of great importance for the properties of paper. In general, the smaller the pigment particles, the greater their negative effect on strength as shown in Figure 1-2, because smaller particles have relatively large surface areas [2] .

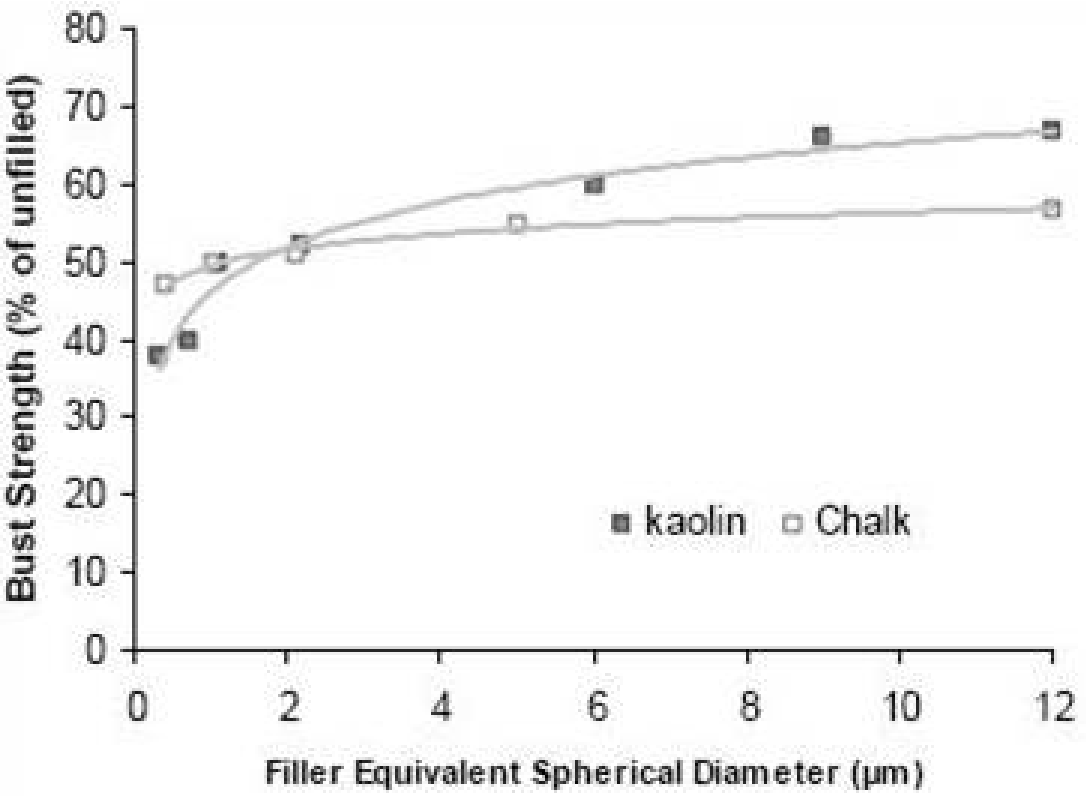

Figure 1-2: Effect of filler particle size on the burst strength of paper filled with different fillers [2].

For particles greater than 5µm, the effect of the shape and number of particles dominate in strength of paper due to large particles disrupting points of interfiber

bonding, so platy kaolin yields greater benefits. For particles less than 2μm, the surface area becomes more important because the attachment of small filler particles to fibrils prevents their collapse and consolidation upon drying, so blocky fillers show better results [2].

1.1.2.2 Effect of fillers on the optical properties of paper

As mentioned earlier, the improvement of optical properties, including opacity and brightness, is another main reason to add fillers to paper sheet because the inorganic fillers generally have higher light scattering of filler than wood fibers. Most fillers are white and their light scattering ability in the sheet can significantly improve the brightness of paper. When fillers are added to a paper sheet, they can create more voids within the sheet, and therefore more interfacial surfaces. Such voids can be considered important as individual particle elements of the same size. Different morphologies such as aggregates cause different behaviors in their ability to scatter light and different physical properties. Filled paper was reported to have a much higher pore volume than unfilled paper, which is evidence that fillers are playing the role of spacers within a sheet of paper so that they enhance optical properties.

1.1.3 Development of new fillers

While the target for filler usage in paper is to achieve as high filer content as possible to reduce fiber cost and maintain acceptable paper performance, the addition of fillers may inevitably adversely affect properties of paper, particularly its strength. As a solution to this problem, different fillers have been synthesized [3, 4]. Paper filled with clay coated with starch has much higher tensile strength than paper filled with conventional clay, but the optical properties are retained.

It is well known that the properties of nanomaterials differ from those of bulk materials, and papermakers hope to exploit such novel properties with advances of nanotechnology. Through carefully designed synthesis procedures, the newly synthesized particles are expected to offer excellent physical and optical performance. Ideally these particles should have a minimal impact on paper strength and provide other desired properties such as high bulk. In addition, they should be cost effective. Recently, Mathur has reported the successful synthesis of a promising high performance filler composed of crystalline calcium silicate hydrate as shown in Figure 1-3 [5]. The fillers are highly porous haystack-like particles containing complex multi-phase crystalline fibers. While the particles are fairly large (d = 0.1-0.2 μm, l = 1–4 μm) and irregular in shape, they scatter light better than PCC, GCC, clay, or calcined clay. The particles offer higher brightness and opacity than

schalenahedral PCC. Other claimed advantages of this filler include low bulk density, good chemical stability in aqueous solution, and high ink adsorptive capability.

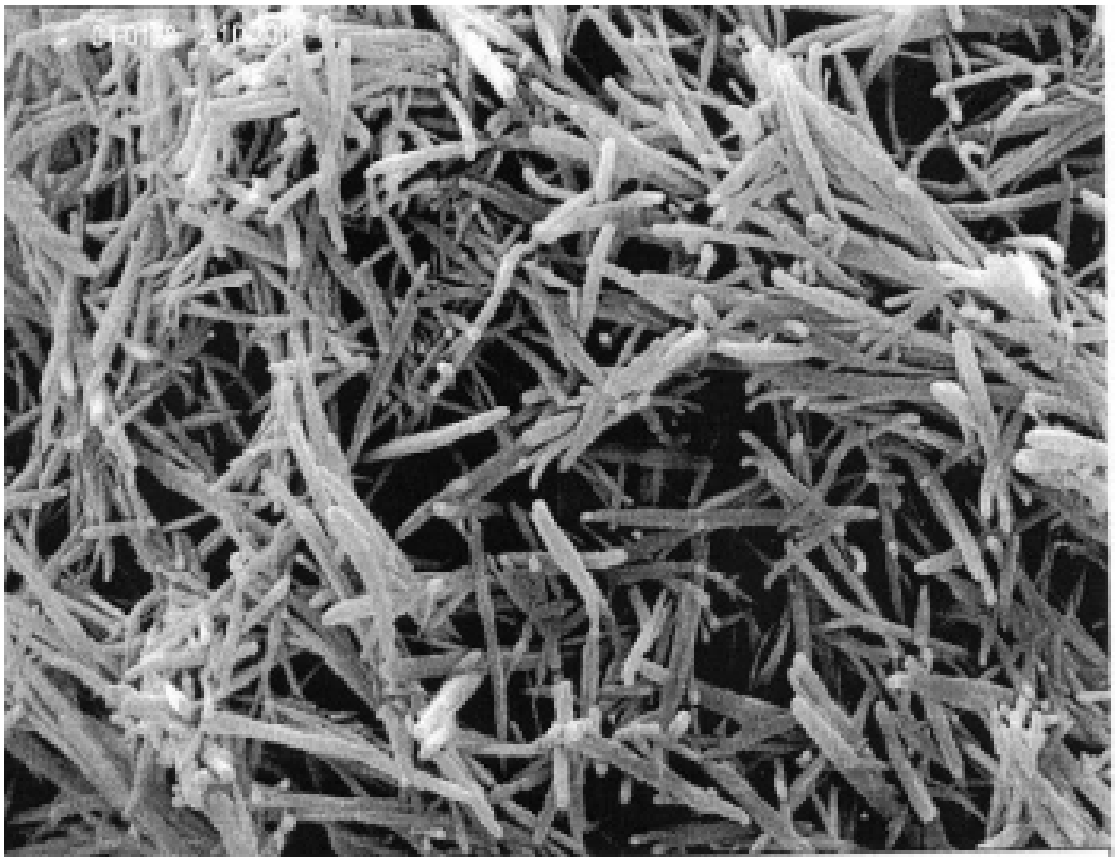

Figure 1-3 Fibrous silicate filler for papermaking [5]

Although nanostructured fillers offer better performance than conventional fillers, the synthesis and control of the nanostructures have not been fully understood. Furthermore, most nanostructured fillers are expensive. It was reported that magnesium hydroxide sulfate hydrate ($5Mg(OH)_2.MgSO_4.3H_2O$) can be synthesized in one dimensional morphology at a low cost. Thus, the first part of the research of

this thesis focuses on low cost, large scale synthesis of magnesium hydroxide sulfate hydrate nanostructures.

1.2 Introduction to Nanomaterials

"Nano", a word derived from the Greek word *nanos*, means "dwarf or small". Nanosize is a range of size located close to the size of an atom in the length spectrum. Nanostructure materials, which at least have one dimension in the range of 1-100 nm (1 nm = 10^{-9}m), have received tremendous attention in recent years. The interest stems first from the fact that new phenomena and novel properties have been observed when the materials have a length sale of less than 100 nm, even a few nanometers. Secondly, the development of electron microscopy and other characterization methods has made the direct observation and manipulation of materials at nanoscale possible.

Nanomaterials are novel due to two unique properties: size change and structure change. When the particle size is reduced to a nanoscale domain, the number of atoms on the particle surface increases significantly. From the classic colloid theory, we know that atoms on surfaces behave differently from those inside bulk material. Thus, we can expect that the properties of nanosize materials will differ from those of bulk materials. In addition to their nanosize, their structure is also unique. When the size of particles shrinks to a few nanometers, the energy bands may

stop overlapping with each other and show quantized energy bands, resulting in dramatic change in the properties.

Based on the ratios of structural dimensions, nanomaterials are typically categorized into three dimensional groups: 0-dimension, 1-dimension and 2-dimension. 0-dimensional nanostructures, also referred to as "quantum dots" or more generally as "nanoparticles" with an aspect ratio around unity duo to its three dimensions, have been widely used as biomarker [6-8]. Two-dimensional thin films also have been explored and utilized in many applications in optical coating [9, 10], corrosion protection [11, 12], and semiconductor devices [13-15]. Nanostructures of one-dimension (1D), including nanorods, nanowires, and nanobelts, have one aspect ratio most commonly much larger than 1.

1.3 Properties of Nanomaterials

Nanostructured materials have attracted extreme attention due to their novel properties, which significantly differ from the properties of bulk materials. These difference, which strongly relate to size, specific surface area, and morphology have been verified experimentally [16-18]. For example, gold nanoparticles can appear orange, purple, or blue as their size changes from 1 nm to up to hundreds of nanometers [19]. Semiconductor CdSe nanocrystals with different sizes show different colors under UV illumination[20]. Other properties such as the melting point

also have been reported to change with the size of the material. For example, the melting point of gold 4 nm nanoparticles decreases to 427 ^{o}C from its bulk value of 1063^{o}C[21] and that of a 2 nm CdSe nanoparticles drops from 1600^{o}C to about 400 ^{o}C [22].

Among the nanomaterials with different morphologies, one-dimensional (1D) nanostructures, with two physical dimensions in the range of 1~100 nm and a large third dimension, have been the focus of intense interest in both academic research and industrial applications because of their potential as building blocks for other nanostructures. Typically, four types of 1D nanostructure have been reported in the literature, including nanotubes [23-26], nanowires [27-30], nanorods [31-33], and nanobelts [34, 35]. Due to physical dimension limits, such nanostructures have exhibited novel optical [36, 37], electronic [38-40], and mechanical properties [41-46].

1.3.1 Review of electrical properties of nanomaterials

Due to the effects of their size, nanomaterials and bulk material exhibit dramatically different properties in electrical conductivity. For example, the well-studied carbon nanotubes have unique electrical behaviors. Researchers have reported discrete quantized electrical conductivity for single wall carbon nanotubes with a diameter of 1.38 nm at a length of as much as 140nm [47]. The conductivity of

carbon nanotubes was also reported to be geometry and temperature dependent [48]. However, no such geometry dependent phenomena were reported in bulk material.

Semiconductor ZnO nanomaterials also exhibit similar size-dependent electrical properties. At nanoscale, ZnO nanomaterial and bulk material exhibit dramatic difference in conductivity. In one experiment measuring the current-voltage characteristics as a function of ambient temperature and gas, in a temperature range from 25 to 150 ^{o}C, ZnO nanorods with diameters of 130 nm were reported sensitive to trace concentrations of gases in the ambient measurement, even at room temperature, demonstrating their potential as gas sensors [49].

ZnO nanowires were used to fabricate field-effect transistors (FETs) in vacuum and with a variety of ambient gases from 5 to 300 K. In air, these n-type nanowire transistors had among the highest mobility. Four probe measurements showed that the resistivity of the Ti/Au-ZnO contacts was 0.002-0.02 Omega/cm. The performance characteristics of the nanowire transistors were also found to be dependent on the presence and the nature of adsorbed surface species [50].

1.3.2 Optical properties

Similarly, within respect to optical properties, nanocrystals also demonstrate strongly size-dependent phenomena, so they are attractive candidates as tunable light

absorbers and emitters in optoelectronic devices such as light-emitting diodes and quantum-dot lasers, and as optical probes in biological systems. Different sizes of semiconductor have been found to have different emission spectra, ie, exhibiting different colors. Figure 1-4 shows some emission spectra from nanocrystals of different sizes and their corresponding colors [20, 51, 52]. The red series comprise InAs nanocrystals with diameters of 2.8, 3.6, 4.6, and 6.0 nm (from left to right), respectively; the green series include InP nanocrystals with diameters of 3.0, 3.5, and 4.6 nm; and the blue series represent different sizes of CdSe nanocrystals with diameters of 2.1, 2.4, 3.1, 3.6, and 4.6 nm. These nanocrystals can be further tailored to interact with biomolecular cells.

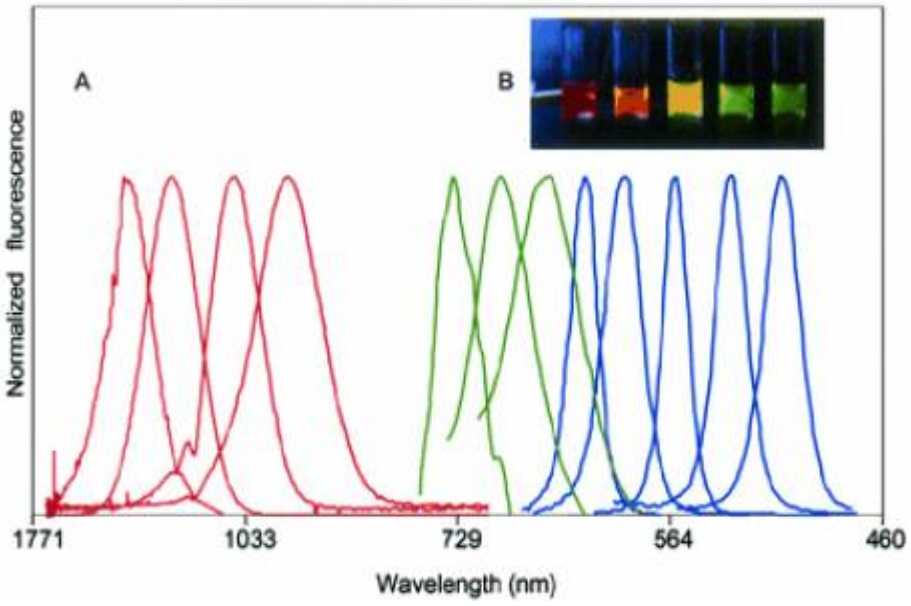

Figure 1-4 Size effect on emission spectra in visible light range[20]

It has been reported that nanocrystals coated with trimethoxysilylpropyl urea were used to bind with biotin. The penetration of nanocrystals into the nucleus membrane can be clearly seen with the naked eye.

In addition, quantum dots in the strong confinement regime have an emission wavelength that is a pronounced function of size, adding the advantage of continuous spectral tunability over a wide energy range simply by changing the size of the dots [53].

It has been reported that light emission from single fluorescing nanocrystals of cadmium selenide under continuous excitation turns on and off intermittently on a characteristic timescale of about 0.5 seconds. This intermittency is not apparent from the ensemble measurements on many nanocrystals. It was found that photoionization of the nanocrystal played an important role in this phenomenon. This finding can be further used to investigate the photophysics of the single nanocrystals[54].

With a large exciton binding energy of 60 meV, ZnO can potentially be used for efficient room-temperature exciton-based emitters. Peidong Yang et al. reported the optical properties of ZnO nanowires [55]. When the excitation intensity exceeded a threshold (about 40 kw/cm^2), lasing emission could be observed in ZnO nanowires. When the size of nanorods decreased, both emissions at 380nm wavelength and green emissions at around a 520 nm wavelength could be observed. The area density of

these short-wavelength nanolasers, which operated at room temperature, readily reached 1 x 10^{10} cm^{-2} on substrate.

1.3.3 Mechanical properties of nanomaterials

The mechanical enhancement performance of nanomaterials has attracted particular attention in composite materials. It is reported that multiwalled carbon nanotubes have a Young's modulus of 1.8Tpa [56], much higher than the highest value 800Gpa reported from bulk carbon fibers [57]. It is also found that thinner carbon nanotubes have a higher modulus.

Nanotube no.	Length (μm)	Outer diameter (nm)	Inner diameter (nm)	Young's modulus (TPa)
1	1.17	5.6	2.3	1.06
2	3.11	7.3	2.0	0.91
3	5.81	24.8	6.6	0.59
4	2.65	11.9	2.0	1.06
5	1.73	7.0	2.3	2.58
6	1.53	6.6	2.3	3.11
7	2.04	7.0	3.0	1.91
8	1.43	6.6	3.3	4.15
9	0.66	7.0	3.3	0.42
10	1.32	9.9	3.0	0.40
11	5.10	8.4	1.0	3.70

Figure 1-5 Average value of Young's modulus of carbon nanotubes [56]

When the nanomaterials with exceptional mechanical strength are incorporated into the composite matrix, the composite materials can provide superior structural properties that cannot be obtained by matrix materials alone. For example, Qian et al reported that in carbon nanotube-polystyrene composites, adding 1 wt% carbon nanotubes to the composites resulted in increase of 36% - 42% and 25% in elastic modulus and break stress, respectively [43]. During the experiment, half of the carbon nanotubes were broken and half were pulled out, clearly indicating a load transfer to the carbon nanotubes. In addition to the exceptional modulus of carbon nanotube, some other factors such as homogeneous dispersion of carbon nanotubes

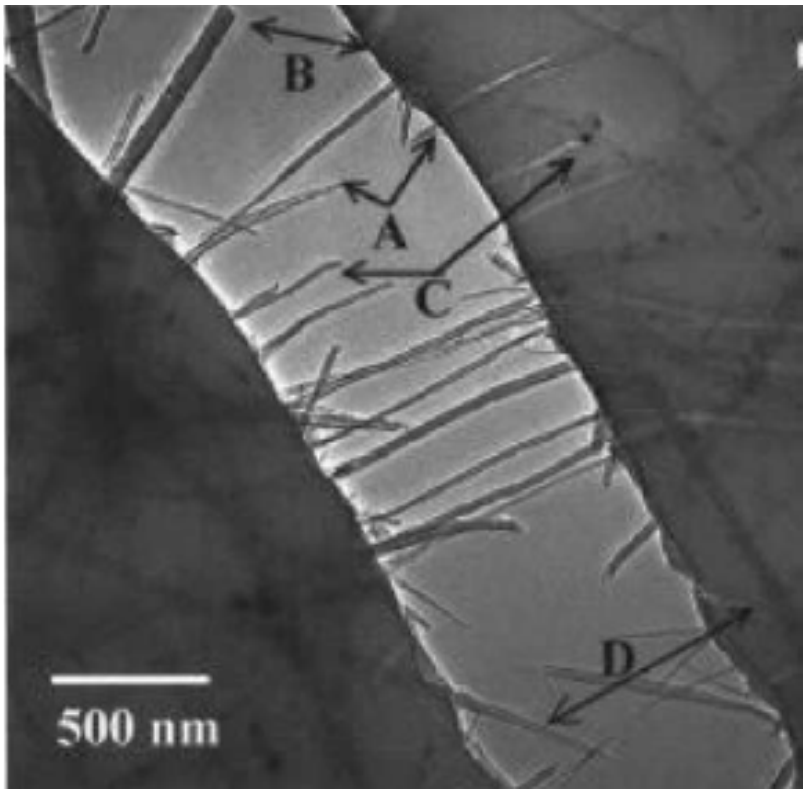

Figure 1-6 Fracture in carbon nanotube based composites [43]

throughout the matrix and high interfacial bonding between carbon nanotubes and the matrix for load transfer, need to be considered in order to fully take advantage of the exceptional mechanical properties of carbon nanotubes.

Similar to the process in papermaking, minerals are commonly added to polymers to modify the polymer matrix. It has been reported that the addition of fillers can significantly affect the properties of epoxy resin [58]. For example, adding spherical SiO_2 nanoparticles of about 50 nm in size to epoxy resin can noticeably increase fracture toughness but not tensile strength. Layered organo-modified montmorillonite improved the tensile strength of the composite significantly but fracture toughness only slightly. However, adding both the SiO_2 nanoparticles and layered montmorillonite fillers to epoxy resin produced a synergetic effect: both the toughness and tensile strength improved. The wear resistance of the composite also increased.

1.3.4 Chemical catalysis of nanomaterials

According to those involved in nanoscience and nanotechnology and in the chemical industry, catalysts, even though not explicitly mentioned, often with particle size in the range of a few nanometers, are located specifically in the nanoregime. Because the field of nanocatalysis has undergone an exponential growth during the past decade, abundant reviews regarding nanocatalysis can be found [59-63]. The

developing of a catalyst must account for several factors, particularly the size and shape of particles. It was demonstrated that transition metal nanoparticles can be synthesized with different shapes. It has been shown that the activities of platinum nanoparticles of different shapes were different for the same electron-transfer reaction in a colloidal solution [64].

With the advance of nanotechnology, catalysts with the same size and shape, factors essential for the functioning of catalysts, can be produced [65]. With nanotechnology, the simple route of catalyst development can be realized [66-69]. Another interesting phenomenon is that the reduction in size can fundamentally change the catalytic property. Gold is inert as bulk material and does not exhibit any catalytic activity. However, simply by reducing the size, nanoscale gold particles dispersed on metal oxide supports exhibit remarkable catalytic activity [70]. It has been shown that gold nanoclusters produced with laser ablation and supported could catalyze the combustion of CO.

1.4 Synthesis of Nanomaterials

Fascinated by the novel properties exhibited by nanomaterials, scientists and engineers have developed various techniques to synthesize all kinds of nanostructure materials. Many approaches, such as vapor-phase, solution-phase, electrospinning [71, 72], templating [73-76], biomimic [77, 78], and lithography [79-84], have been

developed for synthesizing 1D nanostructures. Among these methods, vapor-phase and solution processes are the two main important approaches. Vapor phase growth has been well developed and often used for the synthesis of metal and metal oxide nanostructures. Solution phase techniques, however, provide much more flexibility for synthesizing nanomaterials. The reactions in a solution phase occur at relatively low temperatures compared to the reactions in vapor phase techniques. Solution phase synthesis can be used to synthesize simple binary compounds or complicated compounds that are otherwise difficult for vapor phase synthesis [85]. The solution phase approach also involves lower cost, easy scale up, and other advantages.

1.4.1 Chemical vapor deposition method

Perhaps the most extensively used approach to producing 1D nanostructure, especially for metal oxide, is high temperature vapor-phase synthesis. The approach, a relatively mature method, has been studied by a number of authors [86-89]. It is a simple chemical process involving the reaction between metal vapor and oxidization gas, such as oxygen and nitrogen. In a typical vapor phase synthesis process, the reaction takes place inside a horizontal quartz tube placed inside a high temperature furnace. Inside the tube, source material such as metal powder is loaded in an alumina boat and put in the upstream of the tube. A substrate used for collecting the final product is placed downstream. A schematic of this process is shown in Figure 1-7. The controlling parameters for vapor phase synthesis include the temperature and the

temperature gradient inside the tube, pressure, carrier gas species and flow rate, the substrate used, the distance between the source material and the substrate, and the reaction time [86]. Depending on the manner it provides vapor, the method can be further categorized into direct and indirect vapor-phase methods.

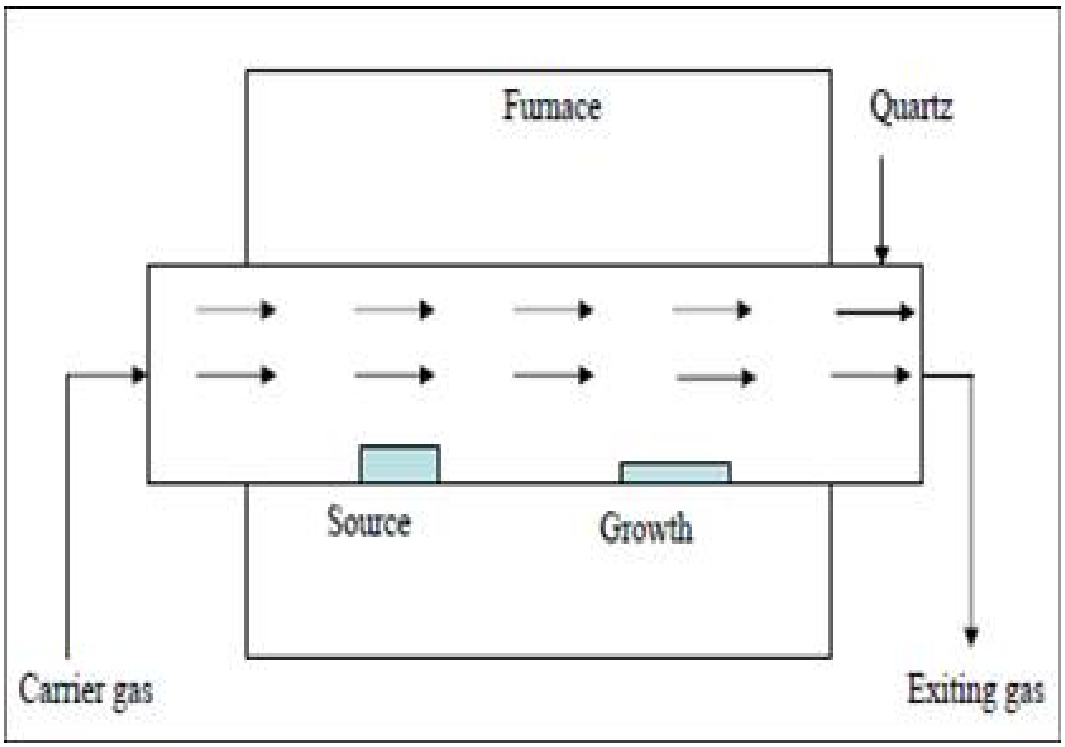

Figure 1-7 A schematic experimental setup in the vapor synthesis process

1.4.1.1 Direct vapor synthesis

In direct vapor-phase synthesis, the metal and oxidation agent are supplied directly into the reaction chamber and the metal was heated to the vapor phase and

reacted with oxidizing agent. For 1D nanostructure vapor phase synthesis, supersaturation, which is the vapor pressure of the metal, is the main controlling parameter. Supersaturation has to be controlled at a low level for 1D nanostructure growth while a medium supersaturation level is used for bulk crystal growth and high supersaturation results in powder growth [89]. The vapor phase growth methods are based on two mechanisms: vapor-liquid-solid (VLS) and vapor-solid (VS).

The VLS process is a catalyst-assisted growth that uses metal nanoparticles as nucleation seeds [90], which determine the growth direction and diameter of final 1D nanostructures. The process is initiated with the formation of liquid alloy droplets containing metal and a catalyst. The liquid alloy is supersaturated with the target metal vapor as the experiment continues. With the oxidizing gas such as oxygen flow, metal oxide is formed. A nanocluster of catalyst at the end of the 1D nanostructure, a characteristic feature of the VLS process, has been proven by TEM observation [91-93].

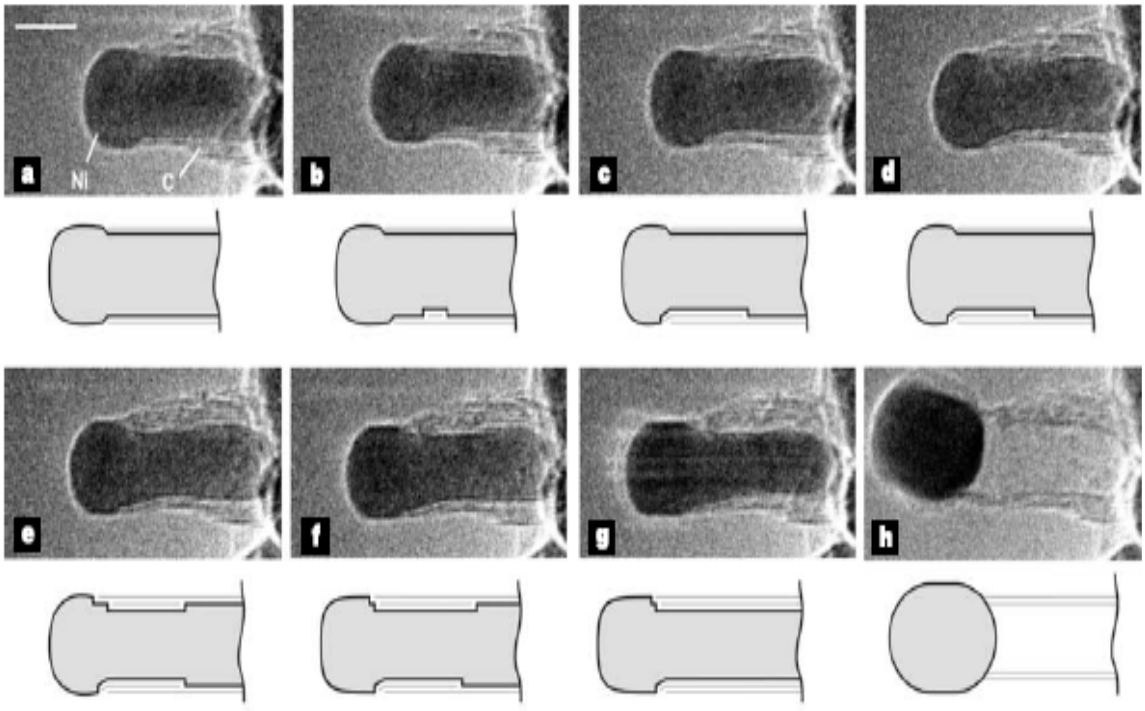

Figure 1-8 Imaging sequence of a growing carbon nanotube. The dark dot is the catalyst [91]

A general guideline for the vapor phase synthesis of a 1D nanostructure has been provided by Lieber based on the phase diagram from which both the catalyst and operation conditions can be determined at the same time [28]. For example, for silicon nanowire growth, two different catalysts could be used: Au and Fe. The phase diagram in Figure 1-5 of the Au-Si binary system suggests that nanowire growth should occur at temperatures slightly higher than 363 ^{o}C, more than 800 ^{o}C lower than in the case of the Fe- based catalyst. Moreover, the solid nanocluster catalyst observed upon termination of growth should be an Au metal, not an Au-Si alloy. The experimental results agree well with these predictions. It was observed that single-

crystal Si nanowires could be produced at temperatures between 370 and 500 ^{o}C with diameters as small as 3 nm.

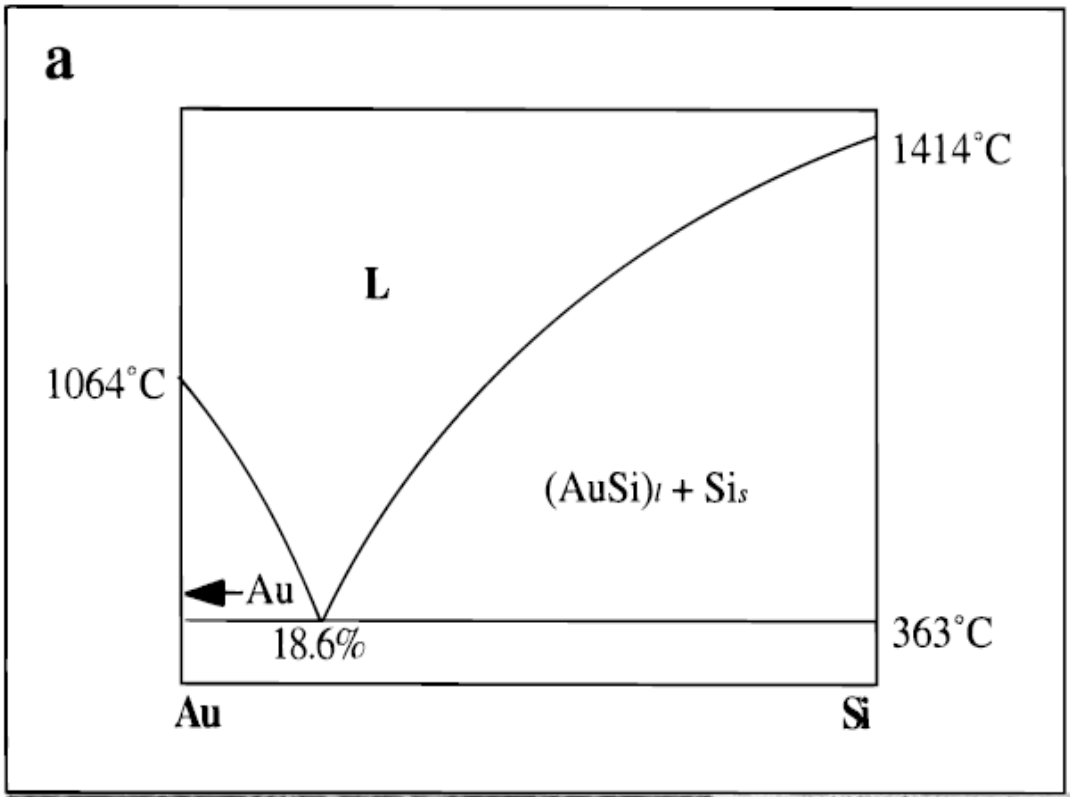

Figure 1-9 Phase diagram of Au-Si binary system[28]

The VS and the VLS processes are similar, but the former does not require a catalyst. However, the process is not yet well understood. In addition to the presence of a catalyst, the difference of between VS and VLS is that the metal vapor directly is condensed on the substrate located in the low temperature region. Once it is condensed, it serves as a nucleation seed [94, 95]. After the nucleation seeds are formed, the nanomaterial grows in a way similar as it does in the VLS process.

1.4.1.2 Indirect vapor phase synthesis

Another common method for 1D nanostructure growth is indirect vapor-phase synthesis. In this approach, intermediates or precursors are usually involved. In many cases, decomposition and other types of side reactions also need to be taken into consideration, so this method is a more complicated synthesis process than the simpler CVD process. For example, Yang and colleagues reported a synthesis method for preparing MgO nanowires via a carbonthermal reduction process. First, they reduce MgO to Mg vapor by producing a reaction with carbon. The Mg vapor was then transported to the surface of condensation substrate, and oxidized to form MgO again [96]. The advantage of this two-step process is that the supersaturation of the Mg vapor could easily be controlled by the reaction rate between MgO and carbon so that the 1D MgO nanowire could be prepared. Another example of indirect vapor phase growth is MOCVD, in which the source metal is provided from the metal organic compounds [97].

Similar to CVD growth process is the laser ablation process. They differ with regard to the way they produce metal vapor. In the latter process, metal vapor is generated by ablating a piece of metal with a laser while the metal is directly heated to the vapor phase of the CVD process. The growth mechanism of laser ablation still follows the VLS or VS process [98].

1.4.2 Solution phase synthesis

Compared to vapor phase synthesis, solution phase growth requires much lower temperature, resulting a lower synthesis cost. Due to the vast availability of solvents and solutes, solution phase synthesis can be carefully designed to carry out the synthesis of materials from elements such as gold and platinum, to binary compound such as TiO_2[99-101], ZnO[102-105], and CdTe [106], to complicated compounds such as barium titanate ($BaTiO_3$) [107, 108] and magnesium hydroxide sulfate hydrate[109]. On the other hand, vapor phase synthesis is quite limited to simple materials such as metal elements or metal binary compounds. A series of morphologies have been successfully synthesized with this approach. A number of solution phase syntheses have been developed to synthesize 1D nanomaterials, including coprecipitation, microemulsion, hydrothermal, and template-assisted synthesis. Due to the complexity and non-ideality of the reaction conditions, the mechanism of nanostructure growth is less understood.

1.4.2.1 Coprecipitation

Coprecipitation is a process involving a series of steps that include nucleation, growth, and coarsening. Due to the complexity of these steps, a fundamental understanding of coprecipitation is not yet available. However, the process is

described in the following brief overview: 1) Desired products are generally sparingly soluble in a certain solvent. 2) Supersaturation is a deterministic factor in the growth of the products. 3) High supersaturation leads to nucleation to form a large number of clusters or nuclei. 4) The clusters grow into crystals as ions or molecules are supplied to the crystals. 5) Secondary growth processes such as Ostwald ripening or aggregation can dramatically affect the size and morphology of the final product.

Various nanoparticles such as elemental metal and metal oxide have been synthesized with the coprecipitation method. For example, different-sized silver nanoparticles can be synthesized by reducing the silver nitrate with different agents. Particles 3-5 nm and those 15-26 nm in diameter can be obtained if sodium borohydride [110] and ascorbic acid[111], respectively, are the reducing agents. Coprecipitation can be achieved in a nonaqueous medium. It has been reported that gold nanoparticles were synthesized from reducing chloroauric acid ($HAuCl_4$) using formamide as a reducing agent and the poly(vinylpyrrolidone) (PVP) as a stabilizer. The reaction can take place at room temperature. It is believed that the nonaqueous solvent can reduce the aggregation and control the size of the final product [112].

1.4.2.2 Microemulsion

Micelles are aggregates of dispersed surfactants when the surfactant concentration is greater than the critical micelle concentration (CMC), which is the

concentration when adding more surfactant can not further reduce the surface tension of the system. In polar media such as water, the hydrophobic parts of the surfactants tend to locate away from the polar phase while the hydrophilic parts of the surfactant will point toward the solvent interface. Micelles can also be formed in nonpolar media such as benzene in which the hydrophobic parts point out toward the solvent and the hydrophilic parts point inward, forming an assembly known as a "reversed micelle". A micelle or reversed micelle may take several forms, such as spheres, disks, or rods, depending on the composition of the surfactant molecules and the conditions of the aqueous system [113].

Having unique properties, micelle can dissolve in both hydrophobic and hydrophilic compounds. Due to the duality of solvent, they have been used as microreactors [114, 115]. They also have been used as templates which will be summarized in a later part of this thesis. When a reverse micelle containing dissolved metal salts is mixed with another micelle containing a suitable reducing agent, the metal ions can be reduced to produce element metal. Barium hexaaluminate 3-10 in size were synthesized with reverse micelle and used for the catalytic combustion of methane [116]. Due to the weak interaction between the solvent and the reactant, reverse micelles can be used to control the size of the final product. With this method, magnetic iron oxide nanoparticles ranging from 2 to 9nm were also reported [117].

1.4.2.3 Hydrothermal synthesis

The solvothermal method is a method that takes advantage of the properties of supercritical fluids which is a fluid that is heated at elevated temperature and pressure above its boiling point and that exhibits both liquid and gas properties. The interfacial tension is greatly reduced and mass transfer between different phases is enhanced. When the solvent is water, it is commonly referred to as "hydrothermal". Although some synthesis did take place under supercritical conditions [118, 119], most of the nanomaterial syntheses were simply carried out at much lower temperatures and pressure.

Many important nanomaterials such as TiO_2, ZnO[120-122] and CdTe[123, 124] have been synthesized using this method. Nanostructured titania, one of the most important photocatalysts, has been synthesized extensively with hydrothermal method. Walsh systematically investigated the effects of hydrothermal conditions on TiO_2 nanotube growth [125]. It was found that the diameters of the nanotubes depended on the reaction temperature and ratio of reactants, and higher temperatures resulted in large nanotubes and wide size distribution. Some researchers took advantage of high temperature and converted amorphous TiO_2 into anatase or rutile crystallite TiO_2 using different acids as catalysts under hydrothermal conditions [126]. With citric and nitrate acid, nanorods the in rutile phase could be obtained and HF could convert amorphous TiO_2 to the anatase phase.

1.4.2.4 Template assisted

Another approach to nanostructure synthesis is to use the existing nanostructures, referred to as "template synthesis". Many templates such as polymeric membrane, self-assembled molecular structure [127, 128], existing nanostructures synthesized from other approaches [129], and even DNA [130-132] have been developed for the purpose of synthesizing nanostructure materials. Among these templates, anodic aluminum oxide (AAO) and polymers are the two commonly used templates. AAO, a membrane with ordered channels, was immerged into the reaction system during synthesis, and then the reaction solution was deposited into the pores of the AAO membrane by an electrochemical method. After that, the AAO membranes could be dissolved in the NaOH solution to obtain the desired nanowires [133, 134]. Because of their easy processibility, polymer materials can be used as templates. They either act as sacrificial templates when synthesizing a hollow structure or as a directing agent. Caruso reported a technique for fabricating hollow SiO_2 nanospheres [73]. In this technique, polystyrene spheres were used as templates and SiO_2 particles were then coated on the polystyrene surfaces through poly(diallyldimethylammoniumchloride) (PDADMAC). Calcination of the coated spheres led to the formation of a hollow sphere of silica. Similarly, gold core-shell structure was synthesized using polystyrene as the core template [73, 135].

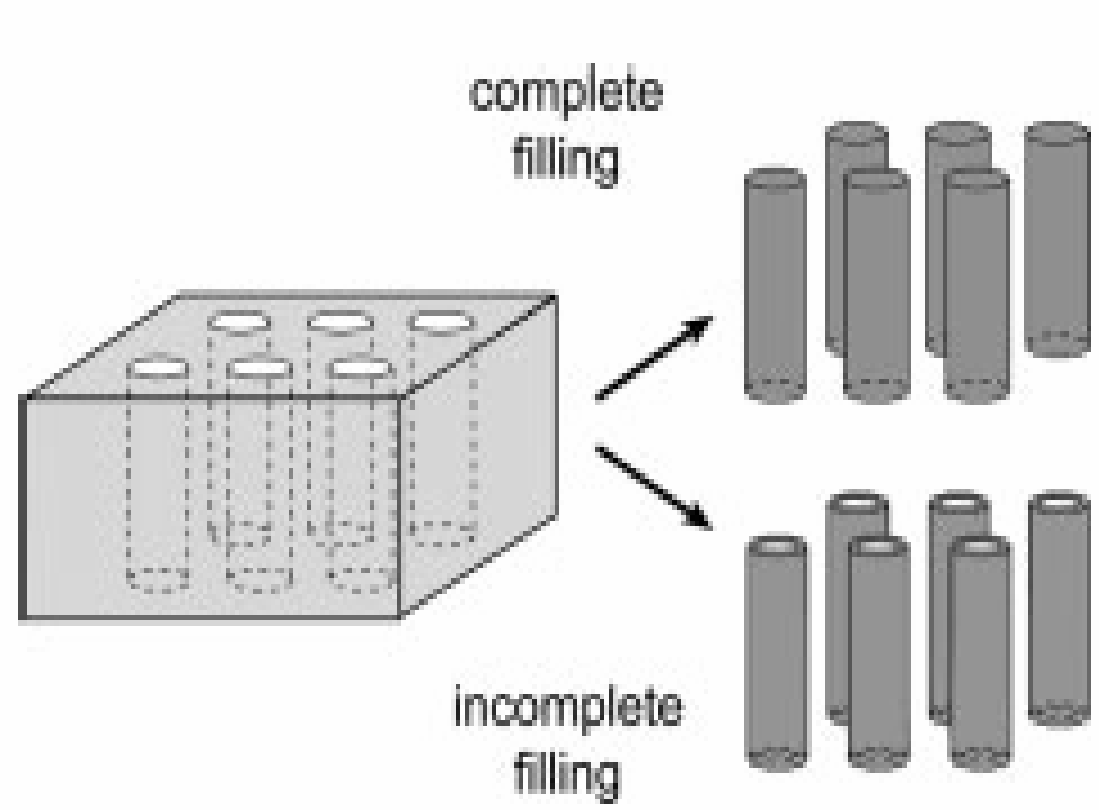

Figure 1-10 Schematic illustration of 1D nanomaterial synthesis using templates.

1.5 Theories of Nanomaterial Growth

The basic process of 1D nanostructure formation is crystallization, a process that has already been investigated for hundreds of years. Nevertheless, little quantitative information is known about crystallization [89]. The growth of a solid from a vapor, liquid, or solid phase basically consists of two fundamental steps:

nucleation and growth. In the first step, there is an absence of any solid phase, when the concentration of the building blocks (atoms, ions, or molecules) of a solid becomes sufficiently high, that is, the solution is supersaturated. At this point, the building blocks tend to aggregate into small clusters (or nuclei) due to their thermodynamic instability. With a continuous supply of building blocks, these nuclei can serve as seeds for further growth to form, or the formation of larger structures. In addition, the building blocks also need to be supplied at a well-controlled rate in order to obtain crystals which possess a homogeneous composition and uniform morphology.

1.5.1 Nucleation

The fundamental driving force for crystallization is the difference between the chemical potential of the solution and that of the crystal, which can be written as:

$$\Delta\mu = \mu_s - \mu_l \qquad (1.1)$$

where μ_s and μ_l are the chemical potentials of the crystal and the solution, respectively.

The chemical potential can be defined with the reference of μ_0 and the activity, and the driving force for phase transformation is shown in equation (1.2)

$$\mu = \mu_0 + RT\ln(a) \qquad (1.2)$$

where R is gas constant and T is the absolute temperature.

$$\Delta\mu = RT\ln(a/a^*) \approx RT\ln(c/c^*) = RT\ln(S) \quad (1.3)$$

where c and c* are the real and equilibrium concentration of the solute, respectively. In an ideal solution, the activity can be approximated with the concentration. S is supersaturation, defined as c/c*.

It can be seen from the above equation (1.3) that, the driving force $\Delta\mu$ is positively correlated with supersaturation. The supersaturation effect on nucleation has been well documented [136, 137] in studies that have shown that it has to reach a certain level before nucleation can take place in a practical way. Table 1-2 shows the estimation of the time scale for nuclei formation in supercooled water[137]

Table 1-2 Estimation of time for nuclei formation in supercooled water

Supersaturation	Time
1.0	∞
2.0	10^{62} years
3.0	10^{3} years
4.0	0.1 seconds
5.0	10^{-13} seconds

In order to synthesize 1D nanomaterials, the supersaturation level has to be finely controlled. It is generally accepted that the building blocks should be able to move back and forth between the crystal surfaces and the solution phase during the synthesis of nanomaterials. If supersaturation S is high, then the system mainly experiences the nucleation stage and monodispersed particles will be obtained.

The free energy of the system includes work needed to create the new solid phase,(i.e. nuclei), and work created by surface tension due to the new emerging solid phase. If we assume the nuclei take the form of a sphere, then

$$\Delta G = \frac{4}{3}\pi r^3 \Delta Gv + 4\pi r^2 \gamma \qquad (1.4)$$

where r is the radius of the spheres, ΔGv is the energy change in transformation per unit volume, and γ is interfacial tension.

The two terms have opposite sign: ΔGv is negative, and the interfacial tension is positive. Therefore, ΔG has a maximum.

$$d\Delta G / dr = 4\pi r^2 \Delta Gv + 8\pi r\gamma = 0 \qquad (1.5)$$

$$r^* = -\frac{2\gamma}{\Delta Gv} \qquad (1.6)$$

The relationship among supersaturation, particle size, and interfacial tension has been derived as:

$$\ln(S) = \frac{2M\gamma}{RT\rho r} = \frac{2\gamma v}{K_B T r} \qquad (1.7)$$

where M is the molecular weight, R is the gas constant, K_B is the Boltzmann constant, and v is the molecular volume. Thus,

$$\Delta Gv = -\frac{K_B\ T\ Ln(S)}{v} \qquad (1.8)$$

Put back into equation (1.4), it becomes

$$\Delta G = -\frac{4\pi r^3}{v} K_B T \ln(S) + 4\pi r^2 \gamma \qquad (1.9)$$

If the particle size is bigger than this equilibrium size, ΔG becomes more negative and the particles can grow; for nuclei smaller than this size, ΔG is positive and particle will dissolve. It is noted that higher supersaturation will result in a smaller equilibrium size, as shown in Figure 1-11.

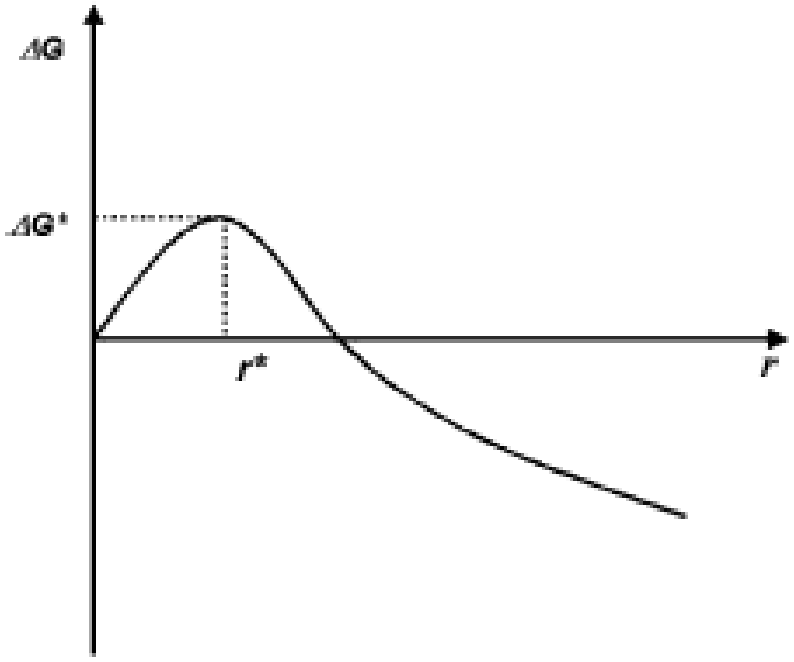

Figure 1-11 Qualitative relationship between overall free energy and radius

1.5.2 Crystal growth theories

After the nucleation stage, the nuclei start to grow into bigger particles. The morphology of a crystal is dependent on the internal structure of crystals such as space groups and intramolecular and intermolecular bonding, and external growth conditions such as temperature, supersaturation, and impurities. Supersaturation has been considered an effective technique to control crystal morphology. Many theories that explain the crystal growth have been developed to [137]. Among these theories, the Hartman and Perdok (HP) theory [138-140], the Burton-Cabrera-Frank (BCF) theory[141], and the kinematics theory are the most popularly accepted ones.

1.5.2.1 HP Theory

HP theory is also known as periodic bond chain (PBC) theory. This theory is based on the surface energy that is present during crystal growth. Gibbs suggested that the sum of surface free energies of each surface should be minimized during the growth from its surroundings. This principle is an extension from a liquid droplet, the surface energy of which has to be minimized to be stable. However, Gibbs theory cannot be used practically for crystal growth for several reasons: For one, the crystal growth is not a reversible process. In addition, the surface free energy of a particular

crystal surface can not be measured or calculated. Finally, the theory does not take into account of supersaturation which is a known factor in crystal morphology control.

In studies of using surface free energy, Hartman and Perdok adopted attachment energy, energy released when a building block forms bonds with a crystal surface. The higher the attachment energy, the faster the building block forms bonds with crystal surface. Therefore, the growth rate of a crystal surface with high attachment energy is higher than that with low attachment energy. Then a vector called periodic bond chain (PBC), which represents the strongest bonds in the crystal, is introduced. Based on the growth rate of the crystal faces, crystal surface were divided into three groups: F faces, which are parallel to two vector components of the PBC vector; S faces, which are parallel to the one component of the PBC vector, and K faces, which are not parallel to any component of the PBC vector. F faces, which need to release a smaller amount of energy since few bonds are needed to form strong bonds, have the lowest growth rate while the K faces have the highest growth rate. Therefore, F faces will determine the final morphology of the crystal. HP theory has predicted some crystal morphology successfully, but its main drawback is that it does not account for the environmental factors of crystal growth such as supersaturation, a known factor influencing the morphology of crystal growth.

1.5.2.2 BCF theory

The BCF theory is based on the thermodynamic reasoning about an adsorption layer on a crystal surface during the growth process. When building blocks of crystal arrive at a particular crystal face, they are not integrated into the lattice immediately. Those building blocks can move freely on the surface to make a loose adsorption layer on the crystal surface, forming a dynamic equilibrium between the adsorption layer and the bulk solution. Based on the adsorption layer assumption and through Boltzmann statistic reasoning, Burton, Cabrera, and Frank proposed a kinetic theory describing the crystal growth process as follows [141]:

$$R = A\sigma^2 \tanh(B/\sigma) \qquad (1.10)$$

where R is the crystal growth rate and σ is relative supersaturation, defined as σ = S-1= c/c*-1. A and B are complex constants that are temperature dependant and include intrinsic crystal structure parameters.

The relationship between supersaturation and crystal growth is depicted in Figure 1-12.When supersaturation is low, crystal growth rate $R = A\ \sigma^2$; at high supersaturation, it is approximated to a linear relationship with σ.

In practice, the BCF theory is difficult to apply due to the following reasons:

1. The original theory was derived for crystal growth from vapor. It is speculated that it can be applied to the solution system, but the relationship are very difficult to quantify due to the complexity of solution systems.

2. Ion hydration could alter the growth pattern of crystal from that of vapor.

3. Little is known about the adsorption layer and its behavior on crystal surfaces.

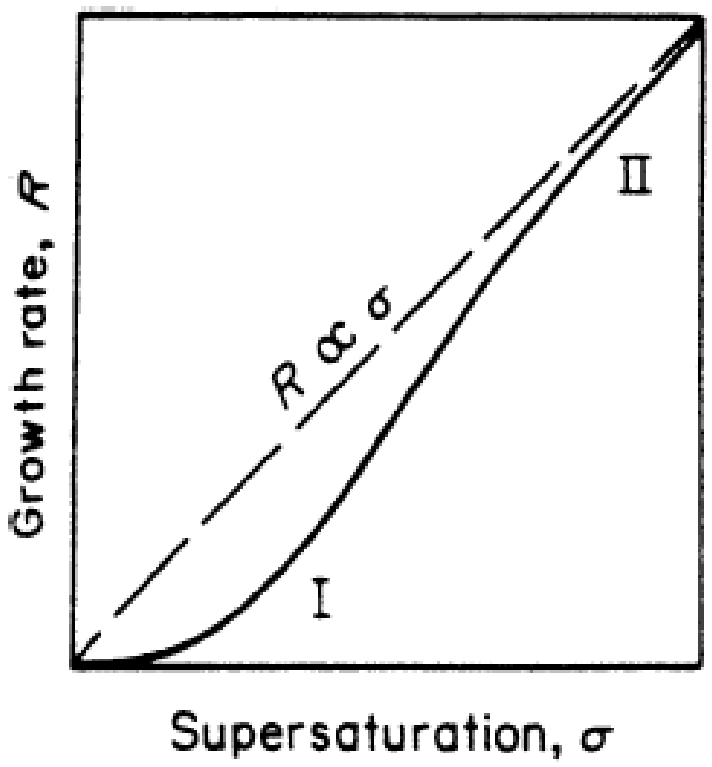

Figure 1-12 Qualitative relationship between growth rate and supersaturation[141].

1.5.2.3 Kinetic theory

In light of the adsorption layer, a new theory was proposed: the crystal growth process. The process consists of two steps: a diffusion step and a reaction step, as shown in the schematic figure(Figure 1-13). In the diffusion step, the building blocks diffused through a boundary layer between the crystal surface and the bulk solution to arrive at the crystal surface; in the reaction step, the building blocks on the crystal surface integrate into the crystal lattice. The two steps can be written mathematically as

$$\frac{dm}{dt} = k_d (C_B - C_i) \qquad (1.11)$$

$$\frac{dm}{dt} = k_r (C_i - C_s) \qquad (1.12)$$

where C_B, C_i, and C_s are the concentration of the bulk solution, the boundary layer, and the crystal surface, respectively. k_d is the mass transfer coefficient and k_r is the reaction constant.

The above equations are not easy to use in practice because little is known about the boundary layer. The C_i is often eliminated, so only the net driving force,

C_B-C_s, is considered in the equation. The above equations can be rearranged as following after the C_i is eliminated as follows:,

$$\frac{dm}{dt} = k(C_B - C_S)^n \qquad (1.13)$$

where k is the overall crystal growth coefficient and n is the order of the crystal growth.

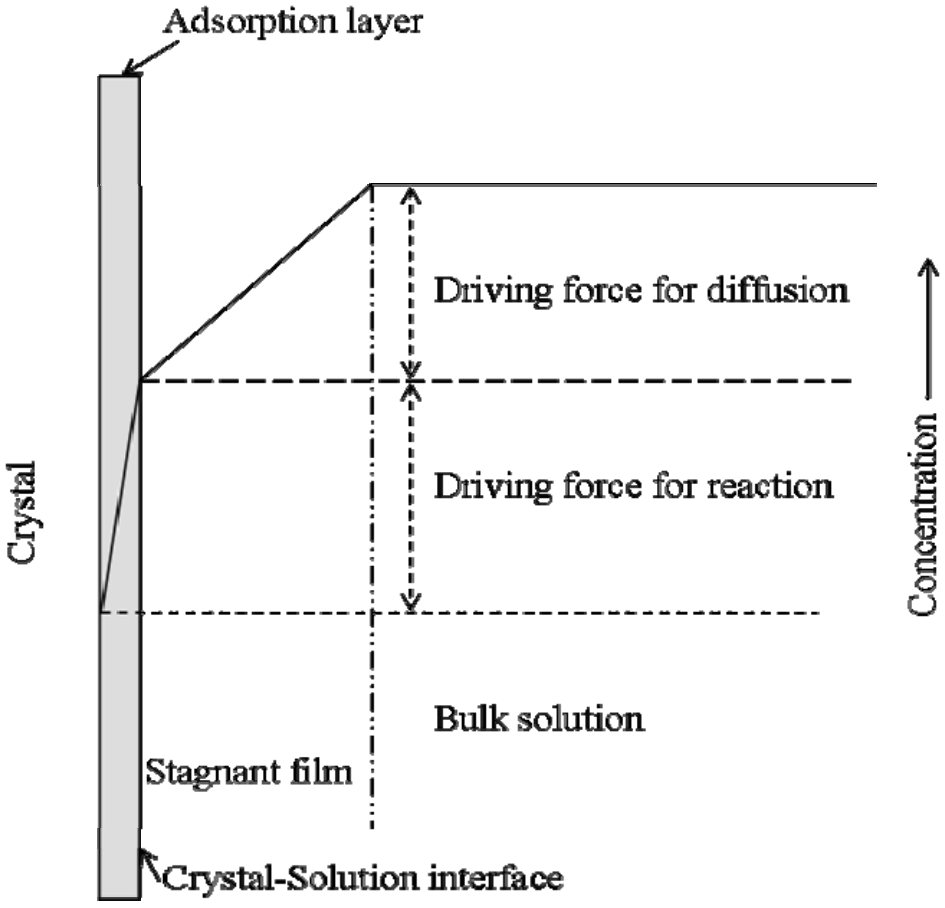

Figure 1-13 Simple diffusion-reaction model of crystal growth

1.5.2.4 Crystal individual surface growth rate

For one dimensional growth, the growth rate of each face of the crystal is different. It is generally accepted that high energy surfaces grow fast and eventually disappear during the crystal growth process. The following equation can be applied for 1D nanomaterial growth:

$$\frac{dR_{hkl}}{dt} = k(C_B - C_{S,hkl})^n \qquad (1.14)$$

where R_{hkl} is the growth rate of the (hkl) surface, and $C_{s,hkl}$ is the concentration on the (hkl) surface. However, in practice, it is difficult to control the growth rates of each face separately. It is known that supersaturation may even take different values for different crystal faces and even may change along the same face [142-144]. To date, the specific control of supersaturation on certain surfaces still remains a challenge.

In spite of all these available theories, a mechanistic understanding of nanocrystal growth still remains elusive, true partly due to its various reaction mechanisms. In the theories mentioned above, only a few parameters for each theory are taken into accounts. Crystal growth is a far more complex process that can be described by these models. Furthermore, the parameters involved in the theories are difficult to measure or control or estimate. As a result, in practice, a trial-and-error

approach is still used in the crystal growth process with some vague guidelines from these theories.

Using calcium carbonate as a model system, Katz studied the effect of supersaturation on calcite crystal growth using the kinetic model [145]. It was found that a simple kinetic model could correlate supersaturation to crystal growth adequately. The process of the crystal growth depended on the solution composition. They further found that at the same supersaturation condition, adding an inhibitor, could change the rate-limiting step of the growth and then the growth rate.

Luo et al. investigated the control morphology through supersaturation [146]. When different supersaturation conditions were used, different morphologies could be obtained for barium sulfate. High supersaturation resulted in nucleation with a narrow particle size distribution while low supersaturation produced large crystals. In the medium supersaturation range, multiple morphologies were observed, illustrating the complexity of supersaturation control on morphology. It was reported that a small fluctuation in supersaturation could significantly change the crystal growth rate of each face and the final morphology [143].

Chapter 2 : Challenges and Research Objectives

2.1 Problem Statement

As previously reviewed, one-dimensional nanomaterials, with their unique properties, show great potential applications in electronics, electrophonics, and composite materials. The paper industry, in particular, can take the advantage of the exceptional mechanical strength and unique optical properties exhibited from nanofillers. However, to fully take advantage of 1D nanomaterials, we must address several issues related to 1D growth of nanomaterials. First of all, those nanomaterials should be produced at a reasonable low cost and at large scale, which to date cannot be achieved by any process. However the first part of the thesis addressed this problem by showing that a new filler magnesium hydroxide sulfate hydrate could successfully be synthesized at a with relatively low cost and on a large scale. Second, the synthesis of a desired particle size and morphology necessitates a fundamental understanding of nanocrystal growth. Previous studies have shown that the growth of nanocrystals can be controlled in certain areas, but the results have been far from satisfactory. Thus, the factors affecting the nanocrystal growth need to be carefully examined. In this thesis, we focus on the investigation of the effect of supersaturation on the growth of nanocrystals since it is the deterministic factor in this process. Some other factors such as temperature and agitation were studied as well.

2.2 Problem Analysis

The main objective of this thesis is to 1) synthesize nanomaterials as potential nanofillers on a large scale and at a low cost. 2) investigate the effect of supersaturation on the growth of 1D nanostructure. To synthesize nanomaterials at a low cost, the process has to be simple and easy to operate. The study of the effect of supersaturation calls for careful control of the supersaturation level in the synthesis. Two commonly used methods to control supersaturation are heating and cooling, but changes in temperature makes the process even more complicated since the growth kinetics are dependent on temperature. Using a dropwise method is obviously unsuccessful because local supersaturation is difficult to control to an desired low level and a sharp increase in local supersaturation may result in undesired crystal growth. Therefore, a new technique for controlling supersaturation at desired level needs to be developed. In addition, the relationship between supersaturation and 1D crystal growth should be studied.

2.3 Goal of This Thesis

The main objectives of the thesis are to:

- develop a method for large-scale synthesis of 1D nanomaterial in a solution in an economical way

- investigate the supersaturation effect on 1D nanomaterial growth for magnesium hydroxide sulfate hydrate nanobelts
- develop a kinetic model that describes the 1D nanomaterial growth for the ZnO nanorods
- explore the effect of other process factors such as temperature and agitation on ZnO nanorod crystal growth.

The overall organization and topics addressed to the above objectives will be presented as follows. In *Chapter 3* describes a new effective method of synthesizing magnesium hydroxide sulfate hydrate nanobelts is described. The MHSH nanobelts can be synthesized on a large scale at a relatively low cost, and in their final state, they will be relatively pure. To control the supersaturation level in the solution, the method will use sparingly soluble carbonate salts. *Chapter 4* further demonstrates the control of supersaturation using sparingly soluble salts through application to another reaction system in which ZnO nanorods were synthesized using carbonate salts as supersaturation control agents. At low supersaturation, the nanorods could be produced while higher supersaturation resulted in a platy morphology. Similarly process conditions have significant effect impact on the synthesis. Chapters 3 and 4 both together demonstrate the importance of supersaturation level in nanomaterial synthesis and supersaturation can be controlled through sparingly soluble carbonate salts. *Chapter 5*, develops a kinetic model for 1D ZnO nanorod growth. The controlled synthesis of ZnO nanomaterials has both scientific and industrial

significance. By developing a kinetic model for ZnO nanorod growth, we provided some insight into the synthesis of nanomaterials and provide an opportunity for better control of the synthesis of other new materials. *Chapter 6* presents the synthesis of another important category of nanomaterials: ZnO nanospheres. In this chapter, ZnO nanospheres were synthesized using hexamethylenetetramine (HMT) and $Zn(NO_3)_2$. This synthesis demonstrated that process parameters other than supersaturation could significantly affect nanomaterial growth, complicating the growth of nanomaterials. *Chapter 7* summarizes the research results for this thesis and includes discussion of future work in nanomaterial synthesis.

Chapter 3 : Synthesis of Magnesium Hydroxide Sulfate Hydrate Nanobelts*

3.1 Introduction and Objectives

It has been a common practice in papermaking process to add inorganic particles to improve the opacity, brightness, and printability of paper. Besides the paper industry, industries such as the paint and polymer industries also commonly use filler. It is well known that adding an inorganic substance to a polymer matrix resin in also improves the its properties, such as rigidity, mechanical strengths, heat resistance and so on [147-151]. Among these particles, the whisker or fiber form particle has attracted considerable interests. Fibrous silicate [5] and precipitated calcium carbonate [152] have been synthesized and tested in papermaking. Magnesium hydroxide sulfate hydrate (MHSH) has proven to be an effective filler for resin, filler, filter medium, fire retardant , and reinforcement of polymers and plastics [153-157]. Various chemical routes based on hydrothermal conditions have reported to synthesize MHSH particles or whiskers[154, 155, 158]. In the typical hydrothermal

*This chapter has been modified from the following publications: a) Z. Zhou, Q. Sun, Z. Hu, and Y. Deng, *Nanobelt Formation of Magnesium Hydroxide Sulfate Hydrate via a Soft Chemistry Process*, Journal of Physical Chemistry B, V110, 13387-13392, 2006 b) Z. Zhou and Y. Deng, *Solution Synthesis of Magnesium Hydroxide Sulfate Hydrate Nanobelts Using Sparingly Soluble Carbonate Salts as Supersaturation Control Agent*, Journal of Colloid and Interface Science, (2007), 316, 183-188

process, $MgSO_4$ and Ammonia or NaOH were first mixed together first and then the newly-formed mixture $Mg(OH)_2$ was transferred to an autoclave which was then sealed and heated to about 150-200^oC for certain hours. Finally, the precipitated particles were washed and analyzed. However, these existing methods use high temperature and result in low aspect ratios. Therefore, a new method is needed to synthesize MHSH on a large scale at a low cost.

In this chapter, we developed a new method of synthesizing magnesium hydroxide sulfate hydrate (MHSH) nanobelts. The reaction was carried out at ambient pressure with mild reaction temperature (~100 °C), in sharp contrast to those requiring higher temperature (usually ≥ 160 °C) and higher pressure reported in the previous MHSH whisker's preparation. The MHSH nanobelts were characterized with various methods that investigated their morphology, structure, and thermal behavior. Scanning electron microscopy (SEM) observations showed that the MHSH exhibited a nanobelt morphology with a thin belt structure (~50 nm in thickness),a rectangular cross section (~200 nm in width), and a length of up to one hundred micrometers. X-ray diffraction (XRD), energy dispersion X-ray spectra (EDS), selected area electron diffraction (SAED), and transmission electron microscopy (TEM) analysis revealed that the MHSH nanobelts possessing a single crystal form. The MHSH nanobelts underwent decomposition under electron beam irradiation during TEM observation and formed MgO with the pristine nanobelt morphology preserved. The thermal decomposition was further investigated with thermal

gravimetric analysis (TGA). The influence of the reaction parameters, such as the molar ratio of reagents, the reaction temperature, the stirring mode, inert gas bubbling, and so forth, on the nanobelt formation was also examined. Finally a chemical reaction mechanism and growth process of nanobelts were proposed.

The objective of this part of the study is to present 1) the low cost and large-scale synthesis of nanofillers, 2) the supersaturation effect on the nanobelt growth; and 3) the supersaturation level controlled using sparingly soluble carbonate salts. These experiments demonstrate that low supersaturation enhance the growth of nanobelt. However, as high supersaturation results in irregular particles, in this synthesis, the supersaturation level is controlled through sparingly soluble carbonate salts. Because of their low solubility, carbonate salts are ideal buffer solutions for providing counter ions, namely OH^-, which coprecipitate the product. The same approach can be used to synthesize other 1D materials.

3.2 Materials and Methods of Synthesis

Materials: Magnesium sulfate heptahydrate, $MgSO_4 \cdot 7H_2O$ (98%) and $CaCO_3$ (>99%) were purchased from Aldrich Chemical Company, Inc and used without further treatment. All other reagents were from Sigma-Aldrich and used as received. The deionized (DI) water was in mili-Q grade with a conductivity of 18 $m\Omega\ S^{-1}$.

Synthesis of MHSH Nanobelts: A prototypical procedure is described below. 24.65 g (about 0.1 mol)of magnesium sulfate heptahydrate $MgSO_4 \cdot 7H_2O$, 0.1 g of sodium carbonate $CaCO_3$ (0.01 mol) and 250 ml DI water were added to a 250 ml three-neck round-bottom flask. An air-inlet bubbling tubing was inserted into the flask and a refluxing column was added to it as a cooler. The solution in the flask was then heated to its boiling temperature (~100 °C) while gentle agitation was maintained with a magnetic stirrer. The compressed air at a pressure of 0.5 psi was charged at a speed of 20 l/hr and bubbled through the inlet tubing in the mother liquor. The reaction was maintained for 48 hours. When the reaction was complete, the suspension was filtered and washed extensively with DI water to remove the excess magnesium sulfate and other water soluble impurities. The final product was dried in a vacuum oven at 60 °C overnight and a white powder was obtained.

3.3 Characterization

SEM observation was conducted on an LEO 1530 thermally-assisted field emission (TFE) scanning electron microscope. Prior to the observation, the samples were lightly sputter coated with a thin layer of Au. The EDS spectra were recorded on the LEO 1530 TFE SEM machine with the same manipulation parameters. SAED and TEM analysis were carried out on a JEOL 100C type TEM machine with an accelerating voltage of 100 kV. XRD patterns were recorded on a PW 1800 X-ray

diffractometer (Philips, USA) using Cu K_α ray (λ = 1.54 Å) as the radiation source. A step size of 0.01° and a scan step time of 0.5 s were used to record the spectra in a range of 2θ from 0.2–80°. Thermogravimetric analysis (TGA) was done on a Seiko TG/DTA 320 in a nitrogen atmosphere at a heating rate of 10°C/min.

3.4 Results and Discussion

3.4.1 Observation of the morphology

Figure 3-1 shows the morphology of the final products, which exhibit a belt shape 20~50 nm thick and 200-300 nm wide. The nanobelts have a long, curled morphology. The length of the nanobelt estimated from the SEM graph is in the range of tens to one hundred micrometers. It was observed that some nanobelts displayed several branching points either splitting from the sub-unit in the center of the nanobelt or separating as two individual branches of belts, as shown in Figure 3-2. It was noted that the surface appearance of the nanobelts was not smooth but presented a wave-like morphology. It was also observed that one nanobelt consisted of a bunch of nanowires, and each nanowire had a diameter about 50nm in diameter, which approximately equals the thickness of one nanobelt.

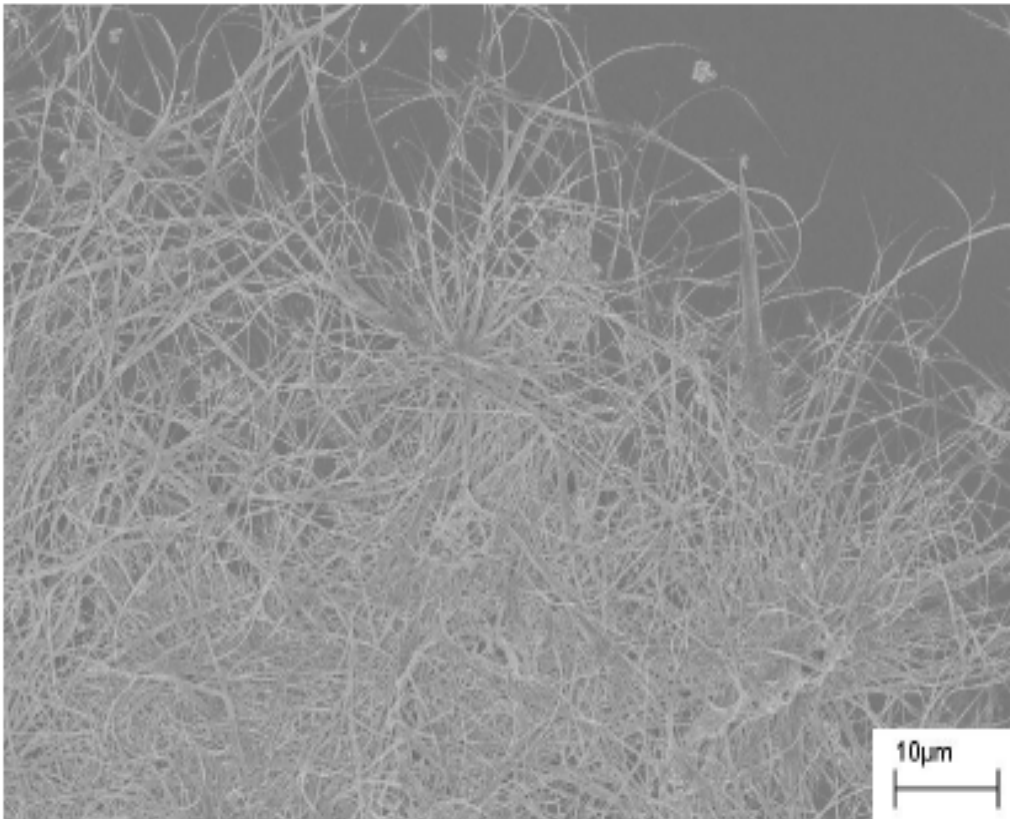

Figure 3-1 SEM micrograph of the MHSH final product

Figure 3-2 further reveals the surface unevenness of the MHSH nanobelts compared to that of ZnO or MgO cousins via a CVD process with a smooth and even surface morphology. When a high shear force was applied to the final products, it could cut the nanobelts into short needles, but it could not separate the nanobelt bundle, suggesting that the individual nanowires in the nanobelt were strongly bonded together by chemical bonds. Figure 3-2 also shows several irregular particles which maybe carbonate salts that did not react..

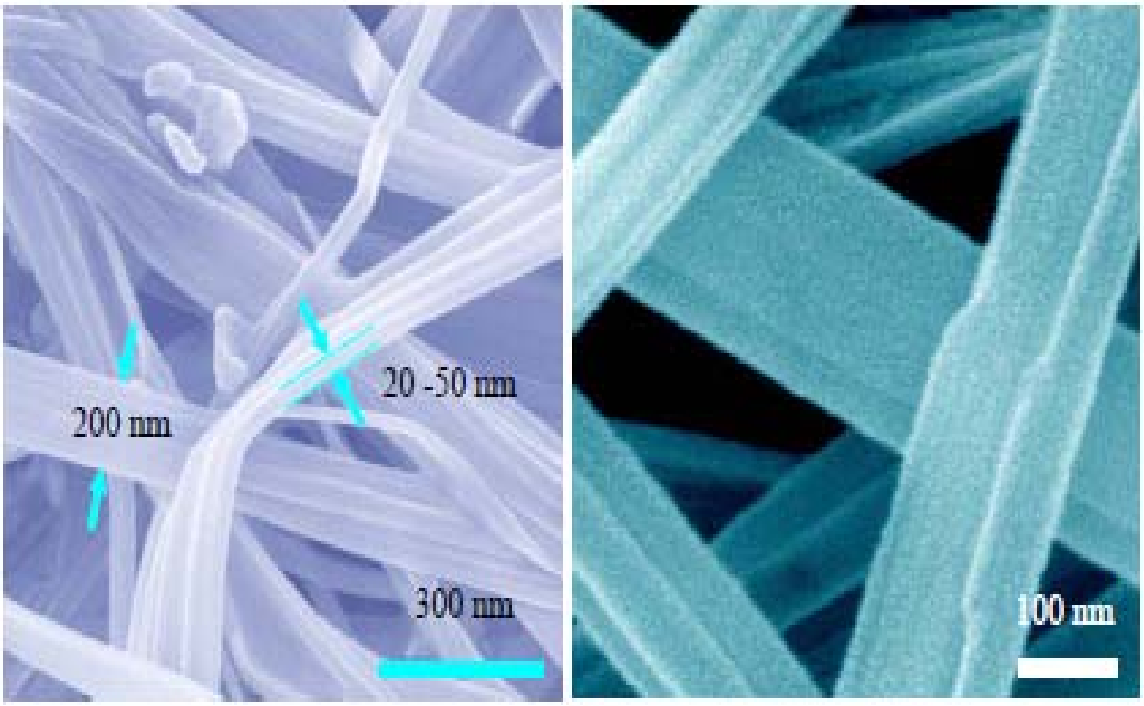

Figure 3-2 Zoomed SEM micrograph of MHSH nanobelts

An EDS analysis of the nanobelts, as seen in Figure 3-3, clearly demonstrated the existence of O, Mg and S, which was in agreement with the XRD analysis as discussed below. A rough atomic ratio estimation of Mg to S from the EDS analysis was 11.13/1.81 ≅ 6.1, very close to the ratio of Mg/S = 6.0 defined in the chemical formula $5Mg(OH)_2.MgSO_4{\cdot}3H_2O$ of MHSH, also in a good agreement with the chemical structure of the proposed MHSH. The extra peaks of C and Cu from the picture were resulted from the holly copper grid which was used to hold the samples for the observation.

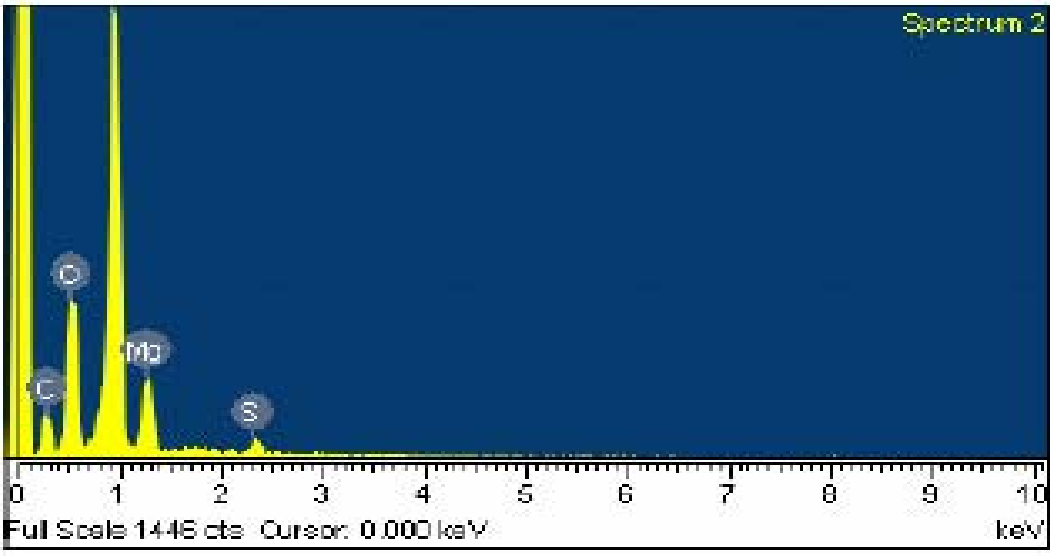

Figure 3-3 EDS spectra of the MHSH nanobelts

3.4.2 XRD structural characterization

The XRD spectrum of the prepared MHSH exhibited a very good match with that as listed in the database. As shown in Figure 3-4, a set of diffraction peaks as numbered from 1 to 10 sequentially in the plot, at 2θ: 12.83, 17.38, 23.11, 29.42, 34.62, 39.41, 43.25, 45.48, 47.61, and 57.42 were recorded as strong peaks, corresponding to *d*-spacings of 6.89, 5.10, 3.84, 3.03, 2.59, 2.28, 2.09, 1.99, 1.91, and 1.60 Å respectively. These data matched very well with those of 2θ (intensity): 12.91 (45), 17.31 (95), 22.78 (60), 29.96 (50), 34.44 (60), 39.47 (6), 43.49 (4), 45.57 (25), 47.70 (4), and 57.21 (12), as listed for MHSH with a formula of $Mg_6(OH)_{10}SO_4{\cdot}3H_2O$ in the database (JCPDS No: 07-0415). In addition to that, other minor peaks with less strengths appeared at 2θ (*d*): 10.96 (8.06), 26.11 (3.41), 30.13 (2.96), 36.38 (2.47),

48.42 (1.88), 51.63 (1.77), 53.68 (1.71), 54.92 (1.67), and 61.26 (1.51), as sequentially marked with asterisks from small to large in the plot, also matched well with that of 2θ (intensity): 11.092 (6), 25.955 (8), 29.960 (50), 36.434 (8), 47.995 (8), 51.594 (10), 53.955 (6), 54.828 (14), 55.114 (40), and 61.164 (18), in the database. The cell parameters for the MHSH nanobelts synthesized were found to be *a*: 15. 94, *b*: 3.11, and *c*: 13.38 Å respectively. All these analyses showed good agreement with data that reported in the literature [155, 158].

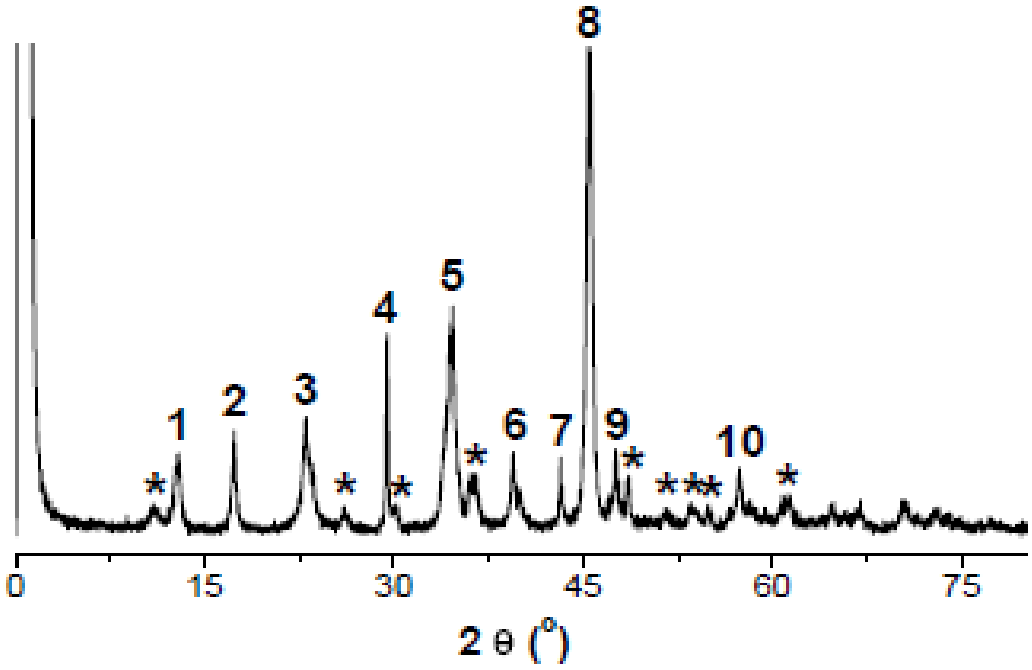

Figure 3-4 XRD spectrum of MHSH nanobelts

3.4.3 TEM characterization

Figure 3-5a shows a typical bright field TEM image of a nanobelt bundle ~500 nm in diameter. The corresponding electron diffraction pattern as shown in Figure 3-5b indicated that the bundle was composed of well-aligned single crystalline nanobelts of a large-unit-cell compound, the orange arrowheads showed the large spacing atomic planes. The strongest set of diffraction spots, however, were matched to those from MgO, which indicated that under an electron beam, $5Mg(OH)_2.MgSO_4.3H_2O$ decomposed to MgO rapidly.

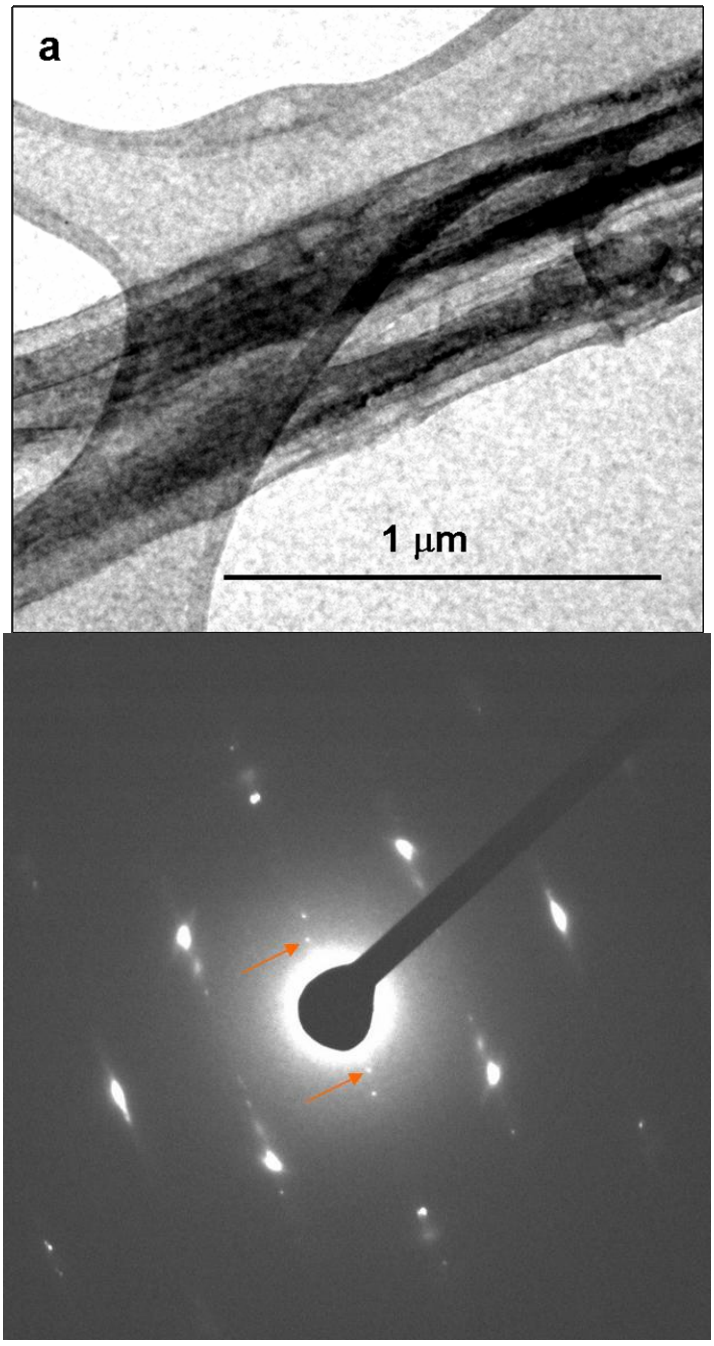

Figure 3-5 a) A typical bright field TEM image of the original 5Mg(OH)2.MgSO4.3H2O nanobelt bundle b) the corresponding electron diffraction pattern of the nanobelt bundle

Decomposition was further confirmed by the thermal behavior of MHSH under high voltage electron beam irradiation. Figure 3-6a shows a TEM image of an MHSH nanobelt after it was exposed to a 100kV electron beam for about 10 minutes. The image showed that the nanobelt possessed a porous structure. Similar phenomena were observed by other researchers[155]. Figure 3-6b shows the corresponding electron diffraction pattern of the MgO nanobelt along the [220] direction.

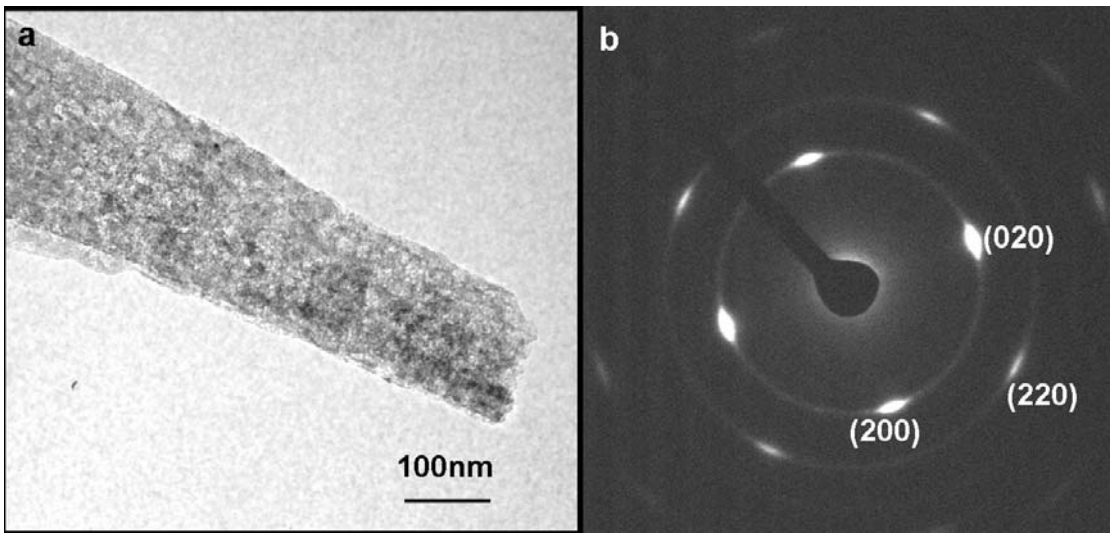

Figure 3-6 a) A typical bright field TEM image of a MgO nanobelt with porous structure after electron beam irradiation. b) the corresponding electron diffraction pattern of MgO along the [220] direction.

3.4.4 Thermal behavior of MHSH nanobelts

The thermal behavior of the MHSH nanobelts was further studied by TGA analysis. As shown in Figure 3-7, the MHSH nanobelts experienced thermal decomposition at relatively low temperature, providing further evidence for decomposition under an electron beam and validating its function as fire retardant agent [156]. From Figure 3-6, three weight loss stages were found: 230-300^{o}C, 360-450^{o}C, and 820-1000^{o}C. From room temperature to 230^{o}C, weight loss was attributed to the evaporation of absorbed water. In the range of 230-300^{o}C, the weight loss of 7.0% was attributed to the loss of 1.5 H_2O by the reaction

$$5Mg(OH)_2 \bullet MgSO_4 \bullet 3H_2O \xrightarrow{-1.5\ H_2O} 5\ Mg(OH)_2 \bullet MgSO_4 \bullet 1.5H_2O \quad (3.1)$$

The theoretical weight loss for the above reaction is 6.55%, which agrees well with the experimental value. However, the weight loss rate for $5Mg(OH)_2 \bullet MgSO_4 \bullet 3H_2O$ nanobelts created in this study was slightly differed from that of the reported results from MHSH needles[154, 155]. This disagreement may be due to the different final product morphologies, which will affect the dehydration temperature of weakly bonded water molecules.

At the second stage of heating in the temperature range of 360-450^{o}C, the MHSH lost its bound water completely and $Mg(OH)_2$ decomposed to MgO. The total

weight loss for the second step was 16.5%, which agrees very well with the theoretical water loss value of 16.4, confirming the completion of the dehydration process:

$$5\ Mg(OH)_2 \bullet MgSO_4 \bullet 5H_2O \xrightarrow{-6.5\ H_2O} MgO + MgSO_4 \qquad (3.2)$$

Finally, the magnesium sulfate decomposed in the temperature range of 820 – 1000^{o}C formed MgO. The weight loss in this decomposition step was 25% of the theoretical calculation and 16% of the experimental results calculation respectively. The lack of agreement between the two values may be due to the incomplete conversion of $MgSO_4$ to MgO.

$$MgSO_4 \xrightarrow{-\ SO_3} MgO \qquad (3.3)$$

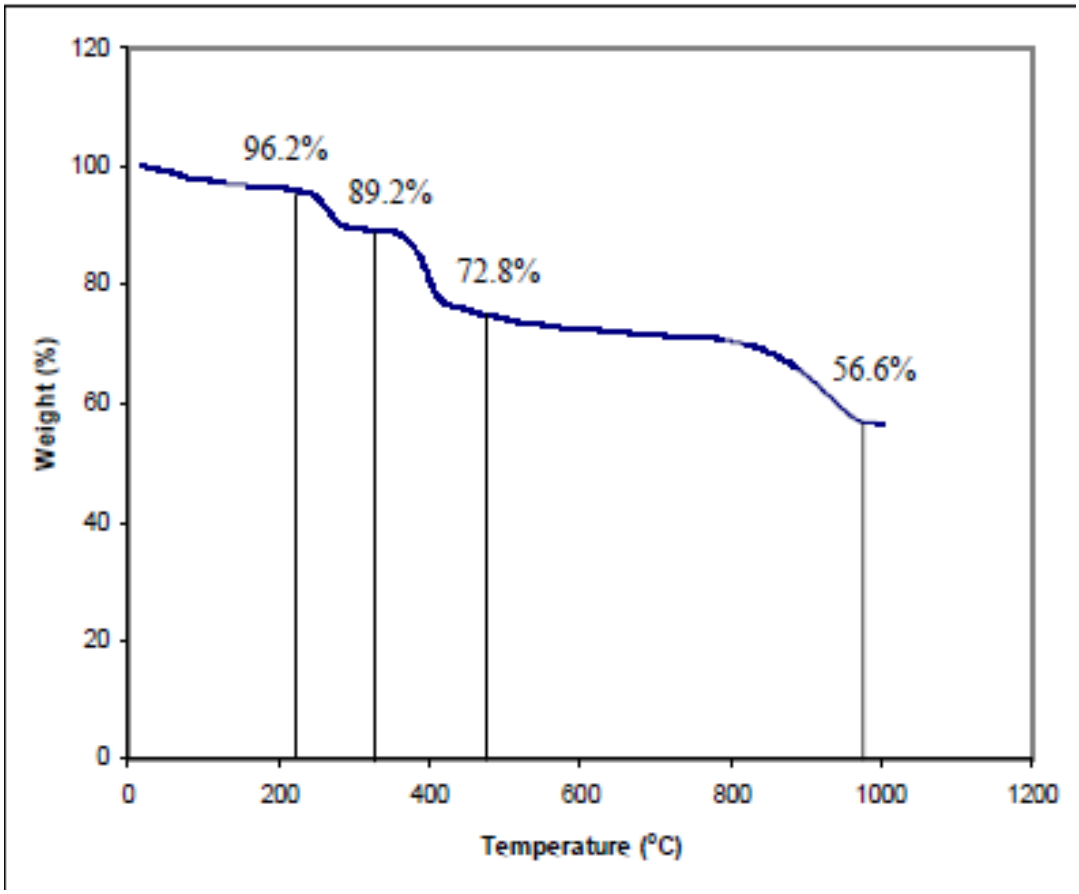

Figure 3-7 Thermal behavior of MHSH nanobelts

The morphologies of the MHSH nanobelts and the MgO nanowires made from dehydration and the decomposition of MHSH at 1000°C are shown in Figure 3-8. Notably, the final MgO products still maintained their nanobelt shape but were shorter and stiffer compared to their original precursors. They also displayed a porous structure. In addition, the MgO nanowire made from MHSH was composed of many small MgO nanocrystals.

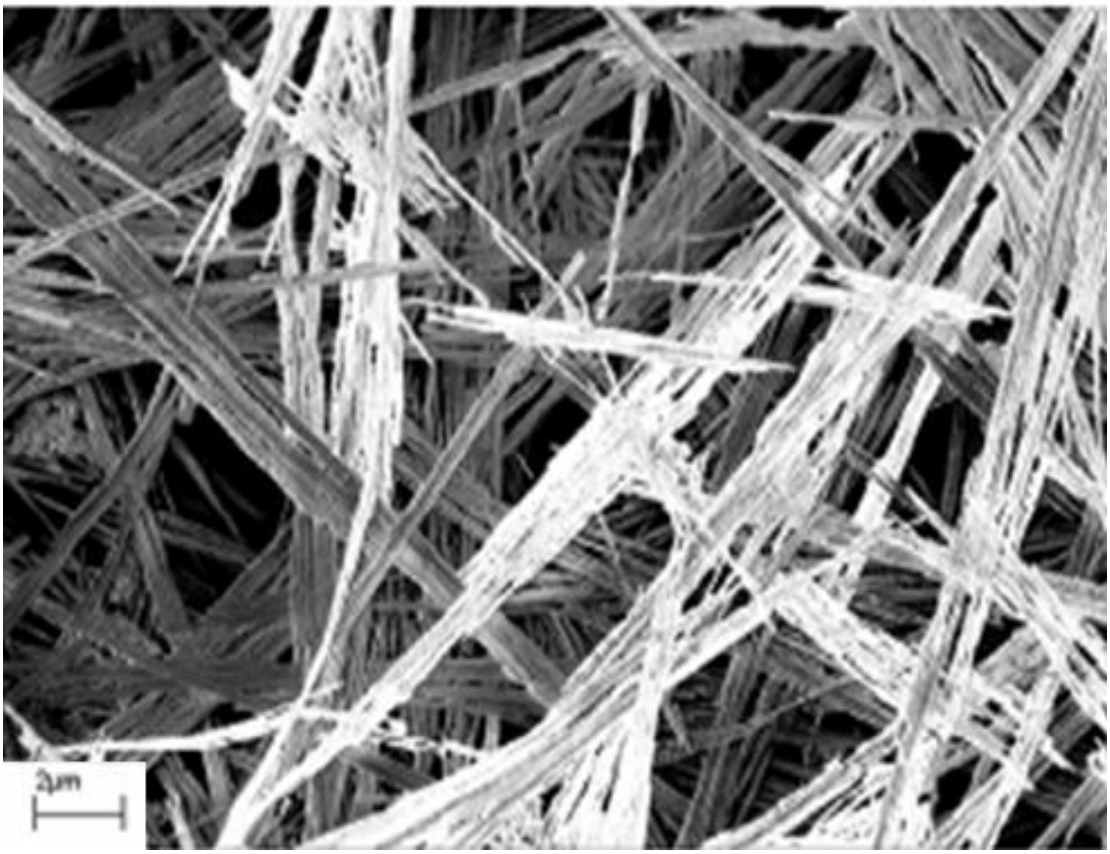

Figure 3-8 SEM micrograph of the calcined MgO nanobelts

3.4.5 Growth mechanism of nanobelts

3.4.5.1 Chemistry of nanobelt growth

MHSH nanobelt formation is simply a chemical reaction of Mg^{2+}, SO_4^{2-} and OH^- ions in water at a controlled temperature and ion concentrations. In precipitation, it is well known that the solubility products (K_{sp}) of the reactants involved in the system determine, to some extent, the sequence of the crystals to be precipitated out in the system. The final precipitation will be that the one with the smallest K_{sp}. In this

reaction system, $MgSO_4$ and $CaCO_3$ can be ionized in water to form hydrolyzed ion species, such as Mg^{2+}, SO_4^{2-}, CO_3^{2-}, HCO_3^- and OH^-, etc. The dissociation and association processes of these species may then result in the formation of bicarbonate and OH^- ions. Furthermore, the reactions between these ion pairs can be reorganized into a range of precipitates such as $Mg(OH)_2$ and $MgCO_3$, depending on the K_{sp} of the pairs to be formed, as shown Table 3-1 [159].

Table 3-1 Solubility constants for different carbonate salts and $Mg(OH)_2$

Materials	K_{sp}
$CaCO_3$	3.36×10^{-9}
$MgCO_3$	6.8×10^{-6}
$BaCO_3$	2.6×10^{-9}
$Mg(OH)_2$	5.6×10^{-12}

During the synthesis of MHSH nanobelts, OH^- is one of the ions participating directly into the formation of the final product, $5Mg(OH)_2 \cdot MgSO_4 \cdot 3H_2O$. Since no direct OH^- ion was introduced to the reaction system, the OH^- ion must have been an intermediate product during the reaction. For the reaction system, a hydrolysis reaction of carbonate ion may take place in water, as shown below:

$$CO_3^{2-} + H_2O = HCO_3^- + OH^- \quad (3.4)$$

$$HCO_3^- = CO_2 \uparrow + OH^- \quad (3.5)$$

And the overall hydrolysis reaction is as follow:

$$CO_3^{2-} + H_2O = CO_2 \uparrow + 2OH^- \quad (3.6)$$

Because of the low solubility of sparingly soluble carbonate salts in aqueous solution, the concentration of OH^- ions in the solution is low, creating a low supersaturation environment for the reaction. The OH^- ions in the solution will react with Mg^{2+} and SO_4^{2-} ions to form a crystal of $5Mg(OH)_2 \cdot MgSO_4 \cdot 3H_2O$, as characterized in the previous study. It should be noted that the final nanobelt products, although they were prepared by using different carbonate salts, have the same EDS and XRD spectra, which strongly suggests that the cations, such as Na^+, Ca^{2+}, and Ba^{2+}, do not directly participate in the chemical reaction of nanobelt formation. Therefore, the overall reaction can be written as follows:

$$MgCO_3 \longrightarrow Mg^{2+} + CO_3^{2-} \quad (3.7)$$

$$CO_3^{2-} + H_2O \longrightarrow HCO_3^- + OH^- \quad (3.8)$$

$$HCO_3^- \longrightarrow CO_2 + OH^- \quad (3.9)$$

$$Mg^{2+} + 2OH^- \longrightarrow Mg(OH)_2 \quad (3.10)$$

$$5Mg(OH)_2 + MgSO_4 + 3\,H_2O \longrightarrow 5Mg(OH)_2 \cdot MgSO_4 \cdot 3H_2O \quad (3.11)$$

When the concentration effect on nanobelt growth was first studied, equimolar amounts of $MgSO_4$ and $CaCO_3$ were used, and the final products were primarily in short whiskers, with trace amounts of nanobelts formed. By changing the molar ratios of $MgSO_4$ to $CaCO_3$ from 1 to 10, the products that were formed were changed to nanobelts. With further increases in the ratio of $MgSO_4$ to $CaCO_3$, the proportion of nanobelts in the product decreased.

3.4.5.2 Effect of temperature on nanobelt growth

The study observed a significant effect of temperature on the growth of nanobelts. For example, when sparingly soluble carbonate salts were mixed with $MgSO_4$ in a solution at temperatures from 25 to 95^{o}C, no nanobelts were observed even after a few days of reaction. When the reaction temperature was raised to about 100^{o}C, nanobelts were observed after 6 hours. The nanobelts grew even faster after further increasing the temperature to 110^{o}C. The morphology of the nanobelts was also affected by the reaction temperature. The nanobelts obtained at 100 ^{o}C were very long with a higher aspect ratio. However, when higher temperatures were used, the final products tended to be shorter in length and larger in diameter, resulting in lower aspect ratio nanoparticles. The study also tested the hydrothermal method at a temperature higher than 140 ^{o}C using an autoclave. However, no nanobelts were observed after 6 hours. Other studies reported that a few whiskers rather than nanobelts could form at a temperature of 220^{o}C [154], but the reactants used these

system were different from those in this system. The reason why MHSH nanobelts could not be prepared using an autoclave at high temperatures will be discussed in the following section.

3.4.5.3 Influence of different carbonate salts

The influence of various carbonate sources besides $CaCO_3$, such as, Na_2CO_3, $MgCO_3$, and $BaCO_3$ etc., on the formation of the nanobelts was studied, and it was found that all of them were effective in controlling the formation of nanobelts if all the reaction conditions remained same as in the systems described above. However, some differences were observed during the reaction process and in the final products. Figure 3-9 shows SEM micrographs of the intermediate products obtained by using different sparingly soluble carbonates. The reaction rate was qualitatively indicated by the amount and the length of the nanobelts. For example, by comparing the images in Figure 3-8, it was found that after a 12-hour reaction, the system with $BaCO_3$ could produce only short whiskers with some large unreacting $BaCO_3$ particles remaining in the reaction system. In contrast, the reaction with $MgCO_3$ produced more and longer nanobelts after the same reaction period. The nanobelt formation rate using different carbonate salts shows a close relationship with the solubility product constant in water. Table 3-1 shows the solubility products for materials involved in the reactions. Because $MgCO_3$ has a higher solubility product

constant than either $CaCO_3$ or $BaCO_3$, the formation of MHSH nanobelt was faster for $MgCO_3$ than for other sparingly soluble salts.

When NaOH was directly added to the $MgSO_4$ solution as the OH^- source, irregular $Mg(OH)_2$ particles were formed immediately, and no nanobelt was observed because NaOH is fully soluble in water, resulting in a high supersaturation condition. In contrast, due to their slow hydrolysis in water, sparingly soluble salts, such as $CaCO_3$, $MgCO_3$, and $BaCO_3$, provide OH^- slowly , creating a low supersaturation environment that favors 1-D particle growth [160]. For the same reason, carbonate salts, providing constant OH^- for the reaction, can act as a buffer. When NaOH was directly added to the solution, the OH^- was depleted very quickly and could not be maintained at a constant level.

Compared with the direct addition of NaOH to the reaction system, the supersaturation condition was much lower if sparingly soluble carbonate salts were used as the OH^- resource. Therefore, they sparingly soluble carbonate salts functioned as both reactant and supersaturation control agents. As shown in Equation (2.5), the byproduct of CO_2 must be removed from the reactor so that the sparingly soluble carbonates can continually provide OH^- for MHSH growth. Thus, compressed air must be bubbled continually through the reaction system to purge the CO_2.

In order to further examine the importance of removing CO_2, this study conducted a reaction system consisting of 0.1 mol $MgSO_4$, 0.01 mol $MgCO_3$, and 250 ml DI water in an autoclave at a temperature of 115 ^oC for 48 hours. Because the autoclave was sealed, the byproduct (CO_2) could not be removed from the system. Therefore, while the reaction system reached equilibrium quickly, the reaction could not continue. By contrast, when a pressurized cooker (T~115 ^oC) was used instead of an autoclave, the MHSH nanobelts underwent fast growth. The difference between the reactions using an autoclave and the pressurized cooker was that the byproduct of CO_2 could be released from the pressurized cooker when the pressure was high, but it could not be released from the autoclave, which was sealed. As a result, the reaction in a pressurized cooker would not reach equilibrium, and the reaction of the system could continue. Therefore, the removal of the CO_2 byproduct is important for 1D MHSH growth.

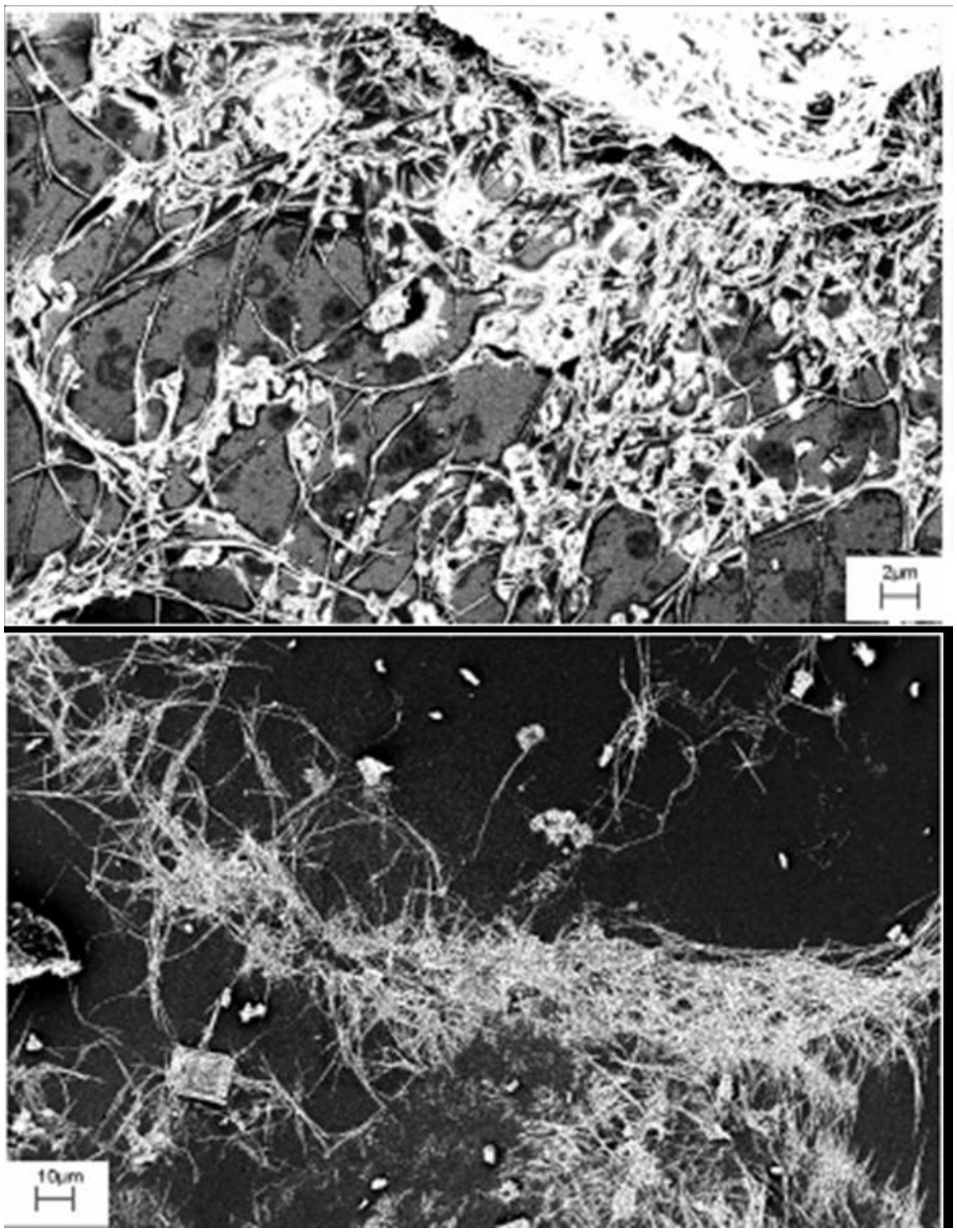

Figure 3-9 SEM images of Intermediate products after 12 hour reaction from $BaCO_3$ (A) and $MgCO_3$ (B)

3.5 Conclusion

The study demonstrated the formation of MHSH nanobelts via a soft chemistry approach using sparingly soluble carbonate salts and magnesium sulfate as reactants and found that the product was composed of $5Mg(OH)_2 \cdot MgSO_4 \cdot 3H_2O$ based on EDS and XRD analysis. SEM and TEM observations revealed that the nanobelts that were formed were up to one hundred micrometers long, with a thin belt structure and rectangular cross section profile. The MHSH, which in a single-crystal form, was easily subjected to decomposition under electron beam irradiation during the electron microscope observation to form MgO, a very important candidate for superconductor fabrication due to its chemical inertness and its compatible with superconductor materials [96, 161] and a brand new class of nano filler materials in polymer composite engineering with an extra long aspect ratio. The nanobelts dehydrated near 230°C, decomposed at a higher temperature, and were eventually converted into MgO at about 1000°C. The MgO obtained from calcination still displayed a nanobelt shape, but the belt was much shorter and weaker than its precursor.

The slow hydrolysis of carbonate ions provided OH^- ion for $Mg(OH)_2$ nucleation and the driving force for MHSH nanobelt growth. Different salts produced similar nanobelts but the reaction rate depended on the solubility constant of the sparingly soluble salts used. The higher the solubility constant was, the faster the

reaction rate and longer aspect ratio were. Among the carbonate salts used in this study, the $MgCO_3$ system showed the fastest reaction rate. The reaction temperature had a significant effect on the formation rate the morphology of nanobelts. A temperature higher than the boiling point of the solution and lower than 140^{o}C resulted in short and stiff nanobelts. However, if the temperature was lower than the boiling temperature, the nanobelts could not form .

Chapter 4 : Synthesis of Zinc Oxide Nanorods Using Carbonate Salts as Supersaturation Control Agents

In the last chapter, we demonstrated the importance of the supersaturation effect in the growth of 1D nanostructures. With all the other experimental conditions remained the same, low supersaturation enhances the growth of MHSH nanobelts, while high supersaturation leads to irregular particles. The supersaturation level in the solution can be controlled using sparingly soluble carbonate salts. This approach can be further extended to the synthesis of other 1D nanomaterials. In this chapter, we will use a similar approach to synthesizing 1D ZnO nanomaterials. ZnO is a material with both commercial and scientific importance. Large-scale synthesis of ZnO nanostructures will significantly contribute to the development of research and its applications. Similar to previous experiment, we will use sparingly soluble carbonate salt, calcium carbonate, as a supersaturation control agent. The slow hydrolysis of $CaCO_3$ at elevated temperatures provides a buffer for OH^-, whose concentration should be finely controlled for solution synthesis of 1D ZnO nanostructure. The growth process is monitored through various methods, namely, XRD characterization of the intermediate product, SEM observation of morphology evolution, and head space gas chromatography (GC) examination of residue carbonate ions. By using several successful examples of synthesizing 1D nanomaterials, we will be in a position to extend the same supersaturation control concept to many other nanomaterial syntheses.

4.1 Introduction

Zinc oxide (ZnO) is an industrially and scientifically important material. It has been widely used in paints, rubber processing, and medicine, and as a catalyst in methanol production. In addition to these traditional applications such as pigment in painting and coating, as a wide band gap semiconductor, ZnO has recently attracted wide attention in the field of electronics and optoelectronics. The literature provides a number of in-depth studies of the mechanical, chemical, electrical, and optical properties of ZnO in addition to related technological issues such as growth, defects, p-type doping, band-gap engineering, devices, and nanostructures can be found in the literature [162, 163].

ZnO, a semiconductive material with a wide band gap (3.37ev) and a big excitation binding energy (60mev). has been recognized as a promising material in electronics, optoelectronics, and solar cell technology. Various applications of these unique nanostructured ZnO, particularly for 1D nanostructured ZnO, have been reported [164-167]. ZnO can ensure efficient exciton emission at room temperature under low excitation energy. Hence, ZnO is recognized as a promising photonic material in the blue–UV region. Strong emissions at a ~380nm wavelength for different sizes of ZnO nanowires have been reported [55]. Green emission at ~520nm has also been observed when the diameter of the nanowires decreases. Room temperature photoluminescence spectra of ZnO showed a strong relationship with the

diameters of the nanorods. While the UV emissions (~380nm) can be attributed to near band-edge emissions, it has been suggested that the green emissions correspond to the singly ionized oxygen vacancy in ZnO. The thinner the nanowires were, the stronger the green emissions were, suggesting a higher oxygen vacancy in the nanowires. However, the size effects of these emissions were the result of a high surface-to-volume ratio rather than quantum confinement [168].

Nanoscale ZnO materials have been effectively used as gas sensors for a variety of gases such as ethanol, oxygen, and ammonium. For example, it was found that high sensitivity and the fast response time of ethanol vapor were achieved at a working temperature of 300°C for ZnO nanowires fabricated with MEMS technology [169]. It was reported that the sensitivity of the sensor depended on the diameter of the nanowires [170]. It is believed that the high surface-to-volume ratio of nanosize materials is more advantageous to sensor applications than that of microstructure materials.

Recently, nanostructured ZnO has shown promising applications in nanodevices. It is reported nanoscale mechanical energy can be converted into electrical energy by means of piezoelectric zinc oxide nanowire arrays [171]. The aligned nanowires were deflected with a conductive atomic force microscope tip. The coupling of the piezoelectric and semiconducting properties of zinc oxide creates a strain field and charge separation across the NW as a result of its bending. The

rectifying characteristic of the Schottky barrier formed between the metal tip and the NW leads to the generation of electrical current. This approach has the potential of converting mechanical, vibrational, and hydraulic energy into electricity to power nanodevices.

In an effort to fully explore the application of ZnO nanomaterials, researchers have synthesized various nanostructures, such as nanowires [172], nanobelts [173], nanorods [174], and nanorings [175], using different methods. These methods include either chemical or physical vapor deposition (CVD) at high temperature (500-600^{o}C) or a wet chemical approach at low temperatures. For example, with high temperature synthesis, ZnO nanobelts were synthesized at temperatures of 500-600^{o}C in a furnace while the source material ZnO power was heated to a temperature of 900-1300^{o}C [173]. The typical CVD process in Section 1.3.1 is applicable to ZnO synthesis. Source Zn or ZnO and a catalyst are placed inside a ceramic boat that is then loaded into the central region of a ceramic tube. Downstream in the tube, several pieces of substrate are placed on which products of ZnO will grow. The CVD synthesis method has been systemically investigated. Process parameters, including the temperature inside the furnace, the pressure, the carrier gas species and flow rate, the substrate used, the distance between the source material and substrate, and the reaction time, have been found to affect the growth of ZnO morphologies [86]. A qualitatively diagram of supersaturation is shown in Figure 4-1. In different downstream regions, both the supersaturation and the morphologies of the final product differ. Regions I, II,

III, and IV in the figure correspond to microrods, nanoplatelets, nanobelts, and nanowires, respectively, with a low flow rate of carrier gas [86]. The supersaturation can be well controlled close to unity during these reactions. Under this condition, the growth of crystal is under thermal equilibrium and the morphology of the final product is defined by its internal crystal structure and well described by the Wulff theorem [176]

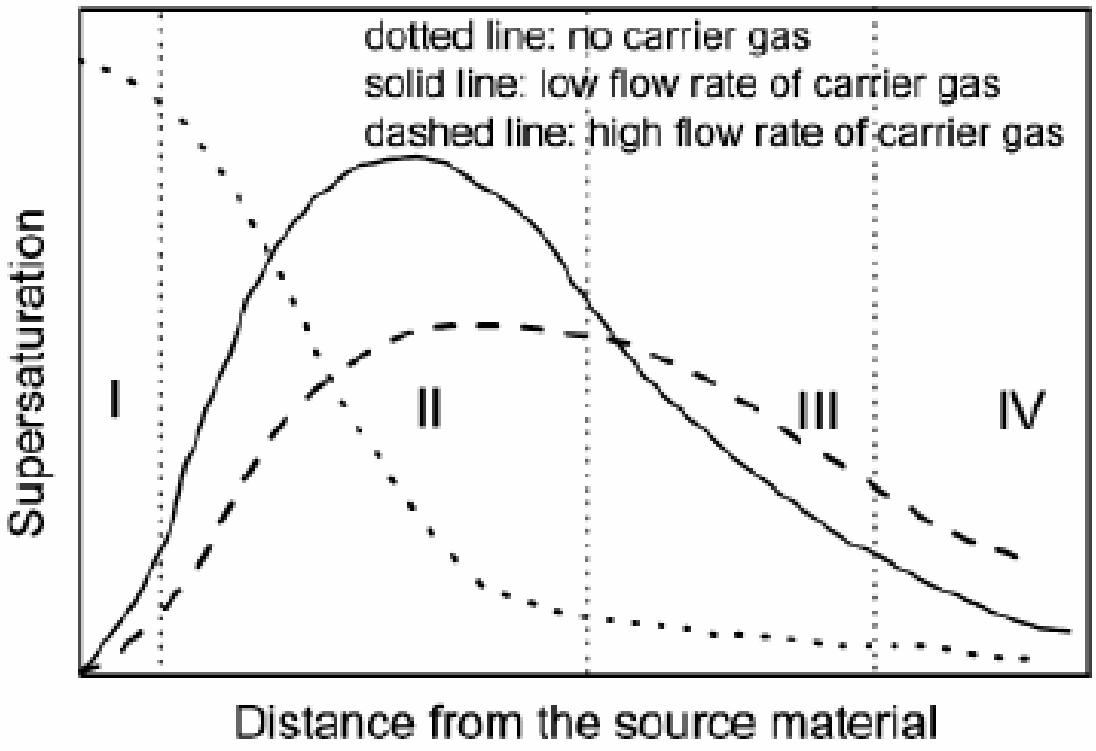

Figure 4-1 Supersaturation level inside the tube in CVD synthesis

The division of the tube into four regions is merely a demonstration of essence of the supersaturation. In practice, however, within the same control window, products with different morphologies will be produced, as shown in Figure 4-2. Nanowires and nanosheets can both be synthesized from the same supersaturation level. In order to obtain pure nanostructures, other controlling parameters need to be considered.

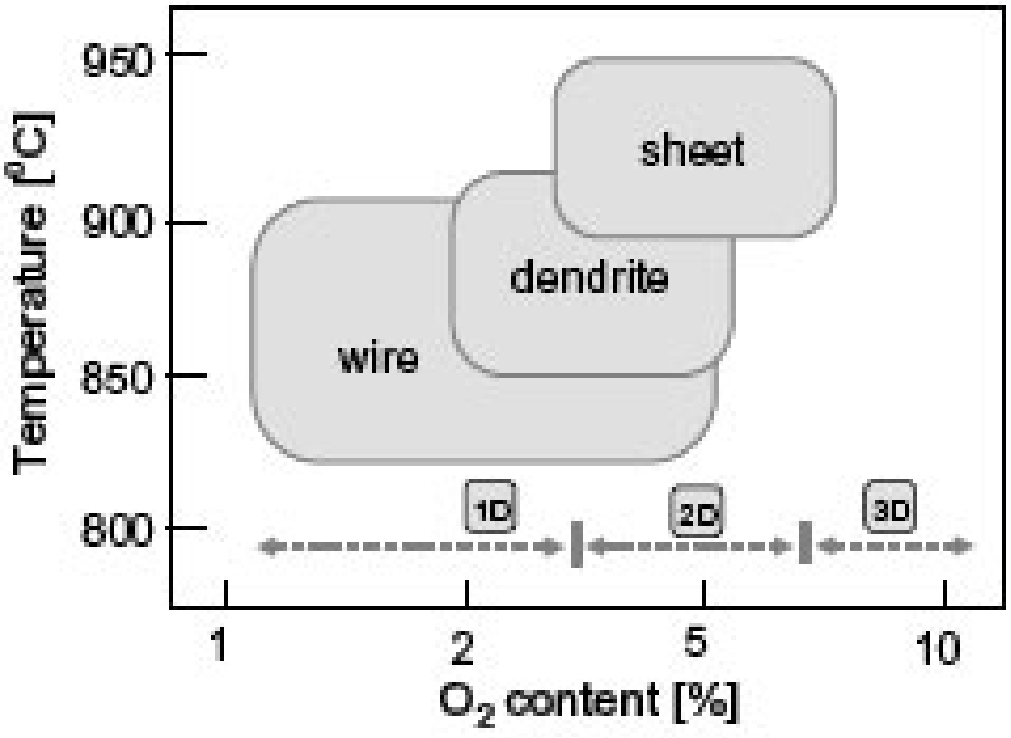

Figure 4-2 Relationship between process parameters and corresponding nanostructures[177]

Another important method for synthesizing ZnO nanostructures is solution synthesis. Some of its benefits that it is low temperature, catalyst free, and potentially large scale. Vayssieres reported a method for synthesizing ZnO nanorods arrays on certain substrates[178, 179]. This simple method is now widely used for synthesizing ZnO nanostructures in solution. Soluble zinc salts such as $Zn(NO_3)_2$, $Zn(Ac)_2$, and $ZnCl_2$, are mixed with hexamethylenetetramine (HMT) and a target substrate is put on top of the solution if the nanorods need to be grown on a substrate. The mixture is then either sealed in an autoclave so that it can react at high temperatures or maintained in an open system sot that it can react at low temperatures. After several hours' reaction, the 1D nanorods will grow on the substrate. The mechanism is believed to relate to interfacial tension. However, it was found that the substrates had no effect on the growth of the nanorods [178-180], which seems contradictory to the proposed mechanism. Other researchers found that ZnO thin film synthesized with the radio frequency sputtering method was dependent on the substrate [181]. Several of alkalines such as NH_3 [182, 183] and NaOH [184-186] were also tested for synthesis, but these methods mainly involved direct precipitation and phase transformation. Under these conditions, supersaturation is very difficult to control.

This section discusses a new synthesis route of ZnO nanorods, an extension of the approach used in previous chapter to demonstrate that supersaturation should be controlled at a low level for 1D nanomaterial growth and can be controlled using sparingly soluble carbonate salts. The reaction was carried out at ambient pressure

with mild reaction temperatures (~100 °C) similar to those of previous MHSH nanobelt syntheses. The morphology and structure of the nanorods were then characterized. The ZnO nanorod growth process was studied using SEM and XRD. The influence of reaction parameters on the formation of nanorods , such as molar ratio of reagents and the temperature of reaction, was also examined.

4.2 Synthesis of ZnO Nanorods

***Materials*:** Zinc sulfate heptahydrate, $ZnSO_4 \cdot 7H_2O$ (98%) and $CaCO_3$ (>99%) were purchased from Aldrich and used without further treatment. All other reagents are from Sigma-Aldrich and used as received. The deionized (DI) water was in mili-Q grade with a conductivity of 18 $m\Omega\ S^{-1}$.

Synthesis: The reaction conditions were similar to those of the MHSH synthesis. Typically, 0.92 g (about 0.04 mol) of zinc sulfate heptahydrate $ZnSO_4 \cdot 7H_2O$, 0.4 g of sodium carbonate $CaCO_3$ (0.004 mol), and 250 ml DI water were added to a 250 ml three-neck round-bottom flask. An air-inlet bubbling tube was inserted to the flask and a refluxing column was added to it as a cooler. The solution in the flask was then heated to its boiling temperature (~100°C) while maintaining gentle agitation with a magnetic stirrer. Compressed air at a pressure of 0.5 psi was

charged at a speed of 20 l/hr and bubbled through the inlet tubing in the mother liquor. The reaction was maintained for 48 hours.

Characterization: The morphology of the nanorods formed was tracked by SEM observation during various stages of the reaction. The XRD spectra of the intermediate products and final products were collected. When the reaction was complete, the suspension was filtered and washed extensively with DI water to remove water soluble impurities. The final product was dried in a vacuum oven at 60 °C overnight and a white powder was obtained.

4.3 Results and Discussion

4.3.1 Characterization

The final products were studied with SEM and the morphology of nanorods was observed, as shown in Figure 4-3. The nanorods were about 5-10μm long and exhibited a hexagonal cross area. Each side of the hexagonal cross area was about 200-300 nm long. The surfaces of the nanorods were not smooth but contained many macroscopic defects such as stages and cavities, as shown in Figure 4-4.

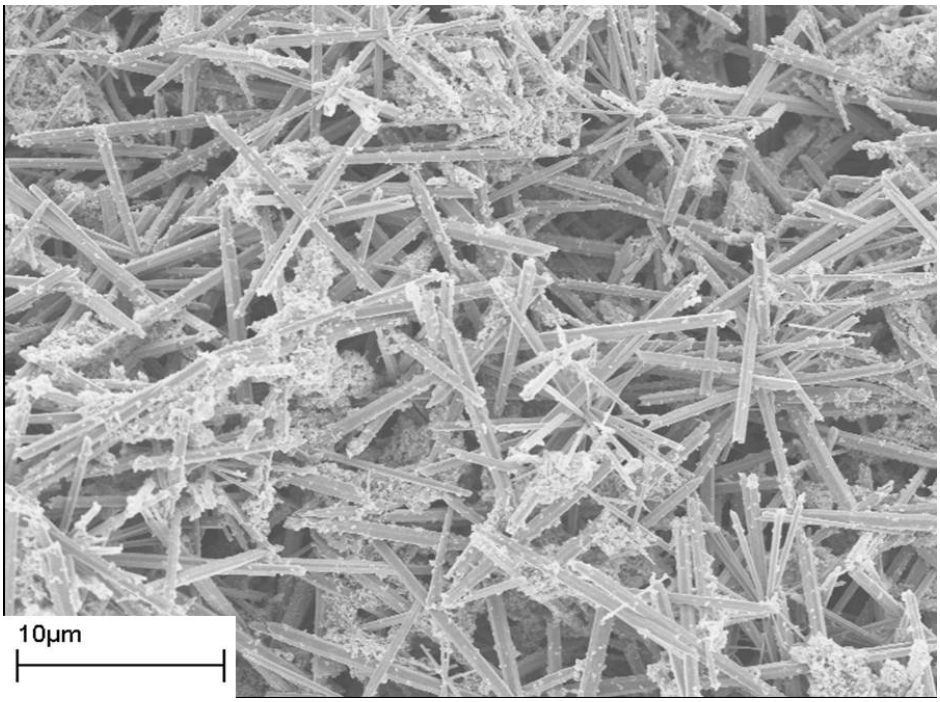

Figure 4-3 SEM of the nanorods

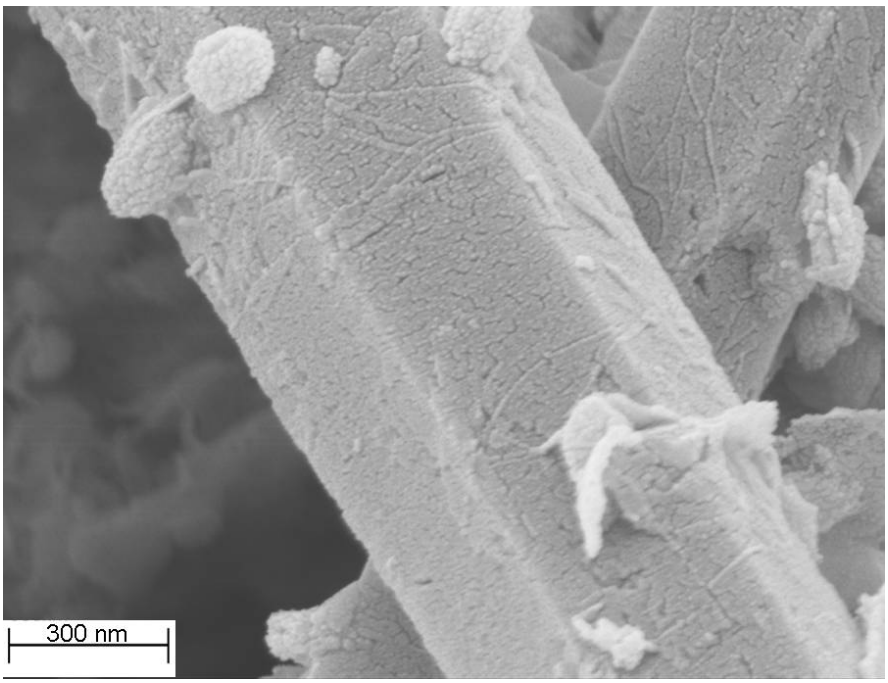

Figure 4-4 Zoomed SEM micrograph of the ZnO nanorods showing a non-smooth surface

The XRD spectra of the nanorods were collected. Figure 4-5 shows the XRD pattern of the ZnO nanorods after 7.5-hour reaction. The spectrum exhibits very sharp diffraction peaks, suggesting high crystallinity of the products. The three strongest peaks at 2θ= 31.93, 34.60, and 36.43 can be attributed to diffraction from (100), (002), and (101) of the ZnO crystal, respectively. These characteristic peaks correspond well to those in the database (JCPDS No. 34-1451) and clearly show that the final products are crystalline ZnO. In addition, several other minor peaks with less strengths, which appeared at 2θ= 23.177, 29.525, and 36.076, were found to be the diffraction from the unreacted calcite $CaCO_3$. The corresponding diffraction faces were (012), (104), and (110), respectively.

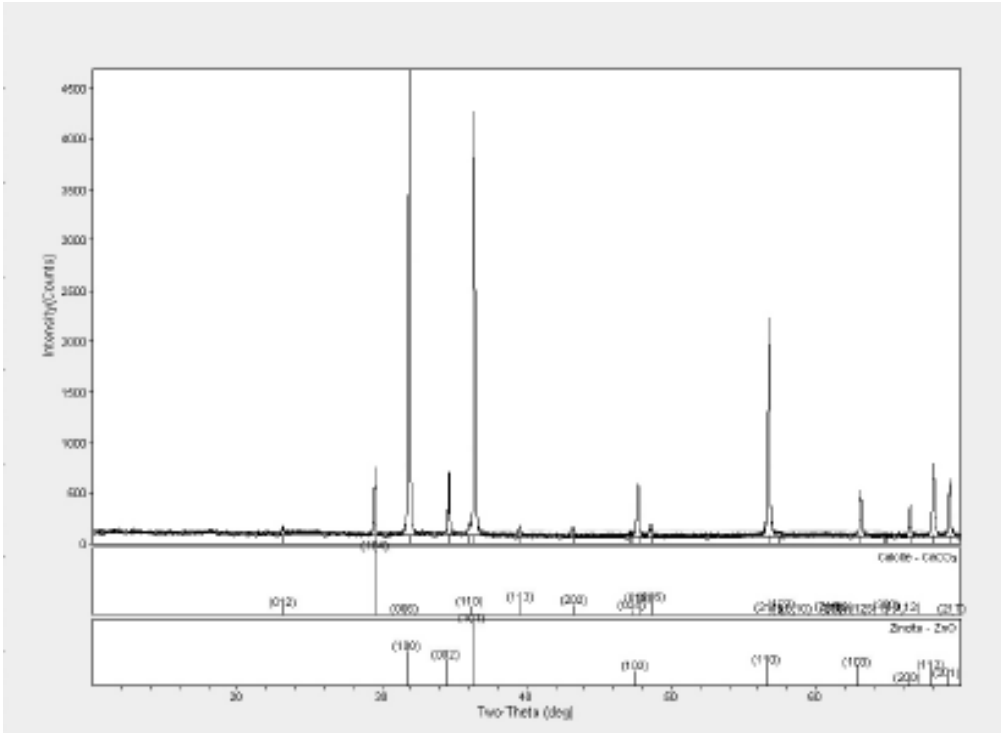

Figure 4-5 XRD spectrum of ZnO after 7.5- hour reaction

4.3.2 Effect of experimental conditions on the synthesis of nanorods

4.3.2.1 Effect of temperature

The effect of temperature on the reaction was investigated. Temperatures of 70, 80, and 90^{o}C were tested with the other conditions remaining the same. Under these temperature conditions, while no nanorods formed during the reactions, nanosheets did. The formation of the nanosheets and its role in the growth of ZnO nanorods will be discussed in detail in a later part of this thesis.

4.3.2.2 Effect of concentration

The effect of chemical concentration on the formation of nanorods was also studied. Maintaining the same amount of calcium carbonate, different ratios of zinc sulfate to calcium carbonate 5:1, 2:1, and 1:1 were tested. A decrease in the ratio produce no nanorod and only irregular particles. When the ratio was set as 10:1 and the amounts of chemicals increased, the final products exhibited hexagonal plate shape, as shown in Figure 4-6.

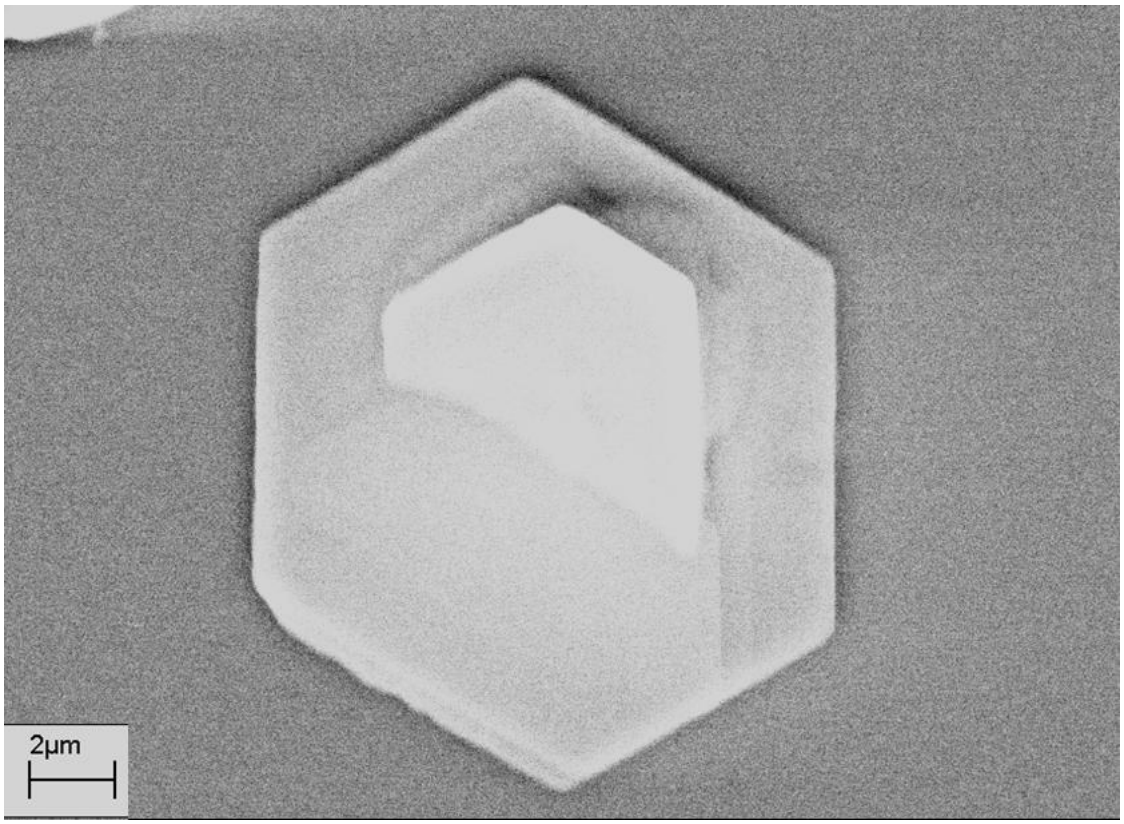

Figure 4-6 Hexagonal plates from high concentration

4.3.2.3 Effect of mixing

The study of the growth kinetics of ZnO nanorods requires pure ZnO nanorods. Previous XRD and SEM characterization showed that the nanorods from the reaction system were mixed with calcium carbonate that did not reacted and intermediate reactants could not be separated easily. To obtain pure nanorods, the reaction was carried out under slightly different conditions.

The same amount of calcium carbonate was put into a dialysis tube suspended in the middle of the zinc sulfate solution. The molecular weight cut off for the dialysis tube can be used to diffuse 12000 to 14000 and the pore size of the tub is less than 5nm. Small ions such as Ca^{2+}, Zn^{2+}, CO_3^{2-} and OH^- could diffuse freely from one side to the other side of the dialysis tube. The dialysis tube could be used in temperature of for 80 ^oC to 120 ^oC. The reaction setup is schematically shown in Figure 4-7.

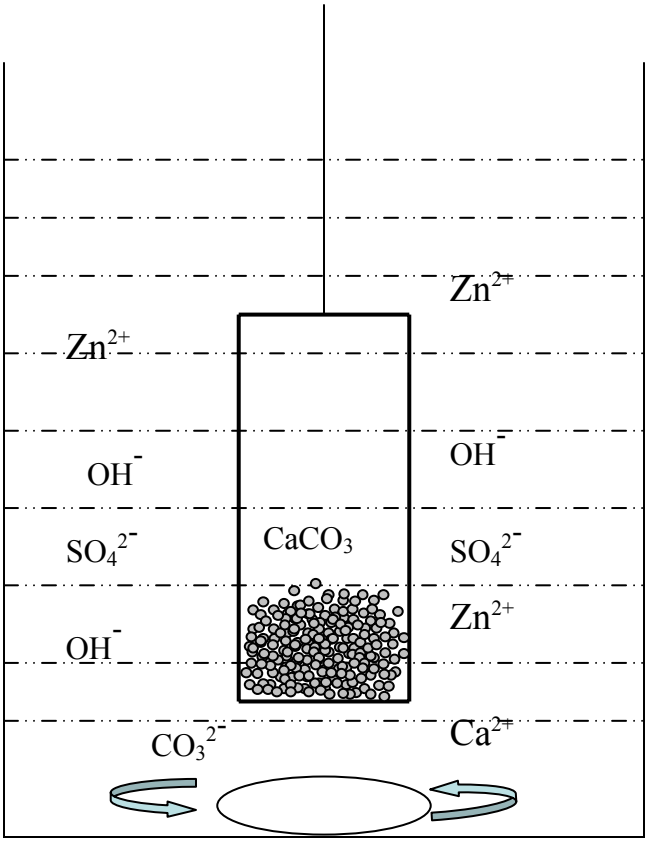

Figure 4-7 Schematics of the reaction with calcium carbonate in the dialysis tube

After eight-hour reaction, however, neither the dialysis tube nor the solution contained nanorods. One possible explanation for this is proposed: Although the ions such as Ca^{2+}, Zn^{2+}, CO_3^{2-} and OH^- can diffuse freely through the membrane, calcium carbonate particles inside the tube cannot be stirred. Calcium carbonate acts as a nucleation site for zinc complex formation. When calcium carbonate is not stirred, only a very small part of the calcium carbonate makes contact with the Zn^{2+} ions. The OH^- provided from dissolved calcium carbonate can not precipitate the Zn^{2+} ions. Which produces no nanorods. In the previous experiments without a dialysis tube, when calcium carbonate was mixed completely within the solution, calcium carbonate was able to mix thoroughly with Zn^{2+} in the solution, and the OH^- ions could make contact with the Zn^{2+}, resulting in the production of ZnO. This experiment suggested that supersaturation is not the only reason to control nanorod growth.

4.3.3 Mechanism of ZnO nanorod growth

It is well known that zinc salts can form a hydration complex in aqueous solution [187, 188], and the hydration ions can further decompose to zinc oxide. Following the discussion in Chapter 3, calcium carbonate, with very low solubility ($Ksp=3.36x10^{-9}$), can release carbonate ions (CO_3^{2-}) at a low concentration. The CO_3^{2-} then hydrolyzes to provide OH^- ions. Zn^{2+} ions and OH^- ions can form $Zn(OH)_2$,

which can decompose to ZnO. In general, the chemistry of the reaction can be written as follows:

$$CO_3^{2-} + H_2O = HCO_3^- + OH^- \quad (4.1)$$

$$HCO_3^- = CO_2 \uparrow + OH^- \quad (4.2)$$

$$Zn^{2+} + 2OH^- = Zn(OH)_2 \quad (4.3)$$

$$Zn(OH)_2 = ZnO + H_2O \quad (4.4)$$

In order to understand the mechanism of ZnO nanorod growth, the growth process of ZnO nanorods was monitored through SEM observations of intermediate products. Based on the result of these observations, the growth process can be roughly divided into three steps: the formation of nanosheets, the formation of seeds, and the growth of nanorods.

In the first stage, from the beginning of the experiment to about 1 hour into the reaction, nanosheets were formed, as shown in Figure 4-8. The nanosheets had irregular shapes about 10nm thick. The surfaces of the sheet were not smooth but instead consisted of small particles. As the reaction proceeded, some seeds, in the shape of egg, were formed at the surface of the nanosheets. The seeds seemed to be empty, as indicated in Figure 4-9. From the SEM graph, the size of the seeds was estimated to be about 100 to 200 nm in diameter. In the second stage of growth, seeds were formed due to the deformation and fractures of the nanosheets.

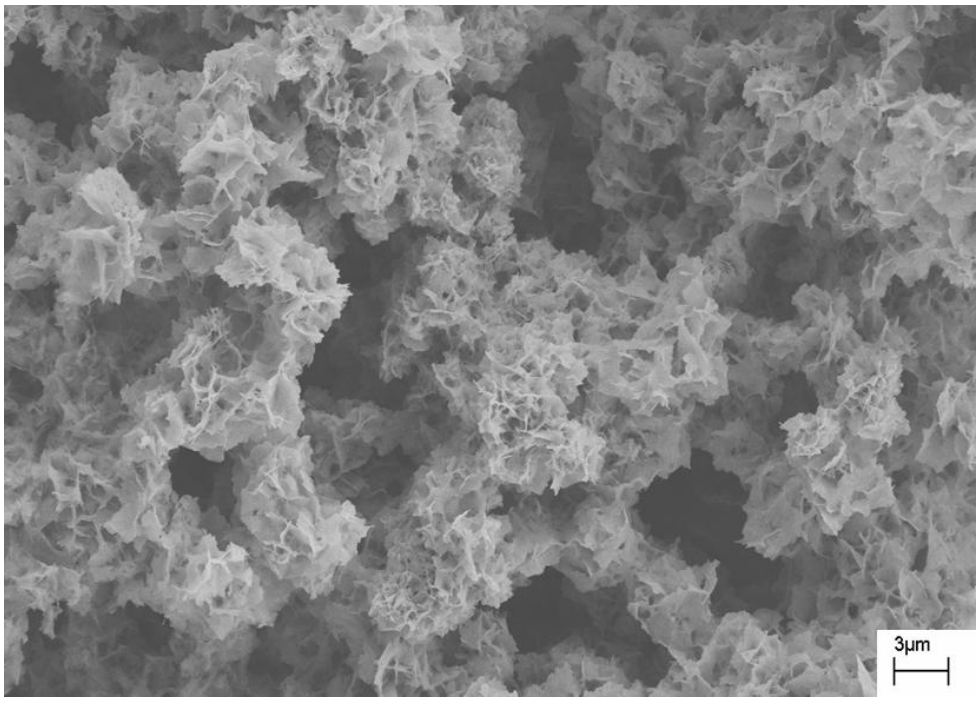

Figure 4-8 SEM of reactant after about 1 hour

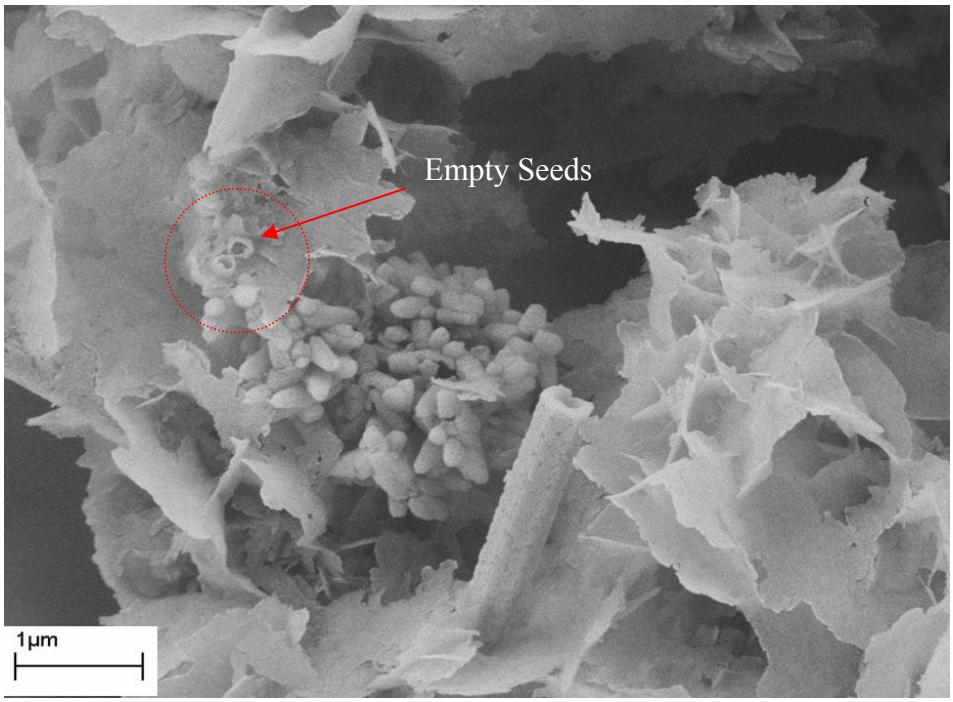

Figure 4-9 Seeds for nanorod growth in the second stage

In the third stage, after the seeds were formed, the nanorods began to form their final shapes through a process similar to Oswald ripening. The seeds were relatively large and the broken pieces from the sheets consisting of small particles could be dissolved or adsorbed on the surfaces of the seeds and finally incorporated into the lattice of the ZnO nanorods. This adsorption also explained the formation of nanotubes during the earlier stages. When the empty seeds were formed, their outside surfaces served as sites for the adsorption. The diffusion of smaller particles to the outside surface was faster than that of the dissolved ions into the tubes and the seeds grew into a nanotube shapes. The nanotubes were finally filled through the diffusion of dissolved ions when there were no small broken pieces.

The intermediate materials of the growth process were investigated by XRD. A series of reactions were prepared and stopped at various reaction times, namely 1 hour, 2.5 hours, 4.5 hours, 6.5 hours, and 7.5 hours. The products that formed during the different reaction times were washed with DI water and dried. The XRD spectra were shown in Figure 4-10. The XRD spectrum confirmed the first formation of an intermediate complex, identified as $Zn_5(OH)_6(CO_3)_2$ (JCPDS No. 98-000-0062), indicated by the peaks at 2θ =12.90, 32.90, and 36.20. Very strong diffraction from the calcium carbonate that had not reacted in the first several hours also appear in the spectrum. The diffractions from ZnO, indicated by diffractions at 2θ= 31.93, 34.60, and 36.43, were negligible for the products until 2.5 hours. As the reaction proceeded, the diffraction intensities from ZnO increased and the diffractions from the

intermediate product decreased. Both the XRD spectrum and experiment observation revealed that after 24 hours some calcium carbonate particles had still not reacted. In other words, despite the longer reaction time (> 48 hours), the calcium carbonate could not be completely consumed. However, the longer reaction caused damaged to the nanorod morphology, resulting in a corn morphology, as shown in Figure 4-11.

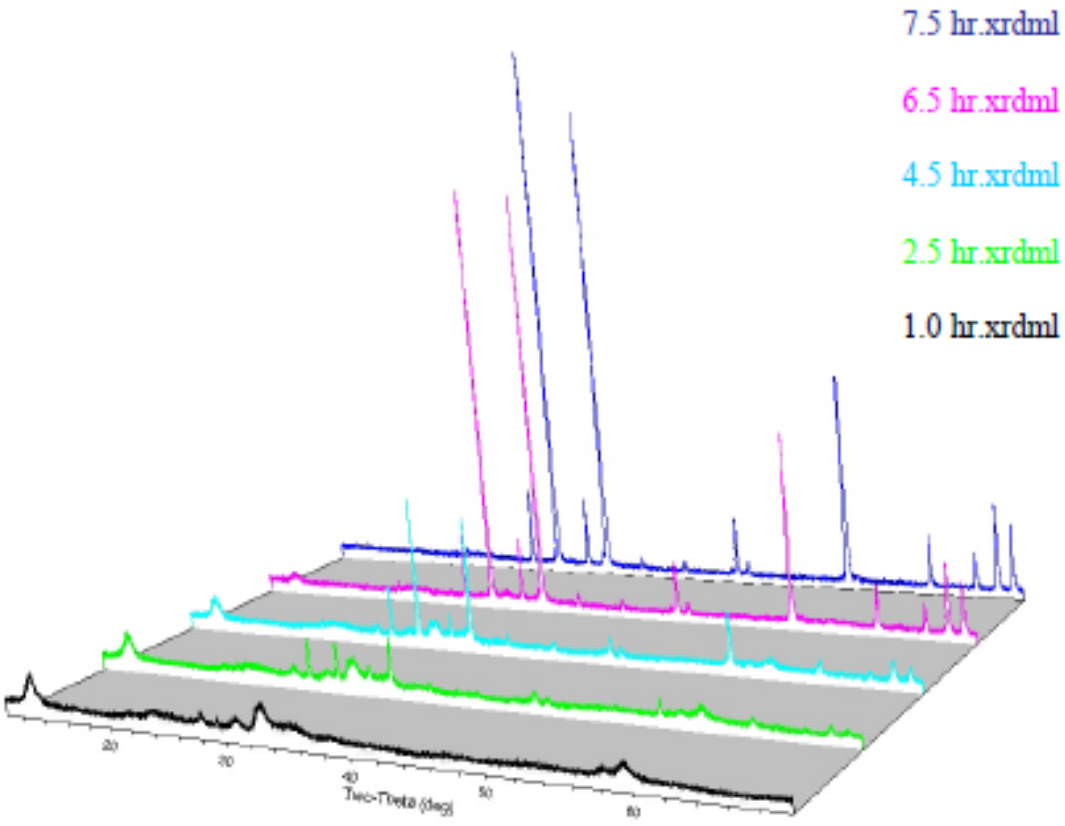

Figure 4-10 XRD spectrum of intermediate reactants at different time

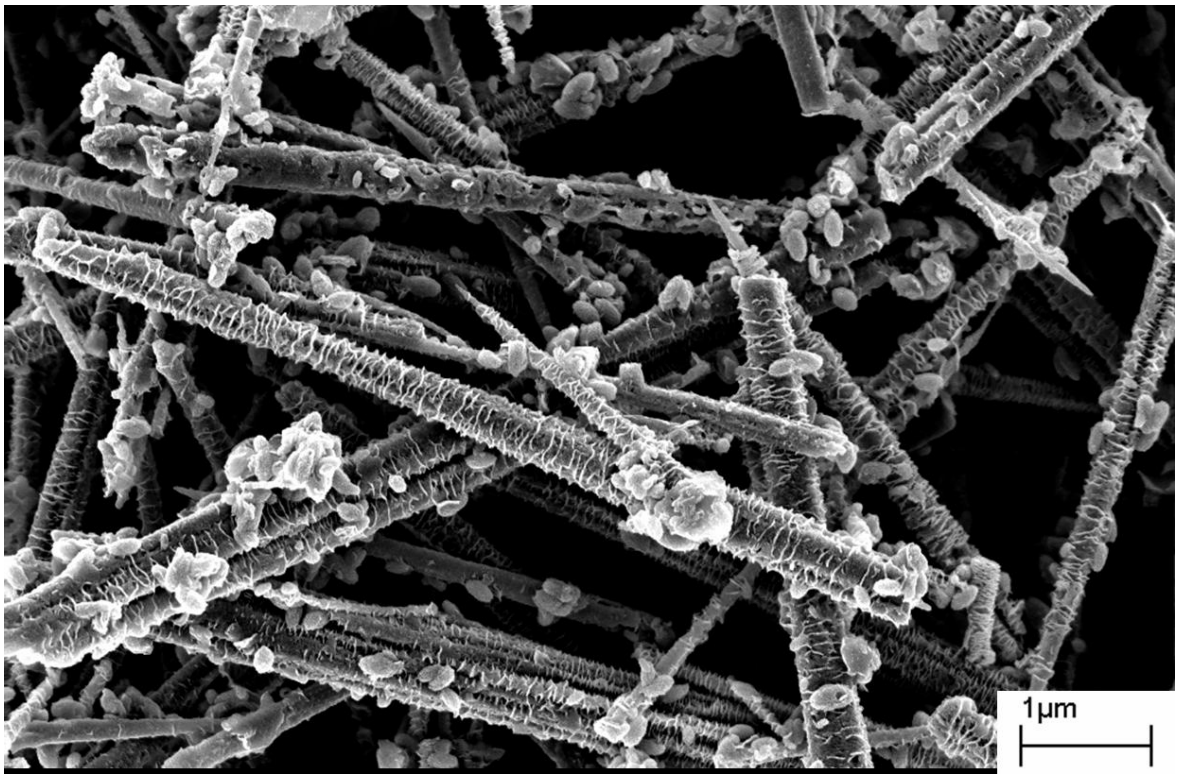

Figure 4-11 SEM micrograph of product with corn morphology after long time reaction (reaction time longer than 48 hours)

4.3.4 Preliminary kinetic study using head space gas chromatography

Further study of the kinetics of the growth process by head space gas chromatography (GC) took place. From the above XRD and SEM characterizations, we knew that the calcium carbonate could not be fully consumed. From the simple mass balance of carbonate ions, we could obtain the amount of carbonate ions consumed by determining the amount of the carbonate remaining in the reaction system, as described in Equation (4.5). The rate of the reaction, which could be

indirectly related to rate of carbonate ion consumption, could then be deduced. The amount of carbonate remaining in the reaction system could be determined from the amount of CO_2 released when acid was added to the carbonate materials.

$$[CO_3^{2-}]_{consumed} + [CO_3^{2-}]_{Zn\ Complex} + [CO_3^{2-}]_{unreacted} = \text{Constant} \qquad (4.5)$$

$$[CO_3^{2-}]_{consumed} = \text{Constant} - ([CO_3^{2-}]_{Zn\ Complex} - [CO_3^{2-}]_{unreacted}) \qquad (4.6)$$

In this experiment, we used head space GC to collect the released CO_2 and calculated the amount. The CO2 release reaction can be shown as follow:

$$CaCO_3 + HCl \qquad CaCl_2 + CO_2 + H_2O \qquad (4.7)$$

$$Zn_5(OH)_6(CO_3)_2 + HCl \qquad ZnCl_2 + CO_2 + H_2O \qquad (4.8)$$

For this study, a series of experiments were carried out for this study. All of the experiments were run under the same conditions, except that each of them was stopped from different reaction times. The mixtures from the different reaction times were then filtered to obtain the solid part. The particles were then washed with DI water and dried. A small amount of the powder was weighted and placed in a vial. HCl acid was added to the vial to dissolve the particles, which were a mixture of unreacted calcium carbonate, intermediate zinc complex, and possible zinc oxide nanorods. The HCl reacted with the unreacted calcium carbonate and zinc complex compound, which also contained carbonate ions as indicated by XRD analysis, to

release CO_2. The CO_2 released from the reaction was analyzed with the head space GC. The amount of carbonate ions consumed was derived from the amount of CO_2. Figure 4-12 shows the amount of released carbon dioxide from products obtained from different reaction times. It can be seen that the amount of released

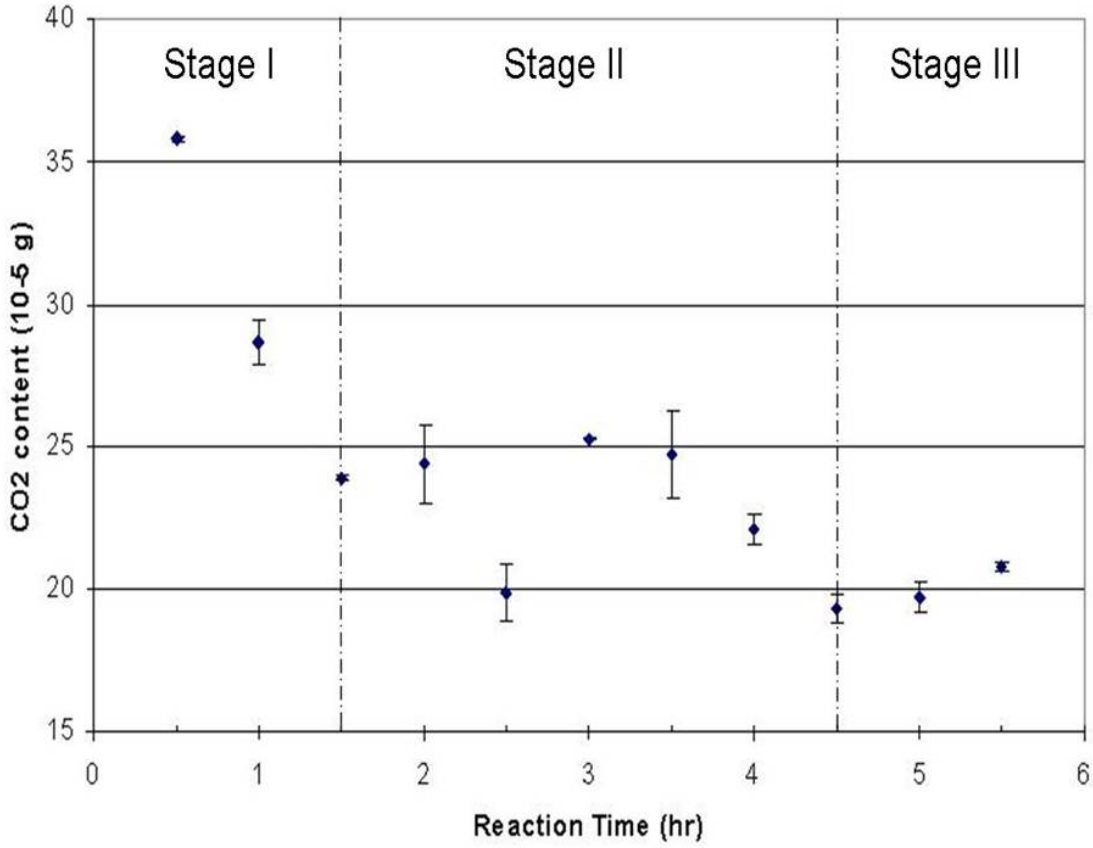

Figure 4-12 GC measurement of CO_2 in the reaction system

CO_2 in the first 1.5 hours was high due to the calcium carbonate that had not reacted in the mixture. However, the amount of CO_2 decreased rapidly during this period of time because the calcium carbonate was dissolved and consumed during the reaction.

A significant part of the carbonate ion was converted into $Zn(OH)_2$. This step transpired relatively quickly not only is calcium carbonate a supersaturation control agent but the particles are also sites for heterogeneous nucleation, which was energetically favored. The amount of CO_2 approached roughly to a constant level after 1.5-hour reaction and remained there for about three hours, indicating that the amount of carbonate ions in the mixture did not change and that a dynamic equilibrium between calcium carbonate and zinc complex existed in the reaction during this period. The CO_2 continued to decease to a low level and remained at the same level for the rest of the reaction. The final amount of CO_2 represented the remaining unreacted calcium carbonate, whose existence was also indicated by XRD analysis. The GC analysis agreed well with the results from the XRD analysis and the SEM observation.

4.4 Conclusion

This chapter demonstrated large scale ZnO nanorod synthesis, which was based on supersaturation control discussed in both this chapter and the previous chapter. That is, supersaturation should be well controlled in the synthesis of 1D nanostructure materials. At the same time, it was shown that supersaturation could be controlled using sparingly soluble carbonate salts. Because of the slow hydrolysis of carbonate ions, the carbonate salts act as a buffer that provides a necessary ion count for coprecipitation.

The formed nanorods are 200-300nm in diameter and as long as 10 micrometers long. Various characterizations revealed that the growth of the nanorods could be roughly divided into three stages. In the first stage, calcium carbonate hydrolyzed and reacted with zinc ions to form zinc carbonate hydroxide. In the second stage, a process involving both a dynamic equilibrium between calcium carbonate and zinc complex and the conversion from zinc complex to ZnO nanorods took place. In the final stage, the zinc complex was converted to ZnO. From the time scale of each step, we could determine that the limiting step of nanorod growth in this reaction system was the conversion of zinc complex to nanorods. Morphologically, these stages were characterized by the formation of nanosheets, or "egg" seeds formation for nanorods, and the growth of large number of nanorods, respectively.

The experimental conditions also played important roles in the development of nanorod morphology. The reaction temperature below the boiling point of the solution could not produce any nanorods. However, nanosheets were formed below the boiling points, further suggesting the limiting step was the conversion of zinc complex. Mixing played a role at least as important a role as temperature. Without mixing, only irregular particles were obtained, even when the temperature was at a boiling point.

Although ZnO nanorods were synthesized on a large scale at a relatively low cost compared to the CVD methods and supersaturation control was successfully

demonstrated, the ZnO nanorods obtained in this reaction had low quality. Both the surfaces and both ends of the nanorods contained macroscopic defects. Furthermore, the final products were mixed with unreacted calcium carbonate or intermediate reactants. Separating ZnO nanorods from those particles that had not reacted is very difficult. Therefore, if this reaction system is used, a quantitative study of ZnO nanorod growth with supersaturation control will be challenging. Thus the establishment of a quantitative relationship between supersaturation and 1D nanomaterial requires a new model system.

Chapter 5 : Kinetics study of ZnO Nanorod Growth

In previous Chapters 3 and 4, we demonstrated the synthesis of 1D nanostructures using sparingly soluble salts as supersaturation control agents. We have found that nanostructure growth is an extremely complicated process and many factors, such as supersaturation, temperature, and mixing, account for the precise control of the growth process. These factors control not only the final morphology of the products but also the growth rate. Compared with the intensive interest and discovery in the synthesis and novel properties of nanostructures, the fundamental study of kinetics has attracted little attention. The kinetic study of nanomaterial growth can lead a greater understanding of and better control of the growth process. As previously discussed, ZnO is a material with both industrial and scientific importance. Therefore, an understanding of the mechanism of ZnO nanostructure growth in solution will significantly contribute to the research and application of this material. Furthermore, the kinetic study of nanorod growth in solution can be a stepping stone for the large-scale production of nanostructure materials and provide insight into the synthesis of similar nanomaterials.

Chapter 4 presents a large-scale synthesis of ZnO nanorods. However, for the quantitative study of kinetics, we need to accurately measure the process variables. However, if the synthesis method in previous chapter is used, the separation of ZnO nanorods from unreacting or intermediate reactants will remain a challenge. To

address this problem, this chapter will introduce a new reaction system for quantitatively studying the relationship between supersaturation and 1D nanomaterials.

5.1 Introduction

As previous discussed in Chapter 4, ZnO nanostructures have very promising applications in various areas such as electronics and optoelectronics. In order to fully explore these applications, various techniques, including both the vapor and solution phases, have been developed to synthesize nanostructured ZnO. Due to its flexible route and low cost, the solution phase is becoming more and more popular for the synthesis of ZnO nanostructures. For example, ZnO nanoparticles 2 to 7 nm in size can be prepared by adding dropwise LiOH methanol solution to a $Zn(Ac)_2$ solution at a temperature of 0^oC [189]. The two most important parameters in controlling the size of the nanoparticles were temperature and water content. Through monitoring of the nucleation, growth, and aging processes by means of the chemical and electrostatic control of the interfacial free energy, ZnO nanorod arrays have been successfully synthesized in aqueous solution [190]. Equimolar $Zn(NO_3)_2$ and hexamethylenetetramine (HMT) were dissolved in DI water and the mixture was heated up to 95^oC. Various substrates such as fluorine doped SnO2 glass, single crystal sapphire, Si/SiO2 wafer, or substrates coated ZnO thin films were floating on top of the solution. In these case, vertically aligned ZnO nanorods 100 to 200 nm in

diameter and up to 10 μm long can be grown on the substrates. Various factors controlling the growth have been evaluated [191, 192]. It was found that factors such as ligands, counter ions, pH, ionic strength, substrate, deposition time, and supersaturation can affect the growth of nanostructure ZnO.

Compared with tremendous efforts in developing method of synthesis and discovering the diverse properties of nanostructures, few kinetic studies can be found in the literature. The kinetic study of nanocrystals involves both the size determination and nanoparticle concentration. Accurate measurements of the diameter of the nanocrystal can be achieved through TEM observations or the light scattering method. However, obtaining statistical significance of the diameters of nanostructure from TEM observations can be very time consuming. The light scattering technique, on the other hand, yields a statistical average of particle size, but the particle size must be very strictly controlled, which is still a challenge for synthesis. The other disadvantage of the light scattering method is that measurement assumes a spherical shape of particles, rendering it not appropriate method for high aspect ratio 1D nanomaterial study.

With all the remaining challenges, researchers have conducted kinetic studies for various nanomaterials. Nair investigated the kinetics growth of single-walled aluminogermanate nanotubes roughly 20nm long [193]. Due to the relative short length of the nanotubes, a spherical diameter was assumed and the length of the

nanotubes was then obtained with dynamic light scattering. From UV-vis spectroscopy, the concentration of the nanotubes could be obtained. A quantitative kinetic model was proposed to capture the essence of the two-step nanotube growth mechanism. Searson investigated the ZnO nanocrystal aging kinetics in a 2-propanol medium with NaOH as coprecipitation agent [194-196]. The nanoparticle sizes studied in their research were less than 5 nm. The size was determined by high resolution TEM and the concentration was determined through optical band edge absorption. It was found that the nanocrystal growth kinetics followed the classic Ostwald ripening mechanism, that is, the crystals grew at the expense of consuming smaller crystals because the crystals of smaller diameter had high curvature, resulting in high dissolution. During the aging process, the volume of the nanocrystal increased linearly with time, indicating that aging is a diffusion-limited process. However, Sarma reported that the aging process did not follow the well known diffusion-controlled Ostwald ripening mechanism[197]. The aging process showed a significant lower rate than that derived from Ostwald ripening mechanism and depended on the concentration of NaOH in a nonmonotonic way. Further experiments confirmed that the deviation was caused by the counter ion Na^+ which together with hydroxyl group formed an adsorption layer around the ZnO nanocrystals. Based on population balance model, Bandyopadhyaya [198] reported the kinetic formation of pearl-chain ZnO nanorods from nanodots through oriented attachment [199]. In the early stage of the synthesis, the nanodots formed aggregates through coalescence which further leads to phase transformation to nanorods. The oriented attachment was directed by

the dipole-dipole and van der Waals interaction between the nanodots. A combination of the oriented attachment and Ostwald ripening can both work in nanocrystal growth [200].

In this section, we established a kinetic model to describe ZnO nanorods growth from solution. We used a $Zn(NO_3)_2$ and hexamethylenetetramine (HMT) system to synthesize ZnO nanorods because the system was reported to synthesize high quality ZnO nanorods. The reactant zinc ion concentration and the length of the nanorods were tracked using different characterization tools. The concentration of zinc ions was measured with the inductive couple plasma (ICP) method, and the length of the nanorods was obtained through SEM measurement. The concentration of Zn^{2+} and the length of the nanorods were then correlated to provide kinetic information about nanorod growth. The results showed that the concentration profile of zinc ions in solution followed a first order reaction mechanism.

5.2 Experimental Section

5.2.1 Synthesis

At room temperature, 0.15 g zinc nitrate 6-hydrate was dissolved in 100 ml of deionized (DI) water in a beaker, and 0.07 g hexamethylenetetramine was added to the above solution which was clear at room temperature. The beaker was then

covered with aluminum foil and heated to the required temperature (55, 65, 75, and 85^{o}C) on a hot plate. The reaction was maintained for at least three hours. Samples were withdrawn from the reactor at different times, filtered through 20nm filters, and the filtered solution was put in an inductively coupled plasma (ICP) matrix solution that was a 5% HCl and 3% HNO_3 aqueous solution. At the same time, a drop of sample was taken from the reactor for SEM observation. After the reaction was complete, a white milky suspension was obtained. The product was washed with DI water to remove unreacted reactants and other water soluble impurities.

5.2.2 Sample characterization

SEM with energy-dispersive X-ray spectroscopy (EDS) and XRD were applied to characterize the size, shape, composition, and structure of the synthesized nanorods. SEM observations and an EDS analysis were conducted on an LEO 1530 thermally-assisted field emission (TFE) scanning electron microscope. XRD patterns were recorded on a X'Pert PRO X-ray diffractometer (PANalytical) using Cu K_{α} ray (λ = 1.54 Å) as the radiation source.

The analysis of the concentration was done through inductively coupled plasma (ICP) spectrometry, a technique used for elemental analysis. The ICP solution matrix, which is a 5% HCl and 3% HNO3 aqueous solution, was made. About 20 grams of the matrix solution was used for each sample. About 0.5 grams sample was

taken from the reaction suspension, filtered with 20nm filter, and dissolved in the ICP matrix solution.

For the SEM analysis, samples from different reaction times were imaged at different locations. The length of the rods was determined using a free image processing software ImageJ (version 1.41). The software is developed by NIH and capable of displaying and analyzing images. ImageJ can measure the length any object defined by users. More details about the software can be found at http://rsbweb.nih.gov/ij/docs/intro.html.

5.3 Results and Discussion

5.3.1 Product characterization

The products were studied with SEM and the morphology of nanorods were shown in Figure 5-1. Compared with the nanorods previously synthesized using $ZnSO_4$ and $CaCO_3$ (discussed in Chapter 4), the nanorods were much cleaner. They were about 3-5 μm long after about three-hour reaction and exhibited a hexagonal cross section. Each side of the hexagonal cross section was about 200-300 nm long. The surfaces of the nanorods were not microscopically smooth, but instead, the tips of the nanorods contained of many particles, suggesting that the nanorods were synthesized through re-organizing nanoparticles.

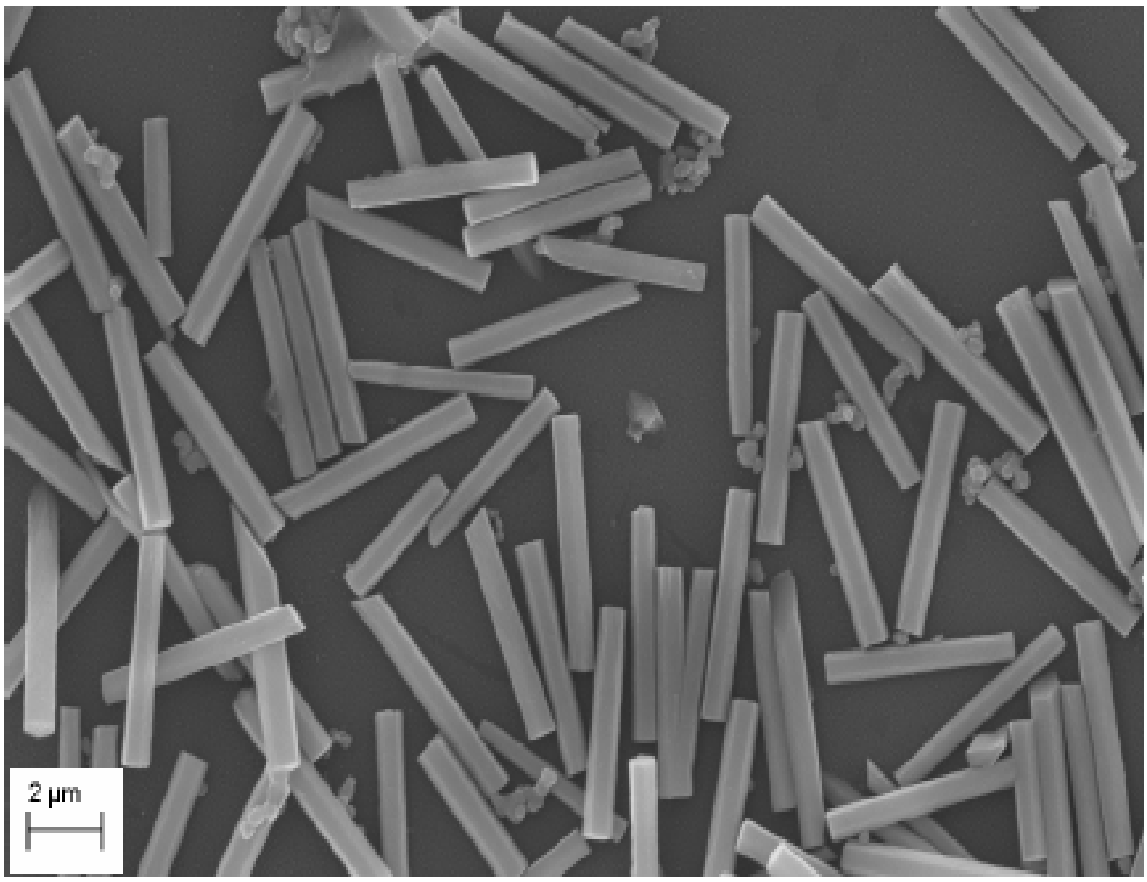

Figure 5-1 SEM of ZnO nanorods

ZnO nanorods obtained at different reaction times were imaged with SEM to measure their lengths. Figure 5-2 shows these SEM images of the nanorods at various times from at different temperatures. The lengths of the rods were then measured with ImageJ software.

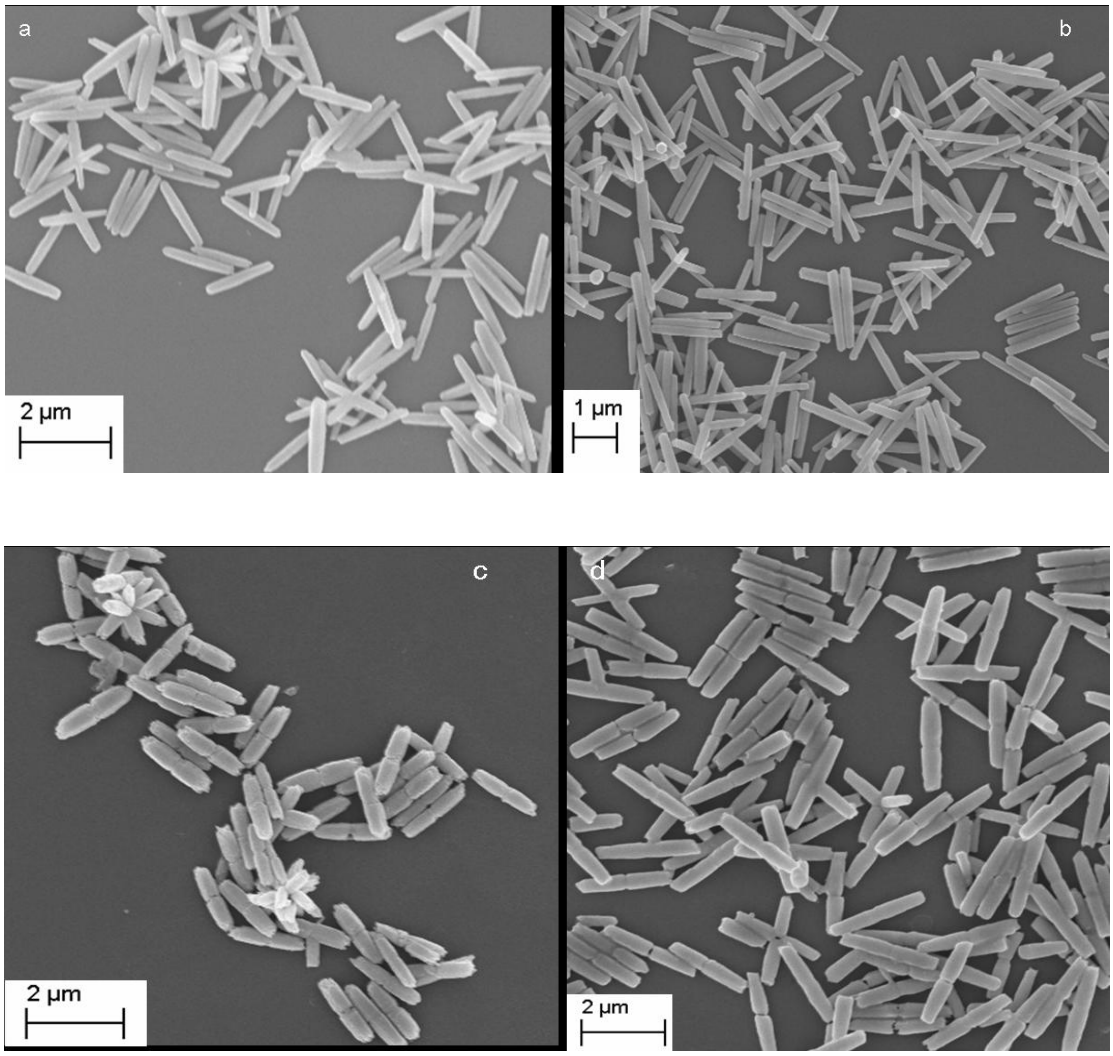
a
2 µm
b
1 µm
c
2 µm
d
2 µm

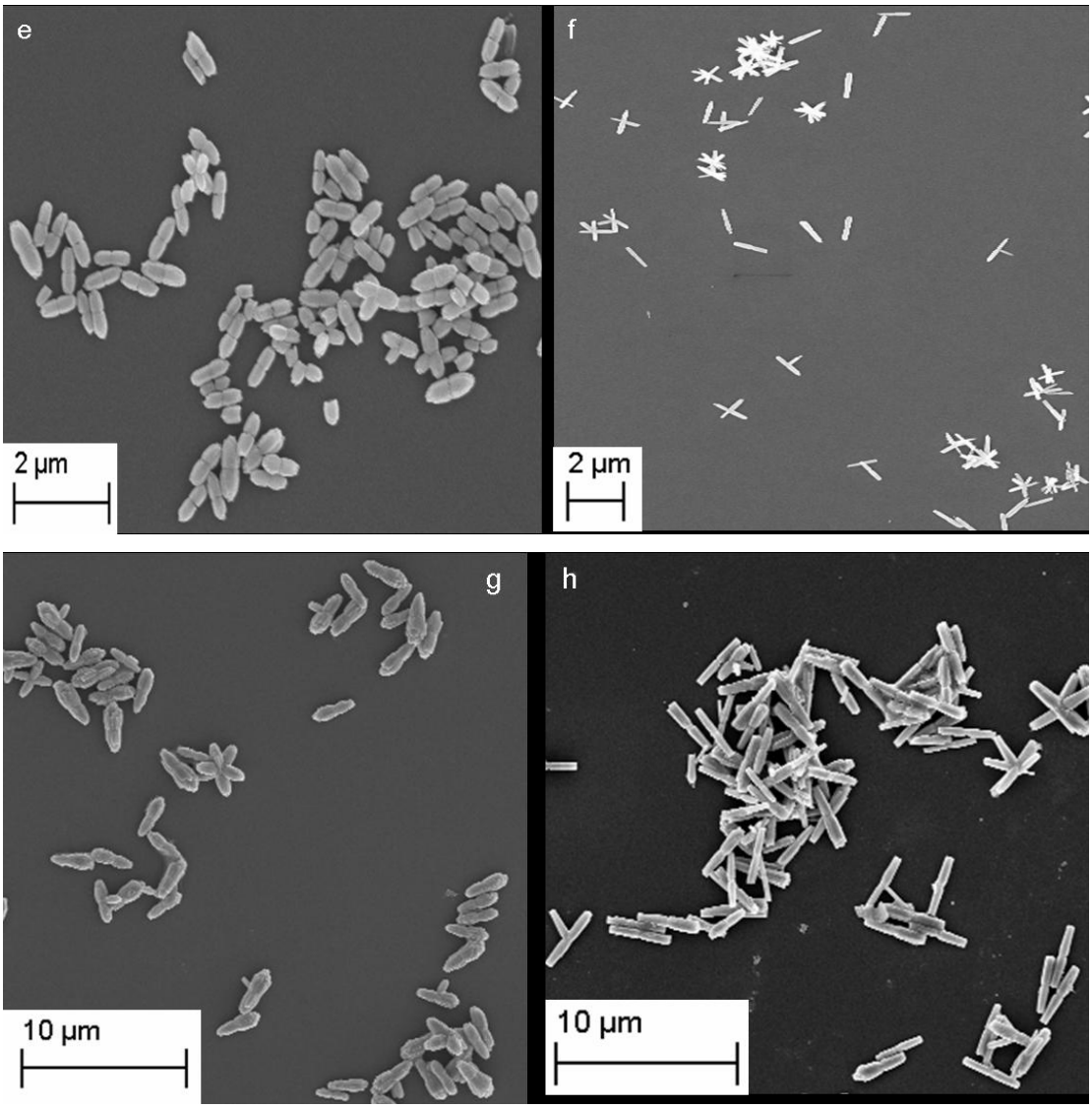

Figure 5-2 SEM micrograph of the ZnO nanorods at different temperatures a), b) T=85^{o}C;. c),d) T=75^{o}C; e),f) T=65^{o}C; g),h) T=55^{o}C

The XRD spectra of the nanorods were also collected. Figure 5-3 shows the XRD pattern of ZnO nanorods after a three-hour reaction. The spectrum showed very sharp diffraction peaks, suggesting high crystallinity of the ZnO nanorods. The three strongest peaks at 2θ =31.89, 34.64, and 36.40 can be attributed to diffraction from

(100), (002), and (101) planes, respectively. These characteristic peaks corresponded well to those in the database. (JCPDS 036-1451), and clearly showed that the final products were crystalline ZnO.

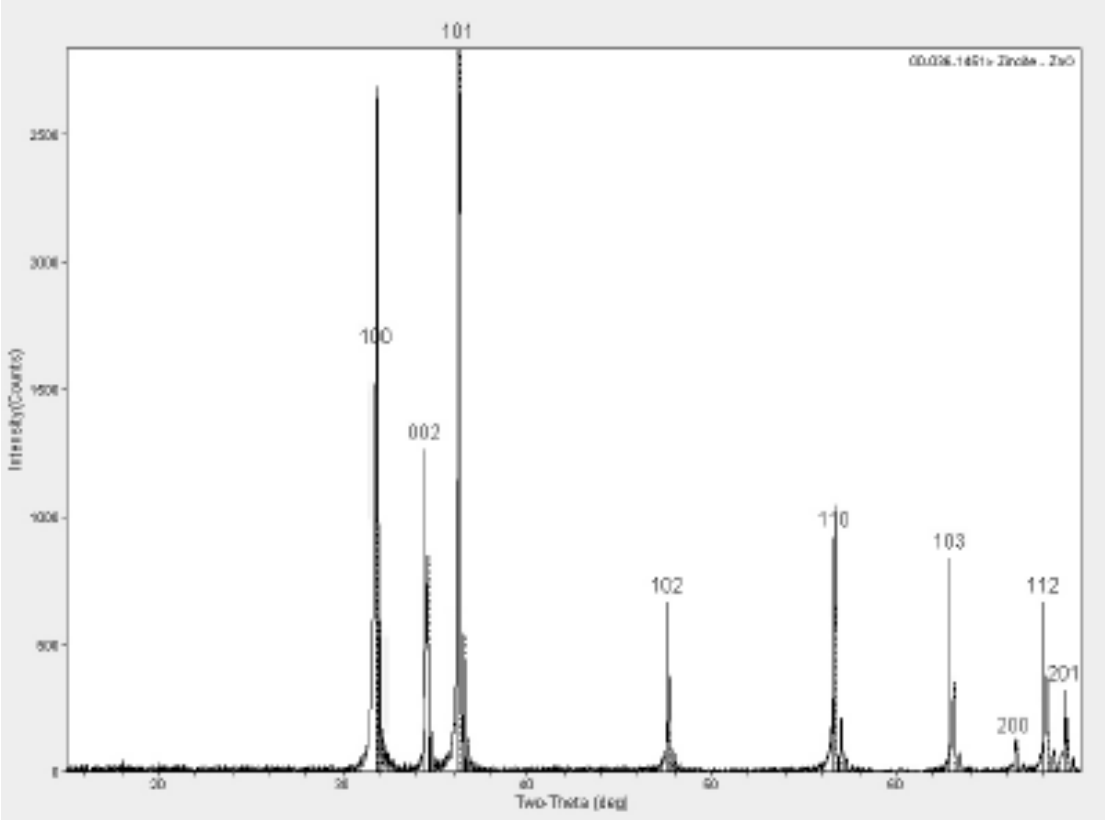

Figure 5-3 XRD spectrum of the ZnO nanorods

5.3.2 Quantitative kinetic model

The zinc nitrate and HMT system has been widely used to synthesize ZnO nanorods [105, 178, 201]. The role of HMT is still not well understood. It is generally

accepted that HMT served as a buffer to slowly provide OH^- ion during hydrolysis. Briefly, the HMT first hydrolyzes to produce formaldehyde and ammonia, and the ammonia then further hydrolyzes to provide OH^- and NH_4^+. The OH^- ion will form complex compound with Zn^{2+}. The zinc compound then decomposes into ZnO under given reaction conditions. The chemistry of the entire process, which is relatively rather complex, is summarized as follows [105]:

$$C_6H_{14}N_4 + 6\,H_2O \dashrightarrow 6CH_2O + 4\,NH_3 \qquad (5.1)$$

$$NH_3 + H_2O \dashrightarrow NH_4^+ + OH^- \qquad (5.2)$$

$$Zn^{2+} + 4OH^- \dashrightarrow Zn(OH)_4^{2-} \qquad (5.3)$$

$$Zn(OH)_4^{2-} \dashrightarrow Zn(OH)_2 + 2OH^- \qquad (5.4)$$

$$Zn(OH)_4^{2-} \dashrightarrow ZnO + H_2O + 2OH^- \qquad (5.5)$$

And the overall reaction of ZnO nanorod formation can be simplified as follows:

$$\underset{A}{Zn^{2+} + 2OH^-} \rightleftharpoons \underset{B}{Zn(OH)_2} \xrightarrow{k} \underset{C}{ZnO + 2H_2O} \qquad (5.6)$$

Because the reaction between Zn^{2+} and OH^- take place very rapidly, a quasi-steady state can be assumed for this reaction. Then the $Zn(OH)_2$ then further decomposes to ZnO under reaction conditions. The overall reaction then can be described with three first order reactions:

$$\frac{dC_A}{dt} = -k_1 C_A + k_{-1} C_B \tag{5.7}$$

$$\frac{dC_B}{dt} = k_1 C_A - k_{-1} C_B - k_2 C_B \tag{5.8}$$

$$\frac{dC_C}{dt} = k_2 C_B \tag{5.9}$$

C_A, C_B, and C_C are the concentration of Zn^{2+}, $Zn(OH)^2$, and ZnO, respectively, and k_1, k_{-1}, and k_2 are the reaction rate constants.

By assuming quasi steady state of first reaction, i.e., $\frac{dC_B}{dt} = 0$, we can solve the above equations:

$$C_A = C_{A0} e^{-Kt} \tag{5.10}$$

$$C_B = \frac{k_1}{k_{-1} + k_2} C_A = \frac{k_1}{k_{-1} + k_2} C_{A0} e^{-Kt} \tag{5.11}$$

$$C_C = C_{A0} - C_A - C_B = C_{A0}(1 - e^{-Kt} - \frac{k_1}{k_{-1} + k_2} e^{-Kt}) \quad (5.12)$$

Here, K is the apparent reaction rate constant defined as follows:

$$K = \frac{k_1 k_2}{k_{-1} + k_2} \quad (5.13)$$

By assuming 1) the nucleation is negligible after crystals growth begins; 2) the growth rate of nanorods in axial direction is much higher than that in radial direction and the length distribution of the nanorods is uniform, we can correlate the lengths of the nanorods L(t) with the Zn^{2+} concentration in a similar way.

$$\frac{dL}{dt} = kC_A = kC_{A0} e^{-Kt} \quad (5.14)$$

where k is the apparent reaction rate constant.

The above solution can be solved as follows:

$$L(t) = \frac{k}{K}(1 - e^{-Kt}) \quad (5.15)$$

5.3.3 Model fitting and validation

The above models were then validated by fitting them to the experiment data. Figure 5-4 shows the Zn^{2+} concentration from the ICP analysis from different temperatures.

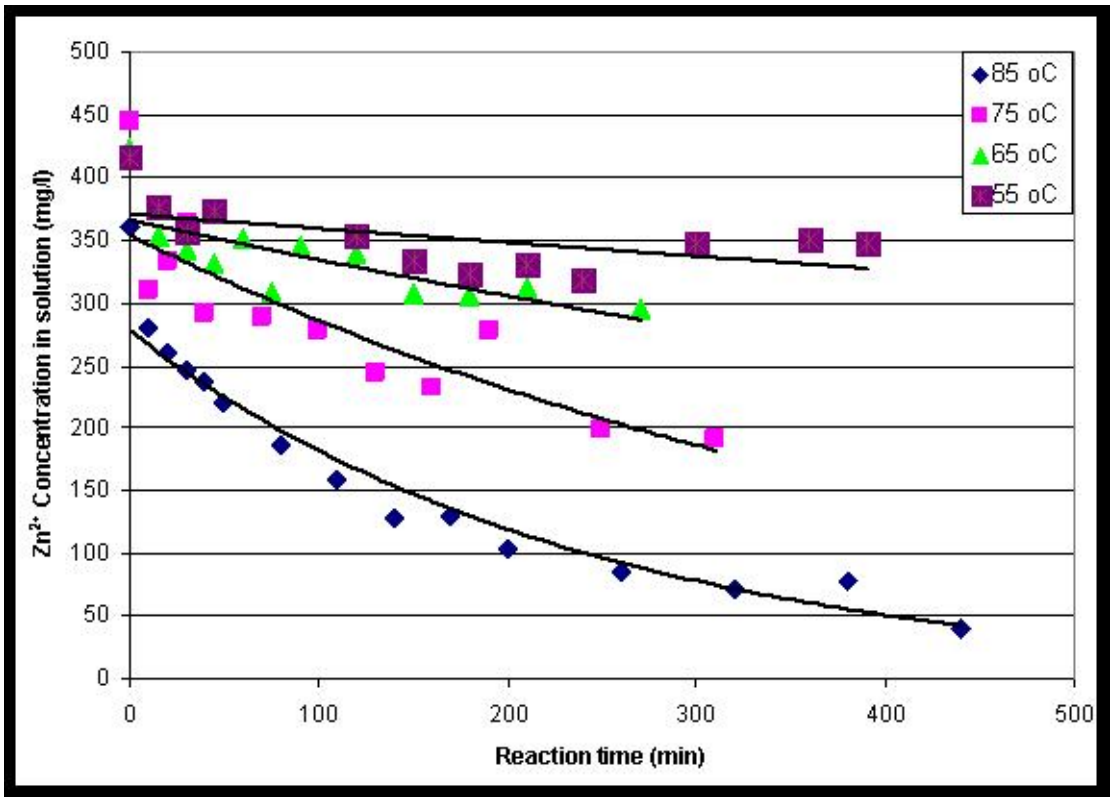

Figure 5-4 Zn^{2+} concentration in the reaction solution

From the above figure, we can see that the Zn^{2+} in the solution can be fitted to the first order reaction, which agrees well with Equation (5.10). The fitted parameters were summarized in Table 5-1.

Table 5-1 Fitted parameters for reactions

Temperature (oC)	Reaction Constant K
85	0.0035
75	0.0021
65	0.0009
55	0.0003

The fitted apparent reaction rate constant can be correlated to the temperature by Arrhenius's law, as shown in Figure 5-5. The activation energy obtained from the correlation is 80.52 kJ/mol.

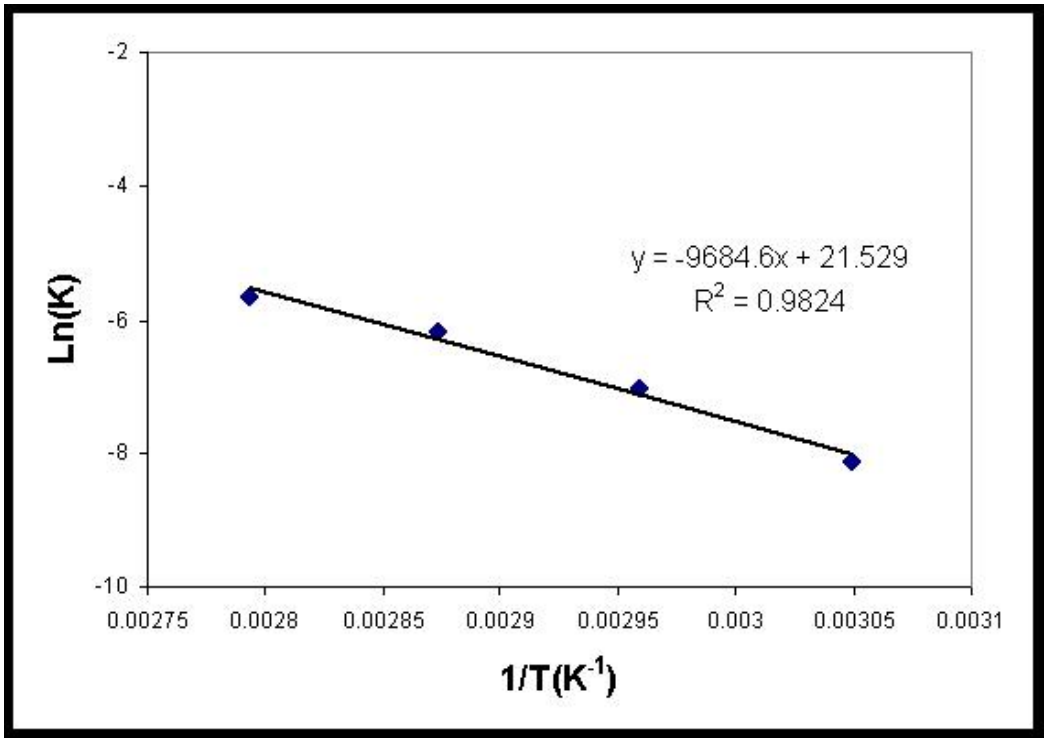

Figure 5-5 Activation energy from the fitted reaction rate

For each experimental temperature, the lengths of the nanorods were obtained from the SEM images, shown in Figures 5-6.

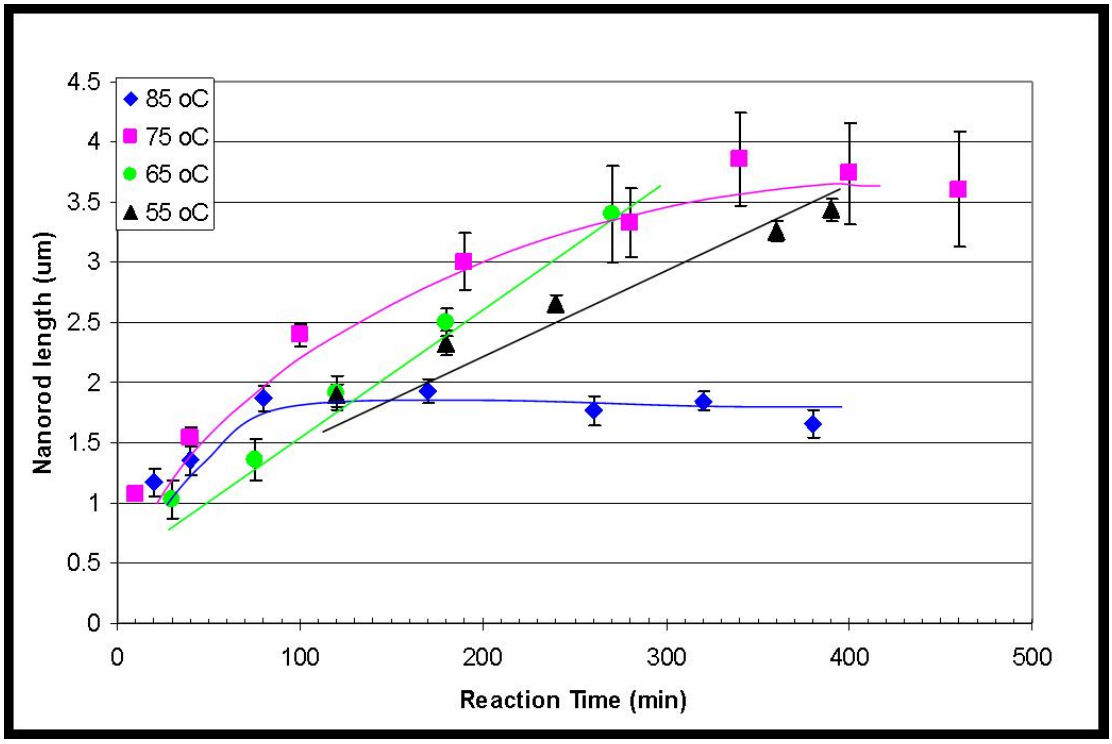

Figure 5-6 Average nanorod from the SEM analysis

We can see from the Figure 5-6 that the lengths of the nanorod increase with increasing temperature except at a temperature higher than 85^{o}C. At a temperature of 85^{o}C, the nanorods grew to certain length and then could not grow any further, which agreed well with experimental observations and predictions from Equation 5-15. The higher the activation energy is , the more rapidly the lengths approach a constant. Crystal growth can be divided into two stages: nucleation and crystal growth. At high temperatures, HMT decomposed faster and provided more OH^- ions, resulting in a

high supersaturation level in the solution which is beneficial for nucleation. At low temperatures, however, HMT decomposed slowly and OH^- concentration was relatively low. The supersaturation level in the solutions is not high enough to promote nucleation but crystal growth can occur at relatively low supersaturation, as summarized in Figure 5-7 [202, 203].

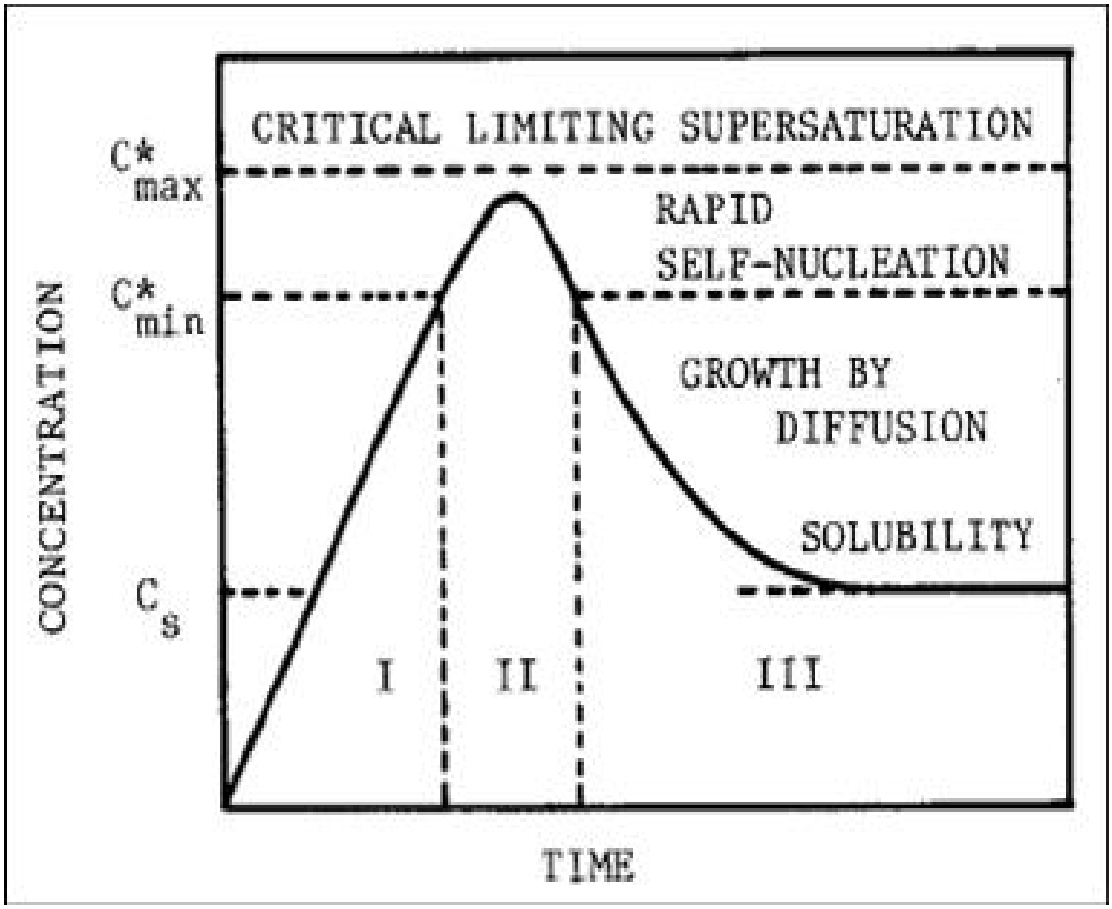

Figure 5-7 Lamer diagram showing the relationship among nucleation, crystal growth, and concentration

5.4 Conclusion

To extract the essence of the mechanism governing the nanorod growth, this chapter investigated the kinetics of ZnO nanorod growth in the solution phase. High quality ZnO nanorods were synthesized using the HMT and $Zn(NO_3)_2$ reaction system in solution. Because HMT in an aqueous solution can undergo decomposition and release OH^- ions. It can be used as a supersaturation control agent. The products were characterized using a variety of different techniques. In the SEM technique, micrographs showed that the nanorods have a hexagonal cross section around 200-300 nm in diameter and several micrometers long. As the nanorods obtained from this method were in pure form, they are suitable for kinetics study. Using ICP technique, the concentration of Zn^{2+} ions in solution was analyzed and the lengths of the nanorods were obtained from SEM micrographs with ImageJ software. The concentration of Zn^{2+} ions could be fitted to a first order reaction mechanism. Correlation between the concentration of zinc ions and the length of nanorods was built. The growth rate of nanorods increased with increasing temperatures in certain range. The length of the nanorods will approach a constant after a certain reaction time. The higher the temperature is , the faster the length approach a constant. The reason was that the HMT decomposed faster at high temperatures and resulted in a high supersaturation level in solution, which was beneficial for nucleation. On the other hand, when the HMT slowly hydrolyzes at low temperatures, the supersaturation is lower and the driving force is not high enough for nucleation.

Nevertheless, crystal growth can take place at low supersaturation. Therefore, the control of supersaturation is not only critical to the final morphology of the nanostructure but also important in the growth kinetics. In order to grow desired nanorods, supersaturation has to be finely controlled during entire synthesis process.

Chapter 6 : Nanosphere Synthesis: Effect of Experimental Conditions on Nanostructure Growth

Based on the previous studies, we have shown how supersaturation affect the morphology of the final product and the kinetics of the growth. Prior studies and experimental observations in this thesis suggest that supersaturation alone is not sufficient to ensure a 1D structure. Other process parameters could have an equally important effect as supersaturation in controlling the morphology of nanomaterials. For example, in Chapter 3, we found that when there was no mixing applied, only irregular particles but no nanobelts were produced. In this chapter, we further examine the effect of mixing on the morphology of the final nanomaterials. When mixing was applied to the reaction system used in Chapter 5, the nanomaterial morphology was changed to nanospheres. The nanospheres were characterized with different techniques and it was revealed that the nanosphere was a combination of ZnO and $Zn(OH)_2$. The mechanism behind the growth was the breakdown of the free diffusion of building blocks to the nanocrystal surfaces.

6.1 Introduction

Studies in the literature have focused considerable attention on not only 1D nanomaterials but also nanospheres and hollow nanospheres. Due to their low density

and high surface-to-volume ratio, nanospheres have been applied in catalysis [204, 205], drug delivery [206], chemical separation [207], and gas sensors [208]. Various methods used to synthesize nanospheres and hollow nanospheres have been employed [73, 209-215]. The most commonly used method to synthesize hollow spheres is the sacrificed template technique. In this method, the target nanoparticles adsorb on the surface of templates such as polystyrene spheres or inorganic spheres, such as SiO_2. The core of the particle is then removed by calcination, chemical and physical etching, or dissolution with a good solvent [215]. A wide range of materials have been synthesized with nanosphere or hollow nanosphere morphology. As an important catalyst and pigment, TiO_2 hollow spheres have been synthesized by coating titanium tetraisopropoxide (TTIP) on cationic polystyrene spheres in an ethanol environment. The polystyrene cores were then removed either by using a solvent such as toluene or by calcination at 600^{o}C. After the cores were removed, the final products maintained the spherical morphology of the polystyrene template [216].

Several researchers have investigated the synthesis of ZnO nanospheres [217, 218]. Both Xiao's and Xu's groups synthesized ZnO hollow nanospheres using carbon nanospheres as templates. Carbon nanospheres were first synthesized, and they were used as templates providing either reaction sites or adsorption sites during the ZnO growth. Although the template method is dominant in synthesizing hollow spheres, it involves several disadvantages. One is that certain templates must be prepared; and another is that several researchers have found that the adsorption of

metal ions on the template is limited [217]. In addition, removing the core material without damaging the shell is usually difficult. Thus, it would be advantageous to synthesize metal oxide nanospheres/hollow spheres directly from the reaction process.

This chapter introduced a simple new method of synthesizing ZnO nanospheres in water solution at low temperatures. The method requires no template for the formation of nanospheres. The product is characterized with different instruments and a formation mechanism is proposed based on the observations of experimental phenomena and results of characterizations.

6.2 Experimental Section

Materials: The chemicals zinc nitrate 6-hydrate and hexamethylenetetramine (HMT) were purchased from Aldrich and used without further treatment.

Synthesis of ZnO Nanosphere/Hollow nanospheres: A description of one example of the synthesis procedure follows. At room temperature, 0.15 g zinc nitrate 6-hydrate was dissolved in 100 ml deionized (DI) water in a beaker, and 0.07 g HMT was added to the above solution after the zinc nitrate was fully dissolved. The solution at room temperature was clear. The beaker was then covered with aluminum foil and heated to a desired temperature of around 75^{o}C on a hotplate under magnetic stirring at a speed of 200-300 rpm. The reaction was maintained for about three hours.

After the reaction was complete, a milky suspension was obtained. The product was washed with DI water to remove unreacting reactants and other water soluble impurities. Half of the final product was freeze-dried, and they were calcinated at 600^{o}C in a furnace for 30 minutes to obtain hollow nanostructures.

Sample Characterization: SEM with energy-dispersive X-ray spectroscopy (EDS), XRD, and TEM were applied to characterize the size, shape, composition, and structure of the synthesized hollow nanospheres. SEM observations were conducted on a LEO 1530 thermally-assisted field emission (TFE) scanning electron microscope with an acceleration voltage of 5 kV. TEM and SAED analyses were carried out on a JEOL 4000EX type high resolution TEM. XRD patterns were recorded on a X'Pert PRO X-ray diffractometer (PANalytical) using Cu K_α ray (λ = 1.54 Å) as the radiation source. Thermogravimetric analysis was performed on a Netzsch STA 449C under N_2 and the heating rate was 10 ^{o}C/min.

6.3 Results and Discussion

6.3.1 Product before calcination

Figure 6-1 shows that the as-synthesized product possesses the morphology of a nanosphere. The estimated diameters of nanospheres ranged from 200nm to 1 μm. The image of the nanospheres showed that the surfaces of the nanospheres were

rough. It was interesting to notice that the nanospheres were consisted of aggregated nanoparticles. The size of the primary crystal particles were less than 10 nm.

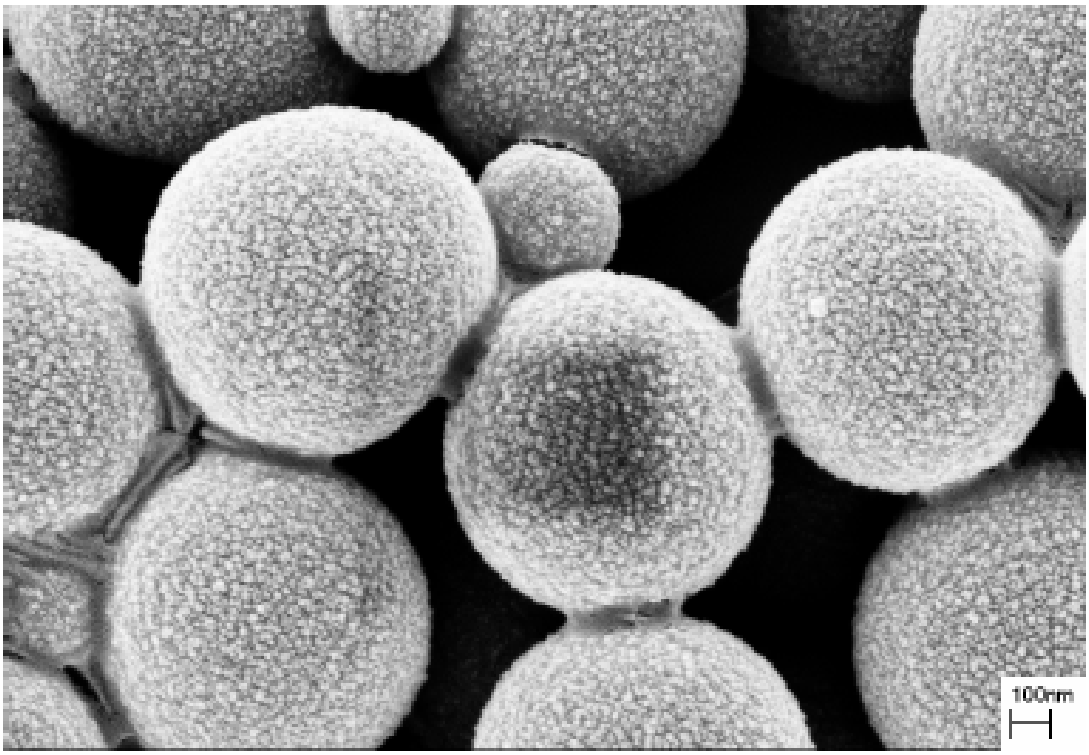

Figure 6-1 SEM of the nanospheres

The XRD spectra of as-synthesized products were shown in Figure 6-2, which indicated that the products are mainly amorphous. The figure reveals a small diffraction peak of around 2θ of 56^{o} which could be attributed to the ZnO (110) plane (JCPDS No. 36-1451). However, the majority of the product did not consist of crystalline ZnO.

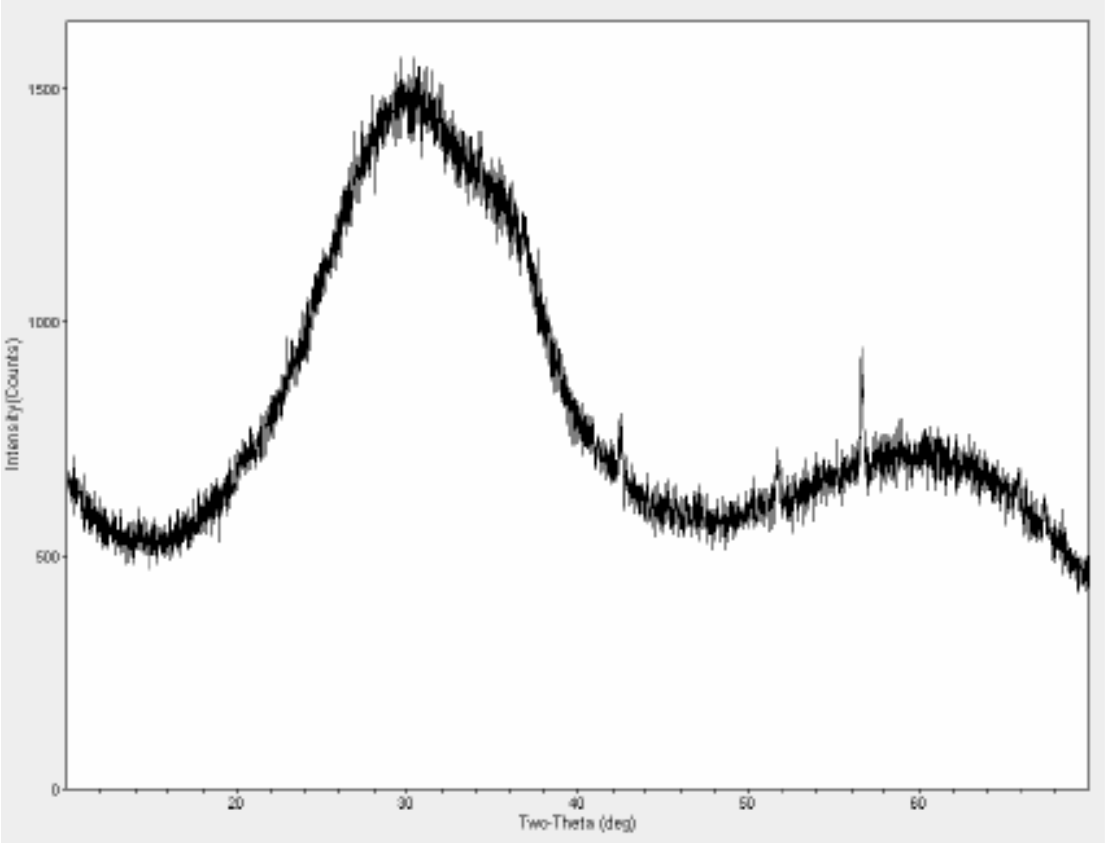

Figure 6-2 XRD spectrum of as-synthesized nanospheres

Figures 6-3a and 6-3b show low magnification TEM micrographs of as-synthesized products, which reveals that some of the nanospheres are solid, as in Figure 6-3a, and some of the nanospheres are partially empty or hollow inside the particles, indicated by the bright contrast in the micrograph in Figure 6-3b. The inset in Figure 6-3a illustrates an electron diffraction pattern taken from a single sphere. The ring patterns suggest that these spheres are polycrystalline. The high resolution TEM micrograph, shown in Figure 6-4, reveals that the nanospheres consist of many nanocrystals less than 10 nm in size and oriented in different directions, which is consistent with the observations from the SEM and XRD spectra.

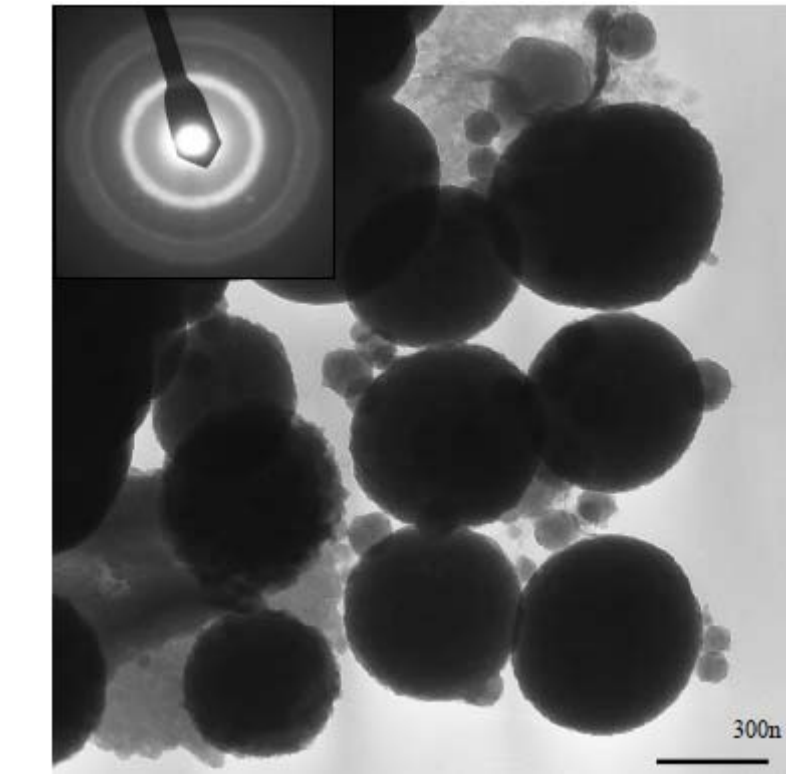

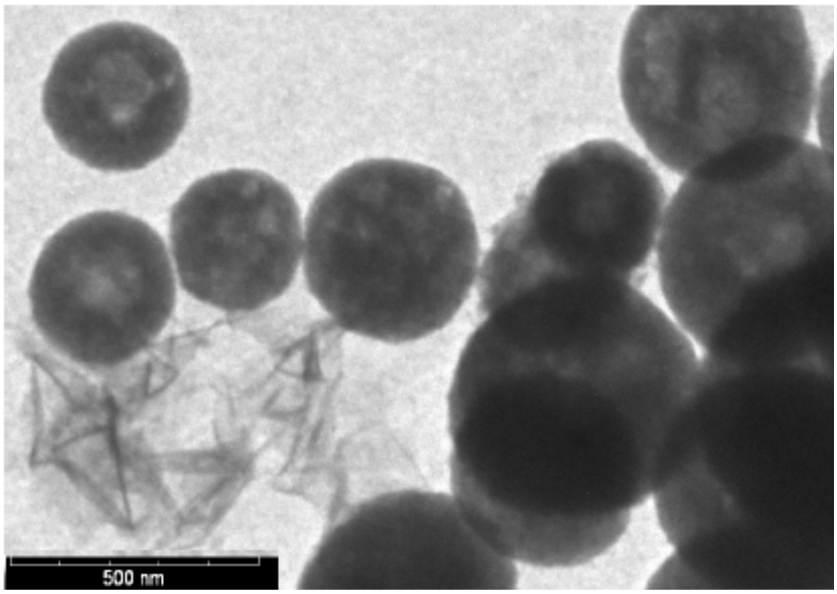

Figure 6-3 TEM micrograph of (a) solid and (b) hollow spheres

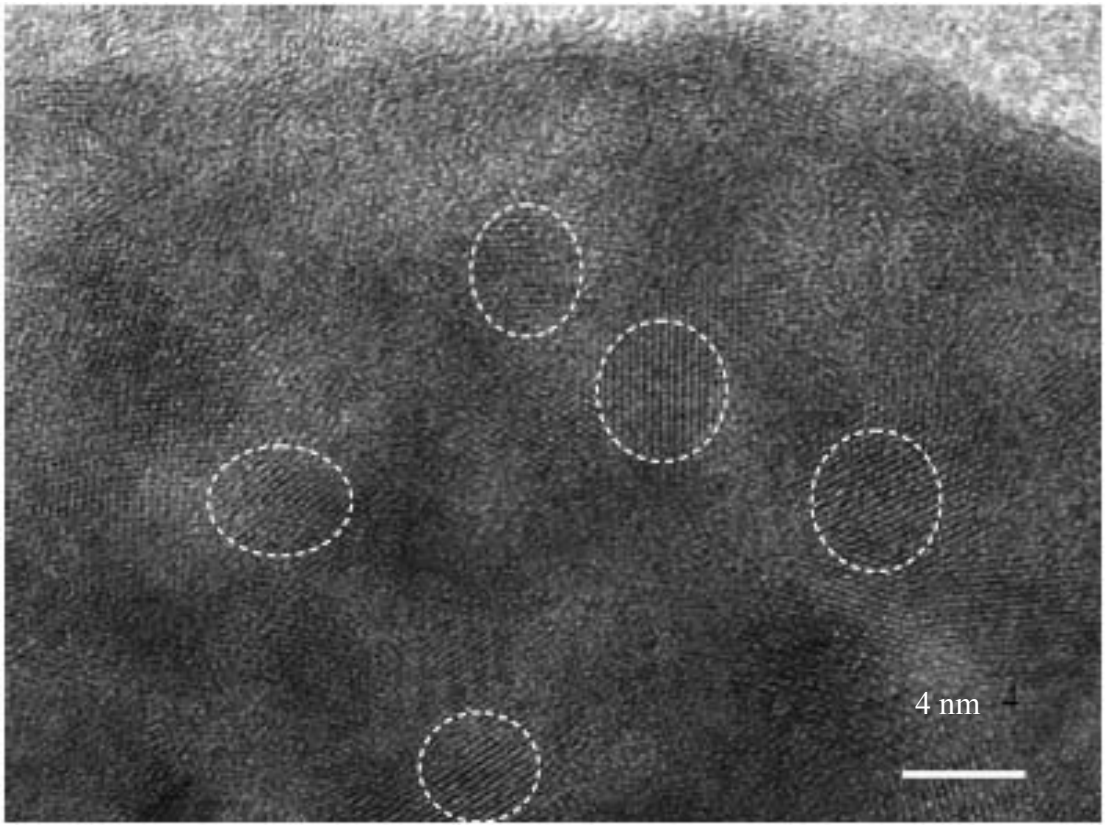

Figure 6-4 High Resolution TEM micrograph of nanospheres

The chemical analysis shows that only Zn and O were detected in the nanospheres prepared with this method, indicating that the possible product is ZnO and/or $Zn(OH)_2$ with associated water. The chemical composition of the synthesized nanospheres and the product were analyzed with TGA. The sample was heated up to 600^{o}C in the sample chamber at a heating rate of 10 ^{o}C/min. Figure 6-5 shows a total weight loss of 10.1% at 600^{o}C during the TGA experiment. The XRD analysis indicated that the product calcinated at this condition was pure ZnO. Therefore, the weight lost can be attributed only to the water lost from only hydrated ZnO or $Zn(OH)_2$. Based on the TGA analysis and TEM observations, the apparent formula of

the nanospheres before calcination should be $ZnO{\cdot}Zn(OH)_2$. The theoretical weight lost is 9.95% for $ZnO{\cdot}Zn(OH)_2$ which is very close to the experimental data of 10.1% from the TGA analysis. The overall TGA weight lost can then be explained by the following equation:

$$ZnO{\cdot}Zn(OH)_2 \text{ ------►} 2ZnO + H_2O \uparrow \qquad (6.1)$$

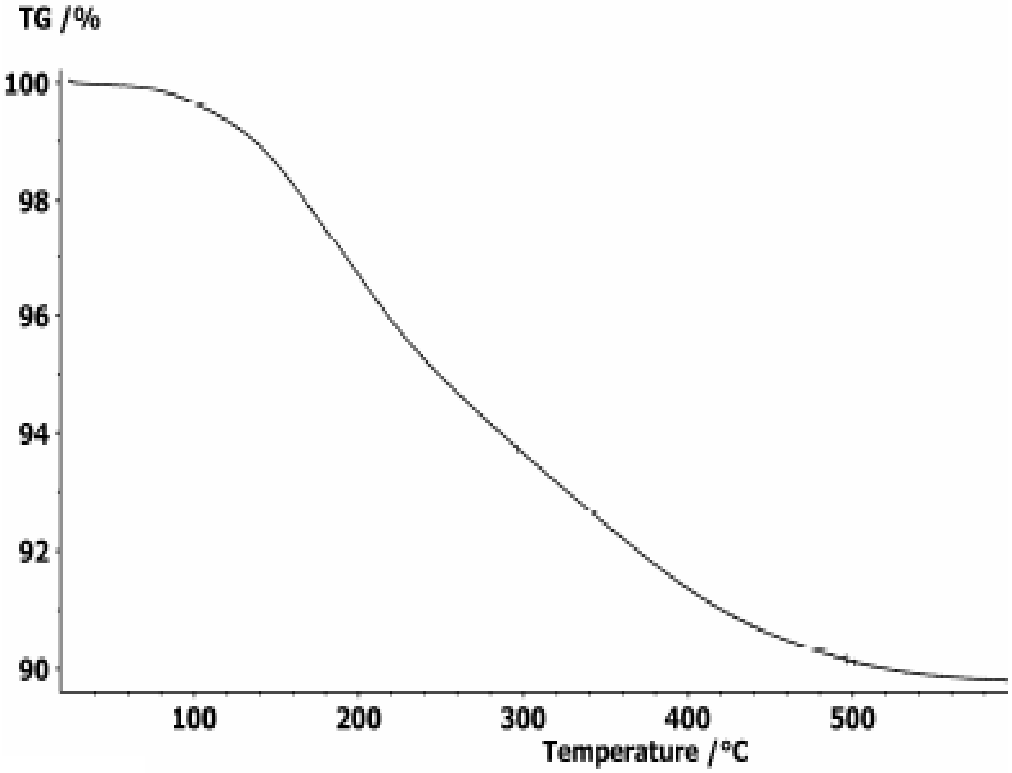

Figure 6-5 TGA analysis of the nanospheres

6.3.2 Product after calcination

The nanospheres were further calcined at a temperature of 600 ^{o}C for 30 minutes. Figure 6-6, which shows a SEM micrograph of calcined nanospheres, reveals that the spherical morphology was maintained after the calcination and then the diameter of the spheres shrank slightly after calcination. The surfaces of the calcined spheres were smoother than those of the as-prepared products. In addition, the surface of the spheres contained some holes, indicating that some of the spheres were possibly hollow.

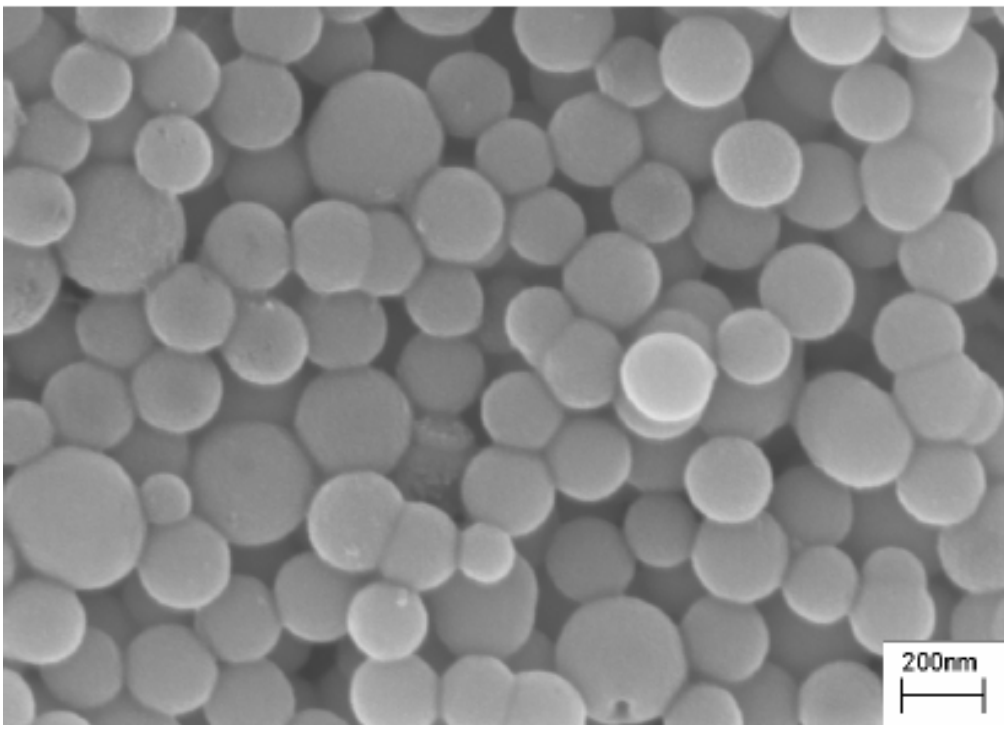

Figure 6-6 SEM micrograph of the calcinated nanospheres

Figure 6-7, illustrating the XRD spectra of the calcined nanospheres, shows that the crystallinity of the calcinated nanospheres was increased. The peaks from the spectra can be identified as diffraction from the wurtzite ZnO structure: the diffraction at 2θ= 31.8, 34.2, 36.2, and 56.5 corresponds to (100), (002), (101), and (110) planes, respectively. All the diffraction peaks agree well with those of the standard data (JCPDS No. 36-1451).

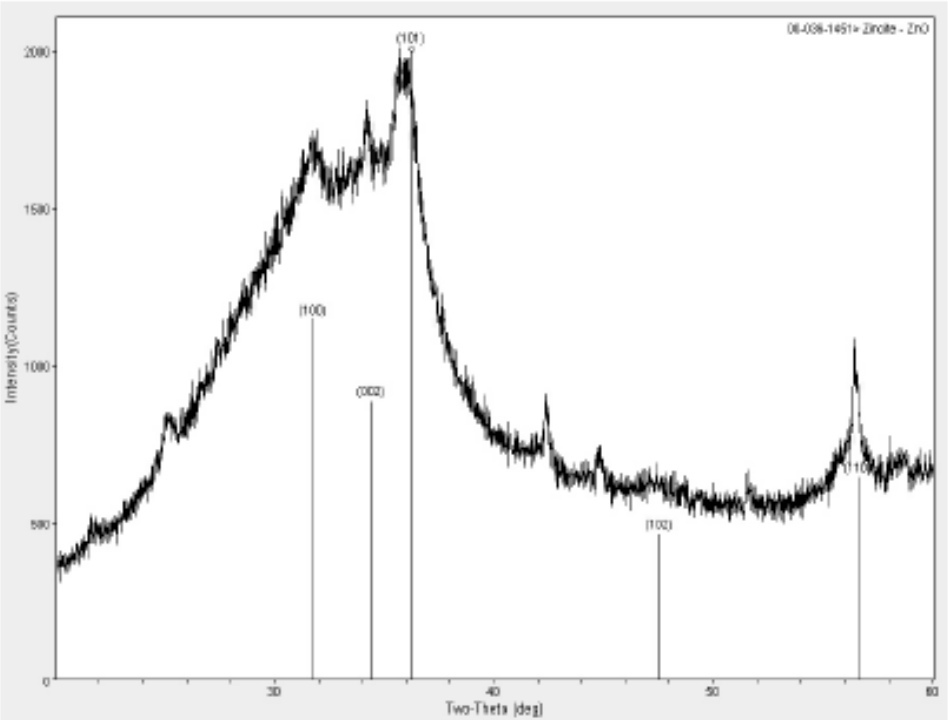

Figure 6-7 XRD spectrum of the calcinated spheres

A low magnification TEM image of the calcined nanospheres clearly shows that the hollowing in the nanospheres observed before calcination (Figure 6-3b) is further enhanced after calcination, as shown in Figure 6-8. A high resolution TEM

image in Figure 6-9 reveals that the sizes of the primary nanoparticles are similar if not the same.

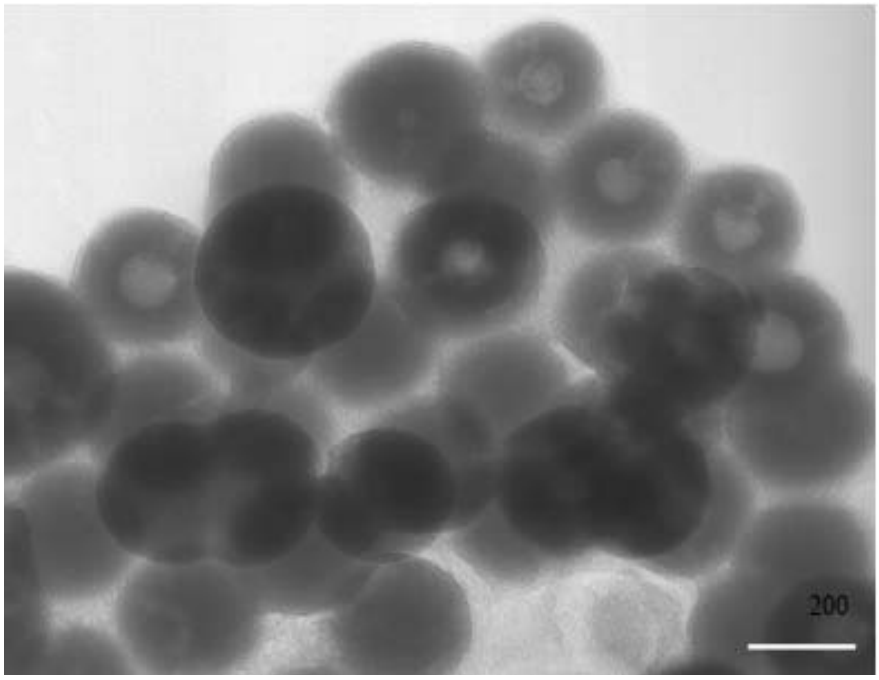

Figure 6-8 TEM micrograph of the calcinated nanospheres

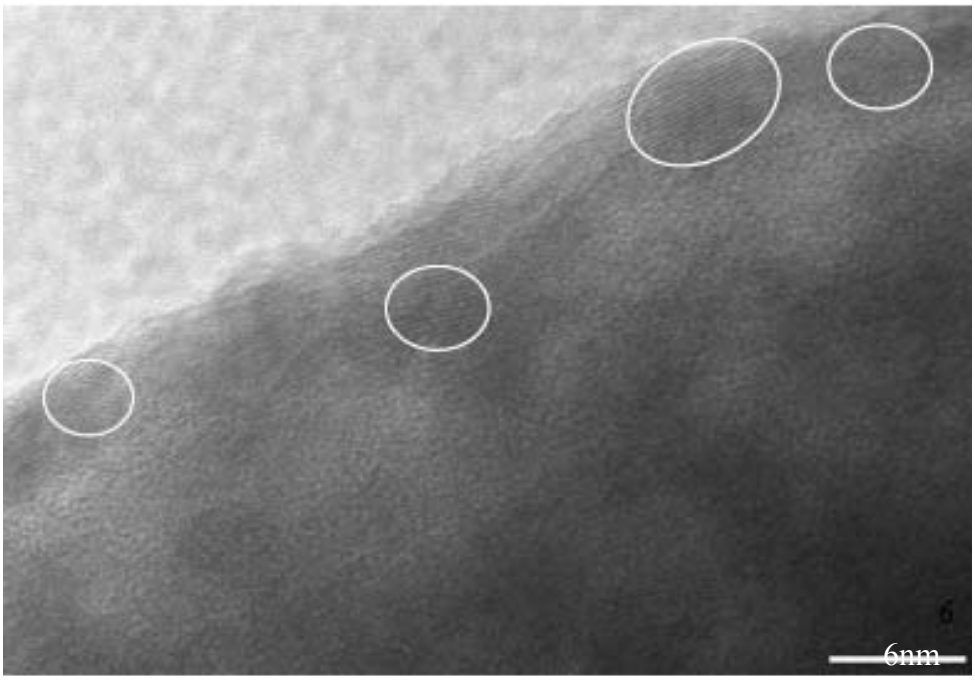

Figure 6-9 HRTEM micrograph of the calcinated nanospheres

6.3.3 Mechanism of nanosphere growth

The zinc nitrate and the HMT system has widely been used to synthesize ZnO nanorods [105, 178, 201]. However, the exact chemistry of this reaction, simply described in Chapter 5, is still not well understood yet. The key points of the reaction are that HMT first hydrolyzes to produce ammonia, and the ammonia then further hydrolyzes further to provide OH^- and NH_4^+. The OH^- ion will forms a complex compound with Zn^{2+}. The zinc compound then decomposes into ZnO under given reaction conditions. The chemistry of the entire process, which is relatively complex, is summarized below:

$$C_6H_{14}N_4 + 6\,H_2O \dashrightarrow 6CH_2O + 4\,NH_3 \quad (6.2)$$

$$NH_3 + H_2O \dashrightarrow NH_4^+ + OH^- \quad (6.3)$$

$$Zn^{2+} + 4OH^- \dashrightarrow Zn(OH)_4^{2-} \quad (6.4)$$

$$Zn(OH)_4^{2-} \dashrightarrow Zn(OH)_2 + 2OH^- \quad (6.5)$$

$$Zn(OH)_4^{2-} \dashrightarrow ZnO + H_2O + 2OH^- \quad (6.6)$$

In Chapter 5, the same materials were used to successfully synthesize ZnO nanorods. The only difference between the experiments in Chapter 5 and those here is that in the former, no agitation was applied during the preparation of the ZnO nanorods and here gentle magnetic stirring was applied. It can be concluded that the agitation must affect the morphology of particles since it disrupted the free diffusion of the building blocks to the growing nanocrystal. Therefore, both supersaturation and agitation play a crucial role in controlling the morphology of nanostructures.

It is generally accepted that crystal growth in solution is based on a dissolution-precipitation-ordering mechanism. Different precursors were first dissolved in solution to provide ions of the target crystal. Then nuclei are formed due to molecular collision. When the size of the nuclei grow larger than a certain critical

size, they become stable and atoms or molecules can diffuse to the nucleus surfaces and arrange themselves into ordered form. Banfield proposed a new crystal growth mechanism, oriented attachment theory. In this mechanism, nanoparticles that had formed from a solution and then attach to each other, shared a common crystallographic orientation and formed larger crystals, so that the total surface energy can be declined [199].

Based on the experimental observations and analyses, a mechanism of the growth of ZnO nanostructures of is proposed. In the nanorod experiment, it was observed that the surfaces of the nanorods were not microscopically smooth but instead, consisted of nanoparticles. These nanoparticles were similar to the primary particles, which aggregated to form the nanospheres. During the reaction, Zn^{2+} and OH^- ions formed the $Zn(OH)_2$ nanoparticles first. The $Zn(OH)_2$ nanoparticles tended to aggregate, reducing the total surface energy of the particles. Without any disturbance, the $Zn(OH)_2$ nanoparticles may aggregate in an ordered fashion. At the same time, under given experimental conditions, the $Zn(OH)_2$ can decomposed to form ZnO with well ordered single crystal nanorod morphology. However, in the case of gentle agitation, the $Zn(OH)_2$ nanoparticles did not aggregated in an orderly fashion. As a result, the $Zn(OH)_2$ nanoparticles randomly aggregated to form spheres, reducing the total energy. Due to the disordered structure, the individual crystal of $Zn(OH)_2$ in the nanospheres shown in Figure 6-1 aggregated to form a loose package The outside layer of the nanoparticles may decompose to ZnO, as in the process of

nanorod formation. However, the inner $Zn(OH)_2$ nanoparticles could not decompose easily. As a result, spheres with a composition of $ZnO{\cdot}Zn(OH)_2$ were formed.

When the $ZnO{\cdot}Zn(OH)_2$ nanospheres were calcined at a high temperature, the $Zn(OH)_2$ decomposed to ZnO and H_2O, and the water vapor diffused outwards through the pores between the loosely aggregated nanoparticles, resulting in a hollow structure of ZnO, as shown in Figure 6-8. Therefore, it can be concluded that the simple control of agitation can produce ZnO nanorods, nanospheres, and hollow nanospheres. While the nanorods usually consist of a single crystal structure, nanospheres are polycrystalline particles.

6.4 Conclusion

In this chapter, experimental conditions other than supersaturation on a nanostructure morphology were qualitatively investigated. Agitation was found to play as important as supersaturation in determining the morphology of nanostructure. With the same reaction system, nanorods and nanospheres could be obtained without or with agitation, respectively.

We have successfully demonstrated the effect of agitation on nanomaterial morphology. With the same reaction system used in Chapter 5, agitation could produce nanospheres ranging from 200 to 500 nm in diameter. SEM observations

further revealed that the nanospheres consisted of nanocrystals of less than 10 nm in size, and TEM showed that some nanospheres were hollow with various wall thicknesses. XRD and SAED analyses showed that the nanospheres consisted of polycrystalline nanoparticles, and their composition was determined to be $ZnO.Zn(OH)_2$. The structure of the nanospheres could become hollow after calcination because the $Zn(OH)_2$ could decompose into ZnO at high temperatures. The synthesis temperature could be as low as 65^{o}C. In the temperature range from 65 to 95 ^{o}C, the final products displayed no noticeable differences.

This chapter proposed a nanosphere formation mechanism. Findings showed that for nanorod growth with no agitation during the crystal growth, the $Zn(OH)_2$ nanocrystals as building blocks could diffuse to the surfaces of the growing nanostructures and oriented their crystallographic planes to form single crystal nanorod. The $Zn(OH)_2$ nanocrystals could decomposed to form ZnO nanorods. A agitation disrupted the ordered diffusion of the building blocks to the nanocrystal surface was broken. The unincorporated nanoparticles tended to form nanospheres, reducing the total system energy. While the $Zn(OH)_2$ nanocrystals on the outside surface were able to decompose to ZnO, those inside the nanospheres experience more difficulty dong so because the inside nanoparticles could not decompose easily. In addition, calcination can promote the conversion of the $ZnO{\cdot}Zn(OH)_2$ nanospheres to hollow ZnO nanospheres by calcination, representing a new method of synthesizing hollow spheres without any templates.

Chapter 7 : Conclusions and Recommendations for Future Work

7.1 Summary of the Present Work

Although 1D nanomaterials are important building blocks for nanotechnology, the controlled synthesis of nanostructures still remains as a challenge. To achieve this goal, we must understand the fundamentals control mechanism of the growth of nanostructures. This thesis has thoroughly investigated the growth phenomena of magnesium hydroxide sulfate hydrate nanobelts and ZnO nanorods in solution phase synthesis and the effect of supersaturation on 1D nanostructure growth. The supersaturation level in solution was successfully controlled by sparingly soluble carbonate salts. Magnesium hydroxide sulfate hydrate nanobelts were synthesized through sparingly soluble carbonate salts. The nanobelts synthesis provided not only direct evidence for the effect of supersaturation on nanobelts growth but also evidence that supersaturation could be controlled using sparingly soluble carbonate salts. This concept of supersaturation control by carbonate salts was further validated by extending it to the synthesis of ZnO nanorods in solution. Combining this analysis with SEM, XRD and GC analysis, we found that the growth of nanorods can be divided into three stages: the formation of nanosheets, the formation of "egg" seeds for nanorod growth, and the formation of large amount of ZnO nanorod. Other experimental conditions for nanorod growth were also examined. The findings show

that calcium carbonate acts as not only supersaturation control agents but also a heterogeneous nucleation site. A quantitative model provided a mechanism of nanorod growth in addition to a qualitative description of the nanostructure growth process. The model showed that supersaturation is not the only condition for controlling 1D nanostructure growth but other experimental conditions such as temperature and mixing should be considered in the preparation of 1D nanostructure.

This thesis work has demonstrated a significant concept, the synthesis of nanomaterial by controlling supersaturation through sparingly soluble salts. With a more thorough understanding of this process, we can achieve an important goal in nanoscience and nanotechnology: the control of the composition, the structure, and the dimensions of nanomaterials. With all its advantages, the solution phase synthesis of nanomaterials will become more and more attractive. Through the incorporation of chemical engineering practice, the large scale production of nanomaterials is within the visible horizon. Based on these finding, this thesis will suggest directions for future research that, if pursued, should result in significant advances in nanoscale science and engineering.

The quantitative model based on kinetic theory was developed to show the relationship between supersaturation and ZnO nanorod growth. The Zn^{2+} concentration in the solution could be described with first order reaction mechanism. The growth rate of the nanorods increased with increasing temperature. The higher

the temperature is, the faster the lengths of the nanorods approach to a constant. This could be explained by the hydrolysis rate of HMT. At high temperatures, HMT decomposed rapidly and provided a high concentration of OH^- resulting in a high supersaturation, which is beneficial to nucleation, but not to crystal growth.

We examined the process parameters other than the effect of supersaturation on the control of morphology and found that agitation significantly affected morphology, as it produced nanospheres when it was applied to the same reaction system used for ZnO nanorod synthesis. Agitation broke down the free diffusion of building blocks to the surfaces of growing nanocrystals. To reduce the total system energy, the building blocks postulated to be $Zn(OH)_2$ aggregated to form nanospheres. When the nanospheres formed, the building blocks inside the nanospheres could not decompose easily under given experimental conditions. However, under high temperature calcination conditions, decomposition took place. Therefore, these nanospheres could be further made into hollow structures.

7.2 Recommendations for Future Work

7.2.1 Understanding and control of nanocrystal growth

Due to the novel properties found in the nanoscale region, the fields of nanoscience and nanotechnology have stirred tremendous interest of both academia

and industry n. In his famous speech: “there is plenty of room at the bottom”, Nobel Laurel Richard Feynman described a picture to “arrange the atoms the way we want” from a scientist’s perspective. From an engineer’s point of view, controlling the growth of nanocrystals in the way we want still poses a great challenge.

Though the simple kinetic model is presented in the research, this thesis has captured the essence of the growth of ZnO nanorod. However, the details of such growth remain elusive. We know that traditionally nanostructures have traditionally been developed through a mechanism in which atoms are added to the crystal one by one. However, the process can be either diffusion controlled in which the diffusion of atoms to the crystal surface is the limiting step, or reaction controlled in which the incorporation of atoms into the crystal lattice is the limiting step. Another proposed theory, the oriented attachment theory [199, 200, 219-221], claims that nanocrystals are formed first and these nanocrystals can re-arrange themselves in such a fashion that they form a single crystal. In ZnO nanorod growth, an oriented mechanism could be applied based on the experimental observations as shown in Figure 6-1 and Figure 7-1. The SEM image clearly shows that the nanorods grow from an aggregation of smaller primary nanocrystals. The TEM micrograph of nanospheres revealed that they consist of similar nanocrystals. This growth mechanism can be verified in the following ways:

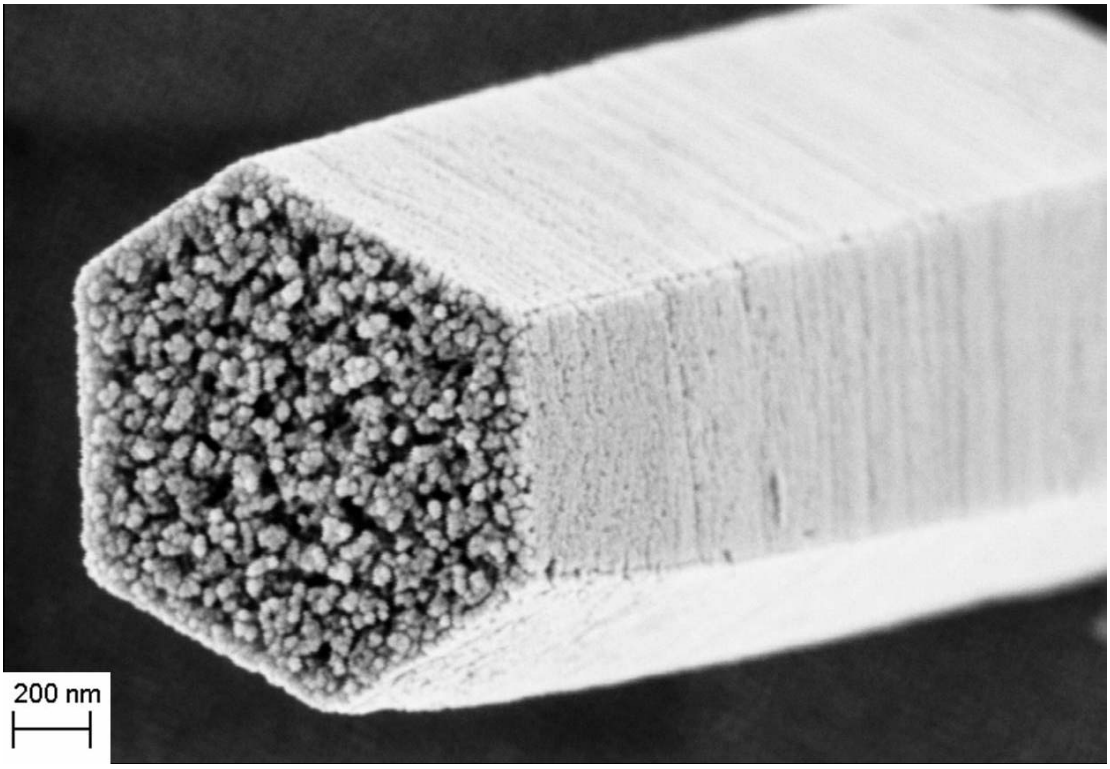

Figure 7-1 SEM micrograph of the growth of nanorods from particle aggregation

- By determining the concentration of $Zn2^{+}$ in the reaction solution through ICP
- By using UV-vis absorption to determine the relative nanocrystal concentration at different time.
- By ascertaining the amount of nanorods through the following methods
  - UV-vis absorption around 380nm.
  - XRD

Once the above information is available, we can test the proposed oriented attachment mechanism. The consumption of nanocrystals should be equal to the increase in the mass of the nanorods. In addition to the experiment investigation, molecular modeling of the process of the incorporation of nanocrystals into nanorods process might provide some insight into the growth process.

REFERENCES

1. Bakshi, D. and W. Walrond, *Paper and pigment Trends*. 2006, The Pigment Course;Imerys, Sandersville, GA: Sandersville, GA

2. Brown, R., *Particle Size, Shape, and Structure of Paper Fillers and Their Effect on Paper Properties.* Paper Technology, 1998. **39**(2): p. 44-48.

3. Yoon, S. and Y. Deng, *Starch-fatty complex modified filler for papermaking.* Tappi Journal, 2006. **5**(9).

4. Yoon, S. and Y. Deng, *Clay-starch composites and their application in papermaking.* Journal of Applied Polymer Science, 2006. **100**(2): p. 1032.

5. Mathur, V.K. *Novel silicate "fibrous fillers" and their application in paper*. 2004. Atlanta, GA, United States: TAPPI Press, Atlanta, GA 30348-5113, United States.

6. Alivisatos, A.P., *Semiconductor clusters, nanocrystals, and quantum dots.* Science, 1996. **271**(5251): p. 933.

7. Michalet, X., F.F. Pinaud, L.A. Bentolila, J.M. Tsay, S. Doose, J.J. Li, G. Sundaresan, A.M. Wu, S.S. Gambhir and S. Weiss, *Quantum dots for live cells, in vivo imaging, and diagnostics.* Science, 2005. **307**(5709): p. 538-544.

8. Dubertret, B., P. Skourides, D.J. Norris, V. Noireaux, A.H. Brivanlou and A. Libchaber, *In vivo imaging of quantum dots encapsulated in phospholipid micelles.* Science, 2002. **298**(5599): p. 1759-1762.

9. Aspnes, D.E., *Optical properties of thin films* Thin Solid Films, 1982. **89**(3): p. 249-262.

10. Francois, J.C., Y. Massiani, P. Gravier, J. Grimblot and L. Gengembre, *Characterization and optical properties of thin films formed on TiN coating during electrochemical treatments* Thin Solid Films, 1993. **223**(2): p. 223-229.

11. Stratmann, M., R. Feser and A. Leng, *Corrosion protection by organic films* Electrochimica Acta, 1994. **39**(8-9): p. 1207-1214.

12. Gray, J.E. and B. Luan, *Protective coatings on magnesium and its alloys - a critical review.* Journal of Alloys and Compounds, 2002. **336**(1-2): p. 88-113.

13. Dimitrakopoulos, C.D. and P.R.L. Malenfant, *Organic thin film transistors for large area electronics.* Advanced Materials, 2002. **14**(2): p. 99-+.

14. Scherf, U. and E.J.W. List, *Semiconducting polyfluorenes - Towards reliable structure-property relationships.* Advanced Materials, 2002. **14**(7): p. 477-+.

15. Wolf, S.A., D.D. Awschalom, R.A. Buhrman, J.M. Daughton, S. von Molnar, M.L. Roukes, A.Y. Chtchelkanova and D.M. Treger, *Spintronics: A spin-based electronics vision for the future.* Science, 2001. **294**(5546): p. 1488-1495.

16. Chen, H., X. Kou, Z. Yang, W. Ni and J. Wang, *Shape- and size-dependent refractive index sensitivity of gold nanoparticles.* Langmuir, 2008. **24**(10): p. 5233-5237.

17. Sun, Y., L. Zhuang, J. Lu, X. Hong and P. Liu, *Collapse in crystalline structure and decline in catalytic activity of Pt nanoparticles on reducing particle size to 1 nm.* Journal of the American Chemical Society, 2007. **129**(50): p. 15465-15467.

18. Lucas, M., W. Mai, R. Yang, Z.L. Wang and E. Riedo, *Aspect ratio dependence of the elastic properties of ZnO nanobelts.* Nano Letters, 2007. **7**(5): p. 1314-1317.

19. Pacifico, J., D. Gomez and P. Mulvaney, *A simple route to tunable two-dimensional arrays of quantum dots.* Advanced Materials, 2005. **17**(4): p. 415-418.

20. Bruchez, M., M. Moronne, P. Gin, S. Weiss and A.P. Alivisatos, *Semiconductor nanocrystals as fluorescent biological labels.* Science, 1998. **281**(5385): p. 2013-2016.

21. Buffat, P. and J.P. Borel, *Size effect on melting temperature of gold particles* Physical Review A, 1976. **13**(6): p. 2287-2298.

22. Goldstein, A.N., C.M. Echer and A.P. Alivisatos, *Melting semiconductor nanocrystals* Science, 1992. **256**(5062): p. 1425-1427.

23. Ichihashi, S.L.T., *Single-shell carbon nanotubes of 1-nm diameter.* Nature, 1993. **363**: p. 603.

24. Lijima, S., *Helical microtubules of graphitic carbon.* Nature, 1991. **354**(56).

25. al, R.E.S.e., *Crystalline ropes of metallic carbon nanotubes.* Science, 1996. **273**(5274): p. 483.

26. Baughman, R.H., A.A. Zakhidov and W.A. de Heer, *Carbon nanotubes - the route toward applications.* Science, 2002. **297**(5582): p. 787-792.

27. Morales, A.M. and C.M. Lieber, *A laser ablation method for the synthesis of crystalline semiconductor nanowires.* Science, 1998. **279**: p. 208.

28. Hu, J.T., T.W. Odom and C.M. Lieber, *Chemistry and physics in one dimension: Synthesis and properties of nanowires and nanotubes.* Accounts of Chemical Research, 1999. **32**(5): p. 435-445.

29. Duan, X. and C.M. Lieber, *General synthesis of compound semiconductor nanowires.* Advanced Materials, 2000. **12**(4): p. 298.

30. Holmes, J.D., K.P. Johnston, R.C. Doty and B.A. Korgel, *Control of thickness and orientation of solution-grown silicon nanowires.* Science, 2000. **287**(5457): p. 1471-1473.

31. Murphy, C.J. and N.R. Jana, *Controlling the aspect ratio of inorganic nanorods and nanowires.* Advanced Materials, 2002. **14**(1): p. 80-82.

32. Li, Y.D., H.W. Liao, Y. Ding, Y.T. Qian, L. Yang and G.E. Zhou, *Nonaqueous synthesis of CdS nanorod semiconductor.* Chemistry of Materials, 1998. **10**(9): p. 2301-+.

33. Patzke, G.R., F. Krumeich and R. Nesper, *Oxidic nanotubes and nanorods - Anisotropic modules for a future nanotechnology.* Angewandte Chemie-International Edition, 2002. **41**(14): p. 2446-2461.

34. Zheng Wei, P., D. Zu Rong and W. Zhong Lin, *Nanobelts of semiconducting oxides.* Science, 2001. **291**(5510): p. 1947-9.

35. Ma, C., D. Moore, J. Li and Z.L. Wang, *Nanobelts, nanocombs, and nanowindmills of wurtzite ZnS.* Advanced Materials, 2003. **15**(3): p. 228-+.

36. Schider, G., J.R. Krenn, W. Gotschy, B. Lamprecht, H. Ditlbacher, A. Leitner and F.R. Aussenegg, *Optical properties of Ag and Au nanowire gratings.* Journal of Applied Physics, 2001. **90**(8): p. 3825-3830.

37. Kataura, H., Y. Kumazawa, Y. Maniwa, I. Umezu, S. Suzuki, Y. Ohtsuka and Y. Achiba, *Optical properties of single-wall carbon nanotubes.* Synthetic Metals, 1999. **103**(1-3): p. 2555-2558.

38. Odom, T.W., J.L. Huang, P. Kim and C.M. Lieber, *Atomic structure and electronic properties of single-walled carbon nanotubes.* Nature, 1998. **391**(6662): p. 62-64.

39. Li, Q.H., Q. Wan, Y.X. Liang and T.H. Wang, *Electronic transport through individual ZnO nanowires.* Applied Physics Letters, 2004. **84**(22): p. 4556-4558.

40. Zhao, X.Y., C.M. Wei, L. Yang and M.Y. Chou, *Quantum confinement and electronic properties of silicon nanowires.* Physical Review Letters, 2004. **92**(23).

41. Wong, E.W., P.E. Sheehan and C.M. Lieber, *Nanobeam mechanics: Elasticity, strength, and toughness of nanorods and nanotubes.* Science, 1997. **277**(5334): p. 1971-1975.

42. Wu, B., A. Heidelberg and J.J. Boland, *Mechanical properties of ultrahigh-strength gold nanowires.* Nature Materials, 2005. **4**(7): p. 525-529.

43. Qian, D., E.C. Dickey, R. Andrews and T. Rantell, *Load transfer and deformation mechanisms in carbon nanotube-polystyrene composites.* Applied Physics Letters, 2000. **76**(20): p. 2868-2870.

44. Mao, S.X., M.H. Zhao and Z.L. Wang, *Nanoscale mechanical behavior of individual semiconducting nanobelts.* Applied Physics Letters, 2003. **83**(5): p. 993-995.

45. Yu, M.F., O. Lourie, M.J. Dyer, K. Moloni, T.F. Kelly and R.S. Ruoff, *Strength and breaking mechanism of multiwalled carbon nanotubes under tensile load.* Science, 2000. **287**(5453): p. 637-640.

46. Yu, M.F., B.S. Files, S. Arepalli and R.S. Ruoff, *Tensile loading of ropes of single wall carbon nanotubes and their mechanical properties.* Physical Review Letters, 2000. **84**(24): p. 5552-5555.

47. Sander J. Tans, M.H.d., Hongjie Dai, Andreas Thess, Richard E. Smalley, L.J. Geerligs & Cees Dekker, *Individual single-wall carbon nanotubes as quantum wires.* Nature, 1997. **386**: p. 474.

48. Ebbesen, T.W., H.J. Lezec, H. Hiura, J.W. Bennett, H.F. Ghaemi and T. Thio, *Electrical conductivity of individual carbon nanotubes.* NATURE, 1996. **382**(6586): p. 54-56.

49. Heo, Y.W., L.C. Tien, D.P. Norton, B.S. Kang, F. Ren, B.P. Gila and S.J. Pearton, *Electrical transport properties of single ZnO nanorods.* Applied Physics Letters, 2004. **85**(11): p. 2002-2004.

50. Goldberger, J., D.J. Sirbuly, M. Law and P. Yang, *ZnO nanowire transistors.* Journal of Physical Chemistry B, 2005. **109**(1): p. 9-14.

51. Guzelian, A.A., J.E.B. Katari, A.V. Kadavanich, U. Banin, K. Hamad, E. Juban, A.P. Alivisatos, R.H. Wolters, C.C. Arnold and J.R. Heath, *Synthesis of size-selected, surface-passivated InP nanocrystals.* Journal of Physical Chemistry, 1996. **100**(17): p. 7212-7219.

52. Peng, X.G., J. Wickham and A.P. Alivisatos, *Kinetics of II-VI and III-V colloidal semiconductor nanocrystal growth: "Focusing" of size distributions.* Journal of the American Chemical Society, 1998. **120**(21): p. 5343-5344.

53. Klimov, V.I., A.A. Mikhailovsky, S. Xu, A. Malko, J.A. Hollingsworth, C.A. Leatherdale, H.J. Eisler and M.G. Bawendi, *Optical gain and stimulated emission in nanocrystal quantum dots.* Science, 2000. **290**(5490): p. 314-317.

54. Nirmal, M., B.O. Dabbousi, M.G. Bawendi, J.J. Macklin, J.K. Trautman, T.D. Harris and L.E. Brus, *Fluorescence intermittency in single cadmium selenide nanocrystals.* NATURE, 1996. **383**(6603): p. 802-804.

55. Yang, P.D., H.Q. Yan, S. Mao, R. Russo, J. Johnson, R. Saykally, N. Morris, J. Pham, R.R. He and H.J. Choi, *Controlled growth of ZnO nanowires and their optical properties.* Advanced Functional Materials, 2002. **12**(5): p. 323-331.

56. Treacy, M.M.J., T.W. Ebbesen and J.M. Gibson, *Exceptionally high Young's modulus observed for individual carbon nanotubes.* NATURE, 1996. **381**(6584): p. 678-680.

57. Bacon, R., *Growth structure and properties of graphite whiskers* Journal of Applied Physics, 1960. **31**(2): p. 283-290.

58. Jia, Q.M., M. Zheng, C.Z. Xu and H.X. Chen, *The mechanical properties and tribological behavior of epoxy resin composites modified by different shape nanofillers.* Polymers for Advanced Technologies, 2006. **17**(3): p. 168-173.

59. Henglein, A., *Physicochemical properties of small metal particles in solution -microelectode reactions, chemisorption, composite metal particles, and the atom-to-metal transition* Journal of Physical Chemistry, 1993. **97**(21): p. 5457-5471.

60. Wong, S.S., E. Joselevich, A.T. Woolley, C.L. Cheung and C.M. Lieber, *Covalently functionalized nanotubes as nanometre-sized probes in chemistry and biology.* NATURE, 1998. **394**(6688): p. 52-55.

61. Shipway, A.N., E. Katz and I. Willner, *Nanoparticle arrays on surfaces for electronic, optical, and sensor applications.* ChemPhysChem, 2000. **1**(1): p. 18-52.

62. Kamat, P.V., *Photophysical, photochemical and photocatalytic aspects of metal nanoparticles.* Journal of Physical Chemistry B, 2002. **106**(32): p. 7729-7744.

63. Burda, C., X.B. Chen, R. Narayanan and M.A. El-Sayed, *Chemistry and properties of nanocrystals of different shapes.* Chemical Reviews, 2005. **105**(4): p. 1025-1102.

64. Narayanan, R. and M.A. El-Sayed, *Shape-dependent catalytic activity of platinum nanoparticles in colloidal solution.* Nano Letters, 2004. **4**(7): p. 1343-1348.

65. Bell, A.T., *The impact of nanoscience on heterogeneous catalysis.* Science, 2003. **299**(5613): p. 1688-1691.

66. Ge, J., W. Xing, X. Xue, C. Liu, T. Lu and J. Liao, *Controllable synthesis of Pd nanocatalysts for Direct Formic Acid Fuel Cell (DFAFC) application:*

From Pd hollow nanospheres to Pd nanoparticles. Journal of Physical Chemistry C, 2007. **111**(46): p. 17305-17310.

67. Miao, S., C. Zhang, Z. Liu, B. Han, Y. Xie, S. Ding and Z. Yang, *Highly efficient nanocatalysts supported on hollow polymer nanospheres: Synthesis, characterization, and applications.* Journal of Physical Chemistry C, 2008. **112**(3): p. 774-780.

68. Li, J. and H.C. Zeng, *Preparation of monodisperse Au/TiO2 nanocatalysts via self-assembly.* Chemistry of Materials, 2006. **18**(18): p. 4270-4277.

69. Shen, S., K. Hidajat, L.E. Yu and S. Kawi, *Simple Hydrothermal Synthesis of Nanostructured and Nanorod Zn-Al Complex Oxides as Novel Nanocatalysts.* Advanced Materials, 2004. **16**(6): p. 541-545.

70. Sanchez, A., S. Abbet, U. Heiz, W.D. Schneider, H. Hakkinen, R.N. Barnett and U. Landman, *When gold is not noble: Nanoscale gold catalysts.* Journal of Physical Chemistry A, 1999. **103**(48): p. 9573-9578.

71. Bognitzki, M., W. Czado, T. Frese, A. Schaper, M. Hellwig, M. Steinhart, A. Greiner and J.H. Wendorff, *Nanostructured fibers via electrospinning.* Advanced Materials, 2001. **13**(1): p. 70-+.

72. Li, D. and Y.N. Xia, *Fabrication of titania nanofibers by electrospinning.* Nano Letters, 2003. **3**(4): p. 555-560.

73. Caruso, F., R.A. Caruso and H. Mohwald, *Nanoengineering of inorganic and hybrid hollow spheres by colloidal templating.* Science, 1998. **282**(5391): p. 1111-1114.

74. Martin, C.R., *Nanomaterials a membrane based synthetic approach* Science, 1994. **266**(5193): p. 1961-1966.

75. Thurn-Albrecht, T., J. Schotter, C.A. Kastle, N. Emley, T. Shibauchi, L. Krusin-Elbaum, K. Guarini, C.T. Black, M.T. Tuominen and T.P. Russell, *Ultrahigh-density nanowire arrays grown in self-assembled diblock copolymer templates.* Science, 2000. **290**(5499): p. 2126-2129.

76. Alivisatos, A.P., K.P. Johnsson, X.G. Peng, T.E. Wilson, C.J. Loweth, M.P. Bruchez and P.G. Schultz, *Organization of 'nanocrystal molecules' using DNA.* NATURE, 1996. **382**(6592): p. 609-611.

77. Li, Z. and Y.M. Du, *Biomimic synthesis of CdS nanoparticles with enhanced luminescence.* Materials Letters, 2003. **57**(16-17): p. 2480-2484.

78. Sommer, A.P. and R.P. Franke, *Biomimicry patterning with nanosphere suspensions.* Nano Letters, 2003. **3**(5): p. 573-575.

79. Park, M., C. Harrison, P.M. Chaikin, R.A. Register and D.H. Adamson, *Block copolymer lithography: Periodic arrays of similar to 10(11) holes in 1 square centimeter.* Science, 1997. **276**(5317): p. 1401-1404.

80. Piner, R.D., J. Zhu, F. Xu, S.H. Hong and C.A. Mirkin, *"Dip-pen" nanolithography.* Science, 1999. **283**(5402): p. 661-663.

81. Chou, S.Y., P.R. Krauss and P.J. Renstrom, *Imprint lithography with 25-nanometer resolution.* Science, 1996. **272**(5258): p. 85-87.

82. Chou, S.Y., P.R. Krauss and P.J. Renstrom, *Nanoimprint lithography.* Journal of Vacuum Science & Technology B, 1996. **14**(6): p. 4129-4133.

83. Haynes, C.L. and R.P. Van Duyne, *Nanosphere lithography: A versatile nanofabrication tool for studies of size-dependent nanoparticle optics.* Journal of Physical Chemistry B, 2001. **105**(24): p. 5599-5611.

84. Xia, Y.N. and G.M. Whitesides, *Soft lithography.* Annual Review of Materials Science, 1998. **28**: p. 153-184.

85. Shu-Hong Yu, M.A., Helmut Co1lfen, and Jurgen Hartmann, *Growth and Self-Assembly of BaCrO4 and BaSO4 Nanofibers toward Hierarchical and Repetitive Superstructures by Polymer-Controlled Mineralization Reactions* Nano Letters, 2003. **3**(3): p. 379.

86. Ye, C., X. Fang, Y. Hao, X. Teng and L. Zhang, *Zinc oxide nanostructures: Morphology derivation and evolution.* Journal of Physical Chemistry B, 2005. **109**(42): p. 19758-19765.

87. Choy, K.L., *Chemical vapour deposition of coatings.* Progress in Materials Science, 2003. **48**(2): p. 57-170.

88. Dai, H.J., *Carbon nanotubes: Synthesis, integration, and properties.* Accounts of Chemical Research, 2002. **35**(12): p. 1035-1044.

89. Xia, Y.N., P.D. Yang, Y.G. Sun, Y.Y. Wu, B. Mayers, B. Gates, Y.D. Yin, F. Kim and Y.Q. Yan, *One-dimensional nanostructures: Synthesis, characterization, and applications.* Advanced Materials, 2003. **15**(5): p. 353-389.

90. Wagner, R.S. and W.C. Ellis, *VAPOR-LIQUID-SOLID MECHANISM OF SINGLE CRYSTAL GROWTH (NEW METHOD GROWTH CATALYSIS FROM IMPURITY WHISKER EPITAXIAL + LARGE CRYSTALS SI E).* Applied Physics Letters, 1964. **4**(5): p. 89-&.

91. Helveg, S., C. Lopez-cartes, J. Sehested, P. Hansen, B. Clausen, J. Rostrup-Nielsen, F. Abild-Pedersen and J. Nerskov, *Atomic-scale imaging of carbon nanofibre growth.* Nature, 2004. **427**(29): p. 426.

92. Meister, S., H.L. Peng, K. McIlwrath, K. Jarausch, X.F. Zhang and Y. Cui, *Synthesis and characterization of phase-change nanowires.* Nano Letters, 2006. **6**(7): p. 1514-1517.

93. Wu, Y. and P. Yang, *Direct Observation of Vapor-Liquid-Solid Nanowire Growth.* J AM Chem Soc, 2001. **123**(13): p. 3165.

94. Umar, A., S.H. Kim, Y.S. Lee, K.S. Nahm and Y.B. Hahn, *Catalyst-free large-quantity synthesis of ZnO nanorods by a vapor-solid growth mechanism: Structural and optical properties.* Journal of Crystal Growth, 2005. **282**(1-2): p. 131-136.

95. Sekar, A., S.H. Kim, A. Umar and Y.B. Hahn, *Catalyst-free synthesis of ZnO nanowires on Si by oxidation of Zn powders.* Journal of Crystal Growth, 2005. **277**(1-4): p. 471-478.

96. Yang, P. and C.M. Lieber, *Nanorod-superconductor Composites: A pathway to materials with High Critical Current Densities.* Science, 1996. **273**(5283): p. 1836.

97. Park, W.I., D.H. Kim, S.W. Jung and G.C. Yi, *Metalorganic vapor-phase epitaxial growth of vertically well-aligned ZnO nanorods.* Applied Physics Letters, 2002. **80**(22): p. 4232-4234.

98. Liu, Z.Q., D.H. Zhang, S. Han, C. Li, T. Tang, W. Jin, X.L. Liu, B. Lei and C.W. Zhou, *Laser ablation synthesis and electron transport studies of tin oxide nanowires.* Advanced Materials, 2003. **15**(20): p. 1754.

99. Tian, Z.R.R., J.A. Voigt, J. Liu, B. McKenzie and H.F. Xu, *Large oriented arrays and continuous films of TiO2-based nanotubes.* Journal of the American Chemical Society, 2003. **125**(41): p. 12384-12385.

100. Cozzoli, P.D., A. Kornowski and H. Weller, *Low-temperature synthesis of soluble and processable organic-capped anatase TiO2 nanorods.* Journal of the American Chemical Society, 2003. **125**(47): p. 14539-14548.

101. Nelson, K. and D. Yulin. *Synthesis of hollow TiO2: Towards a fundamental understanding of the relationship between filler morphology and performance*. 2006. Atlanta, GA, United States: TAPPI Press, Norcross, GA 30092, United States.

102. Lian, G. and C. Zhitao, *A facile route to ZnO nanorod arrays using wet chemical method.* Journal of Crystal Growth, 2006. **293**(2): p. 522-7.

103. Cheng, J.P., X.B. Zhang and Z.Q. Luo, *Aligned ZnO nanorod arrays fabricated on Si substrate by solution deposition.* Physica E-Low-Dimensional Systems & Nanostructures, 2006. **31**(2): p. 235-239.

104. Tak, Y. and K.J. Yong, *Controlled growth of well-aligned ZnO nanorod array using a novel solution method.* Journal of Physical Chemistry B, 2005. **109**(41): p. 19263-19269.

105. Weintraub, B., Y.L. Deng and Z.L. Wang, *Position-controlled seedless growth of ZnO nanorod arrays on a polymer substrate via wet chemical synthesis.* Journal of Physical Chemistry C, 2007. **111**(28): p. 10162-5.

106. Rakovich, Y.P., Y. Volkov, S. Sapra, A.S. Susha, M. Doblinger, J.F. Donegan and A.L. Rogach, *CdTe nanowire networks: Fast self-assembly in solution, internal structure, and optical properties.* Journal of Physical Chemistry C, 2007. **111**(51): p. 18927-18931.

107. Wang, Z.Y., J. Hu, A.P. Suryavanshi, K. Yum and M.F. Yu, *Voltage generation from individual BaTiO3 nanowires under periodic tensile mechanical load.* Nano Letters, 2007. **7**(10): p. 2966-2969.

108. Yu, J.Y., S.L. Tang, R.L. Wang, Y.G. Shi, B. Nie, L. Zhai, X.K. Zhang and Y.W. Du, *Synthesis of single-crystalline barium dititanate nanobelts.* Crystal Growth & Design, 2008. **8**(5): p. 1481-1483.

109. Zhou, Z., Q. Sun, Z. Hu and Y. Deng, *Nanobelt formation of magnesium hydroxide sulfate hydrate via a facile hydrothermal process.* J. Phys. Chem. B, 2006. **110**(27): p. 13387.

110. Yonezawa, T., S. Onoue and N. Kimizuka, *Preparation of highly positively charged silver nanoballs and their stability.* Langmuir, 2000. **16**(12): p. 5218-5220.

111. Sondi, I., D.V. Goia and E. Matijevic, *Preparation of highly concentrated stable dispersions of uniform silver nanoparticles.* Journal of Colloid and Interface Science, 2003. **260**(1): p. 75-81.

112. Han, M.Y., C.H. Quek, W. Huang, C.H. Chew and L.M. Gan, *A simple and effective chemical route for the preparation of uniform nonaqueous gold colloids.* Chemistry of Materials, 1999. **11**(4): p. 1144-1147.

113. Cameron, N.S., M.K. Corbierre and A. Eisenberg. *1998 E.W.R. Steacie Award Lecture Asymmetric amphiphilic block copolymers in solution: a morphological wonderland*. 1999.

114. John, V.T., B. Simmons, G.L. McPherson and A. Bose, *Recent developments in materials synthesis in surfactant systems.* Current Opinion in Colloid & Interface Science, 2002. **7**(5-6): p. 288-295.

115. Pileni, M.P., *REVERSE MICELLES AS MICROREACTORS.* Journal of Physical Chemistry, 1993. **97**(27): p. 6961-6973.

116. Zarur, A.J. and J.Y. Ying, *Reverse microemulsion synthesis of nanostructured complex oxides for catalytic combustion.* NATURE, 2000. **403**(6765): p. 65-67.

117. Santra, S., R. Tapec, N. Theodoropoulou, J. Dobson, A. Hebard and W.H. Tan, *Synthesis and characterization of silica-coated iron oxide nanoparticles in microemulsion: The effect of nonionic surfactants.* Langmuir, 2001. **17**(10): p. 2900-2906.

118. Reverchon, E., *Supercritical antisolvent precipitation of micro- and nano-particles.* Journal of Supercritical Fluids, 1999. **15**(1): p. 1-21.

119. Ji, M., X.Y. Chen, C.M. Wai and J.L. Fulton, *Synthesizing and dispersing silver nanoparticles in a water-in-supercritical carbon dioxide microemulsion.* Journal of the American Chemical Society, 1999. **121**(11): p. 2631-2632.

120. Liu, B. and H.C. Zeng, *Hydrothermal synthesis of ZnO nanorods in the diameter regime of 50 nm.* Journal of the American Chemical Society, 2003. **125**(15): p. 4430-4431.

121. Zhang, H., D.R. Yang, D.S. Li, X.Y. Ma, S.Z. Li and D.L. Que, *Controllable growth of ZnO microcrystals by a capping-molecule-assisted hydrothermal process.* Crystal Growth & Design, 2005. **5**(2): p. 547-550.

122. Cheng, B. and E.T. Samulski, *Hydrothermal synthesis of one-dimensional ZnO nanostructures with different aspect ratios.* Chemical Communications, 2004(8): p. 986-987.

123. Zhang, H., L.P. Wang, H.M. Xiong, L.H. Hu, B. Yang and W. Li, *Hydrothermal synthesis for high-quality CdTe nanocrystals.* Advanced Materials, 2003. **15**(20): p. 1712-+.

124. Yang, W.H., W.W. Li, H.J. Dou and K. Sun, *Hydrothermal synthesis for high-quality CdTe quantum dots capped by cysteamine.* Materials Letters, 2008. **62**(17-18): p. 2564-2566.

125. Bavykin, D.V., V.N. Parmon, A.A. Lapkin and F.C. Walsh, *The effect of hydrothermal conditions on the mesoporous structure of TiO2 nanotubes.* Journal of Materials Chemistry, 2004. **14**(22): p. 3370-3377.

126. Wang, C.C. and J.Y. Ying, *Sol-gel synthesis and hydrothermal processing of anatase and rutile titania nanocrystals.* Chemistry of Materials, 1999. **11**(11): p. 3113-3120.

127. Li, M., H. Schnablegger and S. Mann, *Coupled synthesis and self-assembly of nanoparticles to give structures with controlled organization.* Nature, 1999. **402**(6760): p. 393-395.

128. Kwan, S., F. Kim, J. Akana and P.D. Yang, *Synthesis and assembly of BaWO4 nanorods.* Chemical Communications, 2001(5): p. 447-448.

129. Obare, S.O., N.R. Jana and C.J. Murphy, *Preparation of polystyrene and silica coated gold nanorods and their use as templates for the synthesis of hollow nanotubes.* Nano Letters, 2001. **1**(11): p. 601-603.

130. Mirkin, C.A., R.L. Letsinger, R.C. Mucic and J.J. Storhoff, *A DNA-based method for rationally assembling nanoparticles into macroscopic materials.* NATURE, 1996. **382**(6592): p. 607-609.

131. Mucic, R.C., J.J. Storhoff, C.A. Mirkin and R.L. Letsinger, *DNA-directed synthesis of binary nanoparticle network materials.* Journal of the American Chemical Society, 1998. **120**(48): p. 12674-12675.

132. Yan, H., S.H. Park, G. Finkelstein, J.H. Reif and T.H. LaBean, *DNA-templated self-assembly of protein arrays and highly conductive nanowires.* Science, 2003. **301**(5641): p. 1882-1884.

133. Routkevitch, D., T. Bigioni, M. Moskovits and J.M. Xu, *Electrochemical fabrication of CdS nanowire arrays in porous anodic aluminum oxide templates.* Journal of Physical Chemistry, 1996. **100**(33): p. 14037-14047.

134. Zheng Miao, D.X., Jianhua Ouyang, Guolin Guo, Xinsheng Zhao, and Youqi Tang, *Electrochemically Induced Sol-Gel Preparation of Single-Crystalline TiO2 Nanowires.* Nano Letters, 2002. **2**(7): p. 717.

135. Liang, Z.J., A. Susha and F. Caruso, *Gold nanoparticle-based core-shell and hollow spheres and ordered assemblies thereof.* Chemistry of Materials, 2003. **15**(16): p. 3176-3183.

136. Nielsen, A.E., *Kinetics of precipitation*. 1964: The Macmillan company.

137. Mullin, J.W., *Crystallization*. 2001, Butterworth-Heinemann.

138. Hartman, P. and W.G. Perdok, *On the relations between structure and morphology of crystals 1* Acta Crystallographica, 1955. **8**(1): p. 49-52.

139. Hartman, P. and W.G. Perdok, *On the relations between structure and morphology of crystals 2.* Acta Crystallographica, 1955. **8**(9): p. 521-524.

140. Hartman, P. and W.G. Perdok, *On the relations between structure and morphology of crystals 3.* Acta Crystallographica, 1955. **8**(9): p. 525-529.

141. Burton, W.K., N. Cabrera and F.C. Frank, *The growth of crystals and the equilibrium structure of their surfaces* Philosophical Transactions of the Royal Society of London Series a-Mathematical and Physical Sciences, 1951. **243**(866): p. 299-358.

142. Chernov, A.A., *Formation of crystals in solutions* Contemporary Physics, 1989. **30**(4): p. 251-276.

143. Prywer, J., *Effect of supersaturation on evolution of crystal faces - theoretical analysis.* Journal of Crystal Growth, 2006. **289**(2): p. 630-638.

144. Nanev, C.N., *Polyhedral instability - Skeletal and dendritic growth.* Progress in Crystal Growth and Characterization of Materials, 1997. **35**(1): p. 1-26.

145. Parsiegla, K.I. and J.L. Katz, *Calcite growth inhibition by copper(II) I. Effect of supersaturation.* Journal of Crystal Growth, 1999. **200**(1-2): p. 213-226.

146. Li, S.W., J.H. Xu and G.S. Luo, *Control of crystal morphology through supersaturation ratio and mixing conditions.* Journal of Crystal Growth, 2007. **304**(1): p. 219-224.

147. Chen, L.F. and C. Leonelli, *Alignment of silicon carbide whiskers in polymer matrix.* JOURNAL OF MATERIALS SCIENCE, 1997. **32**(3): p. 627-631.

148. Avella, M., E. Martuscelli, M. Raimo, R. Partch, S.G. Gangolli and B. Pascucci, *Polypropylene reinforced with silicon carbide whiskers.* JOURNAL OF MATERIALS SCIENCE, 1997. **32**(9): p. 2411-2416.

149. Tjong, S.C., R.K.Y. Li and T. Cheung, *Mechanical behavior of CaCO3 particulate-filled beta-crystalline phase polypropylene composites.* Polymer Engineering and Science, 1997. **37**(1): p. 166-172.

150. Tjong, S.C. and Y.Z. Meng, *Performance of potassium titanate whisker reinforced polyamide-6 composites.* Polymer, 1998. **39**(22): p. 5461-5466.

151. Yu, D.M., J.S. Wu, L.M. Zhou, D.R. Xie and S.Z. Wu, *The dielectric and mechanical properties of a potassium-titanate-whisker-reinforced PP/PA blend.* Composites Science and Technology, 2000. **60**(4): p. 499-508.

152. Hu, Z.S. and Y.L. Deng, *Supersaturation control in aragonite synthesis using sparingly soluble calcium sulfate as reactants.* Journal of Colloid and Interface Science, 2003. **266**(2): p. 359-365.

153. Lu, H.D., Y. Hu, J.F. Xiao, Z.Z. Wang, Z.Y. Chen and W.C. Fan, *Magnesium hydroxide sulfate hydrate whisker flame retardant polyethylene/montmorillonite nanocomposites.* JOURNAL OF MATERIALS SCIENCE, 2006. **41**(2): p. 363-367.

154. L. Xiang, F.L., J. Li, Y. Jin, *Hydrothermal formation and characterization of magnesium oxysulfate whiskers.* Materials Chemistry and Physics, 2004. **87**: p. 424–429.

155. Ding, Y., G.T. Zhang, S.Y. Zhang, X.M. Huang, W.C. Yu and Y.T. Qian, *Preparation and characterization of magnesium hydroxide sulfate hydrate whiskers.* Chemistry of Materials, 2000. **12**(10): p. 2845-2852.

156. Lu, H.D., Y.A. Hu, L. Yang, Z.Z. Wang, Z.Y. Chen and W.C. Fan, *Study of the fire performance of magnesium hydroxide sulfate hydrate whisker flame retardant polyethylene.* Macromolecular Materials and Engineering, 2004. **289**(11): p. 984-989.

157. Ding, Y., H.Z. Zhao, Y.G. Sun, G.T. Zhang, H. Wu and Y.T. Qian, *Superstructured magnesium hydroxide sulfate hydrate fibres - Photoluminescence study.* International Journal of Inorganic Materials, 2001. **3**(2): p. 151-156.

158. Yang, D.N., J. Zhang, R.M. Wang and Z.F. Liu, *Solution phase synthesis of magnesium hydroxide sulfate hydrate nanoribbons.* Nanotechnology, 2004. **15**: p. 1625-1627.

159. Linke, W.F., *Solubilities, inorganic and metal-orgainc compounds; a compilation of solubility data from the periodical literature*. 1958-65, Van Nostrand: Princeton, NJ.

160. Dalas, E., P. Klepetsanis and P.G. Koutsoukos, *The overgrowth of calcium carbonate on poly(vinyl chloride-co-vinyl acetate-co-maleic acid).* Langmuir, 1999. **15**: p. 8322.

161. Yang, P. and C.M. Lieber, *Nanostructured high-temperature superconductors: Creation of strong-pinning columnar defects in nanorod/superconductor composites.* Journal of Materials Research, 1997. **12**(11): p. 2981.

162. Ozgur, U., Y.I. Alivov, C. Liu, A. Teke, M.A. Reshchikov, S. Dogan, V. Avrutin, S.J. Cho and H. Morkoc, *A comprehensive review of ZnO materials and devices.* Journal of Applied Physics, 2005. **98**(4).

163. Wang, Z.L., *Zinc oxide nanostructures: growth, properties and applications.* Journal of Physics-Condensed Matter, 2004. **16**(25): p. R829-R858.

164. Navale, S.C., S.W. Gosavi and I.S. Mulla, *Controlled synthesis of ZnO from nanospheres to micro-rods and its gas sensing studies.* Talanta, 2008. **75**(5): p. 1315-1319.

165. Wang, W., B. Zeng, J. Yang, B. Poudel, J. Huang, M.J. Naughton and Z. Ren, *Aligned ultralong ZnO nanobelts and their enhanced field emission.* Advanced Materials, 2006. **18**(24): p. 3275-3278.

166. Beek, W.J.E., M.M. Wienk and R.A.J. Janssen, *Efficient hybrid solar cells from zinc oxide nanoparticles and a conjugated polymer.* Advanced Materials, 2004. **16**(12): p. 1009-+.

167. Wang, Z.L. and J. Song, *Piezoelectric nanogenerators based on zinc oxide nanowire arrays.* Science, 2006. **312**(5771): p. 243-246.

168. Djurisic, A.B. and Y.H. Leung, *Optical properties of ZnO nanostructures.* Small, 2006. **2**(8-9): p. 944-961.

169. Wan, Q., Q.H. Li, Y.J. Chen, T.H. Wang, X.L. He, J.P. Li and C.L. Lin, *Fabrication and ethanol sensing characteristics of ZnO nanowire gas sensors.* Applied Physics Letters, 2004. **84**(18): p. 3654-3656.

170. Fan, Z.Y., D.W. Wang, P.C. Chang, W.Y. Tseng and J.G. Lu, *ZnO nanowire field-effect transistor and oxygen sensing property.* Applied Physics Letters, 2004. **85**(24): p. 5923-5925.

171. Wang, Z.L. and J.H. Song, *Piezoelectric nanogenerators based on zinc oxide nanowire arrays.* Science, 2006. **312**(5771): p. 242-246.

172. Greyson, E.C., Y. Babayan and T.W. Odom, *Directed growth of ordered arrays of small-diameter ZnO nanowires.* Advanced Materials, 2004. **16**(15 SPEC ISS): p. 1348-1352.

173. Pan, Z.W., Z.R. Dai and Z.L. Wang, *Nanobelts of semiconducting oxides.* Science, 2001. **291**(5510): p. 1947-9.

174. Meng, X., B. Lin, B. Gu, J. Zhu and Z. Fu, *A simple growth route towards ZnO thin films and nanorods.* Solid State Communications, 2005. **135**(7): p. 411-415.

175. Kong, X.Y., Y. Ding, R. Yang and Z.L. Wang, *Single-Crystal Nanorings Formed by Epitaxial Self-Coiling of Polar Nanobelts.* Science, 2004. **303**(5662): p. 1348-1351.

176. Herring, C., *Some Theorems on the Free Engergies of Crystal Surface.* Physical Review, 1951. **82**(1): p. 87.

177. Park, J.H., H.J. Choi and J.G. Park, *Scaffolding and filling process: a new type of 2D crystal growth.* Journal of Crystal Growth, 2004. **263**(1-4): p. 237-242.

178. Vayssieres, L., *Growth of arrayed nanorods and nanowires of ZnO from aquesous solutions.* Advanced Materials, 2003. **15**(5): p. 464-466.

179. Vayssieres, L., K. Keis, S.E. Lindquist and A. Hagfeldt, *Purpose-built anisotropic metal oxide material: 3D highly oriented microrod array of ZnO.* Journal of Physical Chemistry B, 2001. **105**(17): p. 3350-3352.

180. Qin, Y., R.S. Yang and Z.L. Wang, *Growth of Horizonatal ZnO Nanowire Arrays on Any Substrate.* Journal of Physical Chemistry C, 2008. **112**(48): p. 18734-18736.

181. Yoshino, Y., K. Inoue, M. Takeuchi, T. Makino, Y. Katayama and T. Hata. *Effect of substrate surface morphology and interface microstructure in ZnO thin films formed on various substrates*. 2000.

182. Van Werde, K., D. Mondelaers, G. Vanhoyland, D. Nelis, M.K. Van Bael, J. Mullens, L.C. Van Poucke, B. Van der Veken and H.O. Desseyn, *Thermal decomposition of the ammonium zinc acetate citrate precursor for aqueous chemical solution deposition of ZnO.* JOURNAL OF MATERIALS SCIENCE, 2002. **37**(1): p. 81-88.

183. Mitra, P. and J. Khan, *Chemical deposition of ZnO films from ammonium zincate bath.* Materials Chemistry and Physics, 2006. **98**(2-3): p. 279-284.

184. Peterson, R.B., C.L. Fields and B.A. Gregg, *Epitaxial chemical deposition of ZnO nanocolumns from NaOH.* Langmuir, 2004. **20**(12): p. 5114-5118.

185. Zhao, J., Z.G. Jin, X.X. Liu and Z.F. Liu, *Growth and morphology of ZnO nanorods prepared from Zn(NO3)(2)/NaOH solutions.* Journal of the European Ceramic Society, 2006. **26**(16): p. 3745-3752.

186. Inubushi, Y., R. Takami, M. Iwasaki, H. Tada and S. Ito, *Mechanism of formation of nanocrystalline ZnO particles through the reaction of [Zn(acac)(2)] with NaOH in EtOH.* Journal of Colloid and Interface Science, 1998. **200**(2): p. 220-227.

187. Fricke, R. and K. Meyring, *Concerning the thermal capacity of crystalised modifications of zinc hydroxides 14 Announcement concerning the structure, thermal capacity and other characteristics of active substances according to R. Fricke and colleagues.* Zeitschrift Fur Anorganische Und Allgemeine Chemie, 1937. **230**(4): p. 357-365.

188. Uekawa, N., R. Yamashita, Y.J. Wu and K. Kakegawa, *Effect of alkali metal hydroxide on formation processes of zinc oxide crystallites from aqueous solutions containing Zn(OH)(4)(2-) ions.* Physical Chemistry Chemical Physics, 2004. **6**(2): p. 442-446.

189. Meulenkamp, E.A., *Synthesis and growth of ZnO nanoparticles.* Journal of Physical Chemistry B, 1998. **102**(29): p. 5566-5572.

190. Vayssieres, L., *Growth of arrayed nanorods and nanowires of ZnO from aqueous solutions.* Advanced Materials, 2003. **15**(5): p. 464-466.

191. Wang, B.G., E.W. Shi and W.Z. Zhong, *Understanding and controlling the morphology of ZnO crystallites under hydrothermal conditions.* Crystal Research and Technology, 1997. **32**(5): p. 659-667.

192. Govender, K., D.S. Boyle, P.B. Kenway and P. O'Brien, *Understanding the factors that govern the deposition and morphology of thin films of ZnO from aqueous solution?* Journal of Materials Chemistry, 2004. **14**(16): p. 2575-2591.

193. Mukherjee, S., K. Kim and S. Nair, *Short, highly ordered, single-walled mixed-oxide nanotubes assemble from amorphous nanoparticles.* Journal of the American Chemical Society, 2007. **129**(21): p. 6820-6826.

194. Hu, Z.S., D.J.E. Ramirez, B.E.H. Cervera, G. Oskam and P.C. Searson, *Synthesis of ZnO nanoparticles in 2-propanol by reaction with water.* Journal of Physical Chemistry B, 2005. **109**(22): p. 11209-11214.

195. Wong, E.M., J.E. Bonevich and P.C. Searson, *Growth kinetics of nanocrystalline ZnO particles from colloidal suspensions.* Journal of Physical Chemistry B, 1998. **102**(40): p. 7770-7775.

196. Hu, Z.S., G. Oskam and P.C. Searson, *Influence of solvent on the growth of ZnO nanoparticles.* Journal of Colloid and Interface Science, 2003. **263**(2): p. 454-460.

197. Viswanatha, R., H. Amenitsch and D.D. Sarma, *Growth kinetics of ZnO nanocrystals: A few surprises.* Journal of the American Chemical Society, 2007. **129**(14): p. 4470-4475.

198. Ethayaraja, M. and R. Bandyopadhyaya, *Mechanism and modeling of nanorod formation from nanodots.* Langmuir, 2007. **23**(11): p. 6418-6423.

199. Lee Penn, R. and J.F. Banfield, *Imperfect oriented attachment: dislocation generation in defect-free nanocrystals.* Science, 1998. **281**(5379): p. 969-971.

200. Zhang, J., Z. Lin, Y. Lan, G. Ren, D. Chen, F. Huang and M. Hong, *A multistep oriented attachment kinetics: Coarsening of ZnS nanoparticle in concentrated NaOH.* Journal of the American Chemical Society, 2006. **128**(39): p. 12981-12987.

201. Xu, S., Y. Wei, M. Kirkham, J. Liu, W. Mai, D. Davidovic, R.L. Snyder and Z.L. Wang, *Patterned Growth of Vertically Aligned ZnO Nanowire Arrays on Inorganic Substrates at Low Temperature without Catalyst.* Journal of the American Chemical Society, 2008. **130**(45): p. 14958-+.

202. Sugimoto, T., *Preparation of monodispersed colloidal particles* Advances in Colloid and Interface Science, 1987. **28**(1): p. 65-108.

203. Lamer, V.K. and R.H. Dinegar, *Theory,production and mechanism of formation of monodispersed hydrosols* Journal of the American Chemical Society, 1950. **72**(11): p. 4847-4854.

204. Chen, H.M., R.S. Liu, M.Y. Lo, S.C. Chang, L.D. Tsai, Y.M. Peng and J.F. Lee, *Hollow platinum spheres with nano-channels: Synthesis and enhanced catalysis for oxygen reduction.* Journal of Physical Chemistry C, 2008. **112**(20): p. 7522-7526.

205. Kidambi, S., J.H. Dai, J. Li and M.L. Bruening, *Selective hydrogenation by Pd nanoparticles embedded in polyelectrolyte multilayers.* Journal of the American Chemical Society, 2004. **126**(9): p. 2658-2659.

206. Zhu, Y.F., J.L. Shi, W.H. Shen, X.P. Dong, J.W. Feng, M.L. Ruan and Y.S. Li, *Stimuli-responsive controlled drug release from a hollow mesoporous silica sphere/polyelectrolyte multilayer core-shell structure.* Angewandte Chemie-International Edition, 2005. **44**(32): p. 5083-5087.

207. Davis, M.E., *Ordered porous materials for emerging applications.* Nature, 2002. **417**(6891): p. 813-821.

208. Schartl, W., *Crosslinked spherical nanoparticles with core-shell topology.* Advanced Materials, 2000. **12**(24): p. 1899-+.

209. Yang, H.G. and H.C. Zeng, *Preparation of hollow anatase TiO2 nanospheres via Ostwald ripening.* Journal of Physical Chemistry B, 2004. **108**(11): p. 3492-3495.

210. Zhong, Z.Y., Y.D. Yin, B. Gates and Y.N. Xia, *Preparation of mesoscale hollow spheres of TiO2 and SnO2 by templating against crystalline arrays of polystyrene beads.* Advanced Materials, 2000. **12**(3): p. 206-+.

211. Wijnhoven, J. and W.L. Vos, *Preparation of photonic crystals made of air spheres in titania.* Science, 1998. **281**(5378): p. 802-804.

212. Kim, S.W., M. Kim, W.Y. Lee and T. Hyeon, *Fabrication of hollow palladium spheres and their successful application to the recyclable heterogeneous catalyst for Suzuki coupling reactions.* Journal of the American Chemical Society, 2002. **124**(26): p. 7642-7643.

213. Jiang, P., J.F. Bertone and V.L. Colvin, *A lost-wax approach to monodisperse colloids and their crystals.* Science, 2001. **291**(5503): p. 453-457.

214. Nakashima, T. and N. Kimizuka, *Interfacial synthesis of hollow TiO2 microspheres in ionic liquids.* Journal of the American Chemical Society, 2003. **125**(21): p. 6386-6387.

215. Kamata, K., Y. Lu and Y.N. Xia, *Synthesis and characterization of monodispersed core-shell spherical colloids with movable cores.* Journal of the American Chemical Society, 2003. **125**(9): p. 2384-2385.

216. Imhof, A., *Preparation and characterization of titania-coated polystyrene spheres and hollow titania shells.* Langmuir, 2001. **17**(12): p. 3579-3585.

217. Qian, H., G. Lin, Y. Zhang, P. Gunawan and R. Xu, *A new approach to synthesize uniform metal oxide hollow nanospheres via controlled precipitation.* Nanotechnology, 2007. **18**(35): p. 355602.

218. Zhang, Y., E.-W. Shi, Z.-Z. Chen and B. Xiao, *Fabrication of ZnO hollow nanospheres and "jingle bell" shaped nanospheres.* Materials Letters, 2008. **62**(8-9): p. 1435-1437.

219. Jongnam Park, B.K., † Ki Youl Yoon,† Yosun Hwang,‡ Misun Kang,‡ and a.T.H. Je-Geun Park, †, *Generalized Synthesis of Metal Phosphide Nanorods via Thermal Decomposition of Continuously Delivered Metal-Phosphine Complexes Using a Syringe Pump.* JACS, 2005. **127**: p. 8433-8440.

220. Tang, Z.Y., N.A. Kotov and M. Giersig, *Spontaneous organization of single CdTe nanoparticles into luminescent nanowires.* Science, 2002. **297**(5579): p. 237-240.

221. Cho, K.S., D.V. Talapin, W. Gaschler and C.B. Murray, *Designing PbSe nanowires and nanorings through oriented attachment of nanoparticles.* Journal of the American Chemical Society, 2005. **127**(19): p. 7140-7147.